Design and Fabrication of Micro-electro-mechanical Systems Actuators for Application in External Cavity Tunable Lasers

By

T. M. Fahim Amin

A thesis submitted in partial fulfillment of the requirements for the degree of

Doctor of Philosophy

in

Microsystems and Nanodevices

Department of Electrical and Computer Engineering

University of Alberta

Abstract

The limited availability of rugged and economical infra-red laser sources that can be tuned over a certain wavelength range is still a bottleneck for widespread application of spectroscopic methods to environmental, industrial, and medical trace gas monitoring. Conventional semiconductor lasers in distributed feedback (DFB) configuration offer only limited wavelength tuning around the center wavelength. External cavity lasers (ECLs) can provide the large tuning ranges needed for laser spectroscopy. Micro-electro-mechanical systems (MEMS) technology is a viable option for integrating and manipulating optical elements and thus fabricating a hybrid integrated ECL at chip level dimensions. With this thesis, I present a strong foundation for building a widely tunable MEMS based ECL. The major contributions are: 1) design and fabrication of different rotary comb actuators to build micro-opto-electromechanical systems (MOEMS) devices for various applications, including ECLs; 2) development of two silicon sidewall smoothing techniques which can provide optical quality reflecting surfaces; and 3) design of an extremely long arm MEMS actuator with zipped comb fingers and structural re-enforcement, and development of an efficient method of mounting external micro mirrors onto MEMS devices.

The first rotary comb actuator presented in this thesis provides a large deflection angle of 3° at a, for MEMS technology, reasonably low voltage of 100 V. This actuator has a high resonance frequency (>1 kHz) and can be used for optical applications where kHz level

frequency operation is required. The virtual pivot point actuator has a pivot point located distant from the physical actuator and offers more options for in-plane optical path alignment. The detailed design and the implementation of the virtual pivot point actuator are presented. The full rotation angle for this actuator is 3° (± 1.5°) for an applied voltage of 190 V. Both of these designs provide an accessible sidewall which can be used as a reflecting surface for on-chip integration. The sidewalls of the actuators were smoothed using either an over-passivated or a two-step oxidation + BOE (buffered oxide etch) technique. The over-passivated recipe uses controlled over-passivation during reactive ion etching with the Bosch process to obtain a smooth sidewall. An rms roughess of as low as 3.93 nm was achieved for the etched sidewall of the rotary comb actuator using this process. The second process uses a thermal oxidation step followed by buffered oxide etching. Repeating this process and using a carefully chosen temperature and oxidation time resulted in the desired optical quality sidewall. This method has no theoretical limitations in terms of smoothing thick structures and the rms roughness achieved for a 100 μm thick silicon sidewall was 2.56 nm. A third actuator was designed with a long movable arm that can support relatively large externally mounted optical components. This actuator will be especially useful for optical applications that require larger optical beams and therefore also large reflectors. For an ECL, a large, high quality external mirror can maximize the reflected light fed back into the gain medium and increase the wavelength tuning range.

Preface

This PhD thesis is based on the research I have done at the University of Alberta as part of a broad collaborative project “development of a MEMS external cavity diode laser in the mid-infrared region for spectroscopic applications”. This collaborative research project was a collaborative effort by Professor Dr. Wolfgang Jäger at the Department of Chemistry, University of Alberta, Professor Dr. John Tulip at the Department of Electrical and Computer Engineering, University of Alberta and two industrial partners, Norcada Inc. and Boreal Laser Inc.

The research results presented in chapter 3 to chapter 5 of this thesis are based on my original work. Figures 6.1 and 6.2 of chapter 6 are a result of my collaborative work with co-researcher Dr. Quamrul Huda; I was responsible for the design of the rotary comb actuator and developing part of the fabrication process. Dr. Huda fabricated the final actuator and smoothed the extruded mirror on the backside. The rest of chapter 6 is based on research done by me.

Parts of chapter 3 (design and simulation) and chapter 5 (over-passivated smoothing technique) have been published (M. Q. Huda, T. M. F. Amin, Y. Ning, G. McKinnon, J. Tulip, and W. Jäger, “Rotary MEMS comb-drive actuator with smooth sidewall for photonic applications,” Journal of Micro/Nanolithography, MEMS, and MOEMS, 11, 023012, 2012). I

was responsible for the rotary actuator design and all the necessary simulations for this paper. I also developed the recipe for smoothing the silicon sidewall that was presented in the paper. Dr. M. Q. Huda performed the final fabrication of the actuator and prepared the first draft of the manuscript. Dr. Y. Ning and Dr. G. Mckinnon of Norcada Inc. provided assistance in fabrication of the actuator. Professor W. Jäger and Professor J. Tulip are the supervisory authors. Professor Jäger was involved in the concept formation and manuscript composition.

A manuscript based on chapter 4 and the second smoothing technique (2-step oxidation + BOE) described in chapter 5 has been submitted submitted to the Journal of Micromechanics and Micro-engineering (T. M. F. Amin, M. Q. Huda, J. Tulip, and W. Jäger, "A virtual pivot point MEMS actuator with optical quality sidewall") soon. I was responsible for design, analysis and fabrication of the actuator described in this journal. I also developed the technique for smoothing the Si sidewall and prepared the first draft of the manuscript. Dr. M. Q. Huda prepared the mask for fabrication of the actuator and is also involved in the manuscript composition. Professor J. Tulip and Professor W. Jäger are the supervisory authors. Professor Jäger is also involved in the concept formation, and manuscript composition.

A modified version of chapter 6 of this thesis is to be submitted to the Journal of Microelectromechanical Systems (T. M. F. Amin, M. Q. Huda, J. Tulip, and W. Jäger, "Design and Fabrication of a Long Arm Comb Drive Actuator with Externally Mounted Mirror for Optical Applications"). I was responsible for design, analysis and fabrication of the long arm actuator. I also developed the technique for mounting external mirror onto the actuator and

prepared the first draft of the manuscript. Dr. M. Q. Huda prepared the mask for fabrication of the actuator and is also involved in the manuscript composition. Professor J. Tulip and Professor W. Jäger are the supervisory authors. Professor Jäger is also involved in the concept formation, and manuscript composition.

This thesis is dedicated to

My loving parents

Acknowledgements

The long voyage of completion of this thesis is possible through lots of unmeasurable contributions from people involved with personal and academic life. Above everything, at first I want to show my gratitude to the Almighty Allah for His unbounding blessings in my life.

I would like to thank my supervisor Professor Dr. Wolfgang Jäger for his countless help, support, and encouragement during the course of the research. I appreciate his insightful suggestions and advices, and above all, the confidence that he had in me. I am also indebted to Professor Emeritus Dr. John Tulip, my departmental supervisor, who had given me the opportunity to work in this project technically and provided me financial support and guidance for the first few years of this project. To John and Wolfgang, I cannot thank you enough.

I am also grateful to Dr. Quamrul Huda, a research associate who worked in this project for his help, contribution and cooperation in my work. I really appreciate his time to discuss solving different critical problems. I also gratefully mention Dr. Kevin Kornelson for his help with the COMSOL simulations.

I would like to thank the industrial partner of this project, Norcada Inc. for their collaboration in this project. I would specially acknowledge Dr. Graham Mckinnon, Dr. Yuebin Ning and Dr.

Nakeeran Ponnampalam for their help in fabrication related issues and developing the mirror mounting setup.

A few people deserve further mention. To Scott Munro, I appreciate the processing skills he taught me and the discussion regarding impact of processing parameters in reactive ion etching. I also thank other nanofab staffs including Jolene Jalota, Les Schowalter and Stephanie Bozic for their help in teaching fabrication techniques and valuable suggestions.

I would like to thank Suraiya Farzana for inspiring me continuing my PhD when I became frustrated and supporting me many ways. I really appreciate her help in teaching me drawing schematic diagram for technical paper. I am also grateful to Linh Nguyen, the guy just sit beside me, for creating an enjoyable and cooperative environment in the office that helped me to concentrate on the research at some very difficult moment of my life. I am very fortunate to make a great friend like you during my stay at University of Alberta.

Finally and most importantly, I need to thank my parents, from whom everything of my life starts and reaches to its destination. They have always supported me in the choices I have made and provided me the support when I needed most.

Funding for this work was provided by Alberta Innovates and Technology Future through its Nanoworks program and by Natural Science and Engineering Research Council of Canada. The devices were fabricated in the nanoFab, University of Alberta.

Table of Contents

List of Tables

List of Figures

List of Symbols

Symbol	Meaning (Unit)
C	Capacitance (F)
V	Voltage (V)
F	Force (N)
E	Young's Modulus (Pa)
ε	Permittivity (F/m)
z	Gap between electrode in z-direction (m)
g	Lateral gap between electrode (m)
r_2	Reflectance of the laser facet
r_3	Coupling efficiency of the external cavity
d_0	Length of the internal laser cavity(m)
λ	Wavelength (m)
v	Frequency (Hz)
Γ_0	Optical confinement factor
μ_0	Refractive index of gain medium
α_0	Linewidth enhancement factor
l	Overlap between comb finger (m)
M	Effective mass (g)
f	Resonance Frequency (Hz)

w	Beam width (m)
L	Beam length (m)
h	Thickness (m)
N	Number of comb fingers
R	Radius of comb fingers (m)
w_f	Comb finger width (m)
θ_i	Angular overlap between fingers (deg.)
α	Adjustable parameter to account fringing field between electrodes
β	Adjustable parameter to account fringing field between electrodes
K	Spring constant (N/m)
I	Second moment of inertia (m^4)
Y	Ratio of second moment of Inertia
L_C / L_F	Distance between beam tip and middle position of all the engaged comb fingers
L_m	Mirror holder length (m)
L_S	Comb finger span length (m)
L_T	Truss length
R	Reaction force at the anchor point (N)
y	Gap mismatch (m), displacement of moving comb fingers from its nominal middle position between fixed comb fingers

Glossary of Terms

Abbreviation	Meaning
MEMS	Micro-electro-mechanical systems
MOEMS	Micro-opto-electro-mechanical systems
EC	External cavity
ECL	External cavity laser
ECSDL	External cavity semiconductor diode laser
VPP	Virtual pivot point
RIE	Reactive ion etching
DRIE	Deep reactive ion etching
ICP	Inductively coupled plasma
BOE	Buffered oxide etch
CRD	Critical Point Drying
SEM	Scanning electron microscope
AFM	Atomic Force Microscope
BOX	Buried Oxide
STS	Surface Technology Systems
AR	Anti-reflection
FSR	Free spectral range

MIR	Mid-infrared
VCSEL	Vertical cavity surface emitting laser
DFB	Distributed feedback
BTEX	Benzene, toluene, ethyl-benzene, and xylene

1 Introduction

1.1 Research Introduction and Background

The detection, quantification and characterization of trace-gas species have many important industrial, urban, medical, and environmental applications. In industry, gas sensing technology is widely used for, for example, reaction kinetics monitoring, pipeline leak detection, industrial emissions and process monitoring, and agricultural monitoring [1, 2]. For example, detection of nitric oxide (NO) is used in many industrial plants for combustion diagnostics. Recent advances in epidemiological research reveal that many diseases can be linked to exposure to environmental trace gas pollutants. For example, continuous exposure to atmospheric pollutants, such as carbon monoxide, ozone, nitrogen dioxide and other toxic gases may cause serious cardiovascular and respiratory disease and increased mortality [3, 4]. Because of these short term and long term effects on human health, detection and monitoring of those trace gases is very important. From an environmental perspective, the ability to continuously monitor the concentrations of toxic pollutants and greenhouse gases is very important to maintain air quality and predict long term environmental issues. Atmospheric, photo-induced oxidation processes of some trace gases can lead to the formation of fine particulate matter, called aerosol. Such atmospheric aerosols (diameter ~ 1 nm to 10 μm) have the ability to penetrate deep into the lung, as opposed to large sized dust

particles, and can cause asthma and other pulmonary and respiratory diseases [5]. In addition, aerosol particles have direct and indirect effects on the radiative forcing of Earth's climate system [5]. They can scatter, reflect or absorb solar radiation and affect the global radiative energy balance and Earth's temperature. Their influence on the cloud condensation and ice nucleation process can affect cloud lifetime and the global hydrological cycle. Despite the ubiquitous threat on health and environment from these gases and particles, our understanding of the underlying physicochemical and biological processes is limited in many cases. Sensitive, reliable, and easy-to-use trace gas sensors can help to establish or improve regulatory frameworks regarding release of trace gases and acceptable atmospheric concentrations and make it possible to enforce regulations. Laser spectroscopic detection techniques have significant advantages over traditional wet chemical processes, which require sampling and laboratory analysis. Laser based detectors can be used in situ, are sensitive and selective, provide data in real time, allow long open path measurements, and can be operated remotely and intervention free.

Laser spectroscopic detectors can also be used in other applications such as medical diagnostics, atmospheric physics and chemistry research, and monitoring tasks on space missions. Laser based breath analysis promises to become an efficient, non-invasive diagnostic tool in the near future. For example, nitric oxide in exhaled breath is an indicator of an inflamed airway and may have potential application for diagnosis of asthma and other respiratory inflammatory diseases [6]. Similarly, exhaled NH_3 is a potential non-invasive bio-marker of liver and kidney function as well as peptic ulcer disease [7]. Detailed discussions about diseases that may potentially be diagnosed using breath analysis can be found in [2, 8]. Laser based trace gas sensing is also an important tool in manned or unmanned space

missions. A very recent example, the Mars laser hygrometer, was built to measure the water vapor mixing ratio in the Martian atmosphere and in gas that has thermally evolved from Martian soil or ice samples in situ [9].

In spectroscopic studies, an optical signal is broken up into its wavelength components and the light intensity is measured as a function of wavelength. The resulting spectrum contains detailed information about the light source or about the path through which the light is transmitted. Spectroscopy has become a very important tool in many areas of science and engineering to identify and quantify substances by analyzing the emitted or absorbed spectral profile. The simplest absorption based methods usually involve probing at a wavelength where absorption occurs, and also at a nearby wavelength chosen to be essentially free of any absorption of the target gas and possible contaminants. The target gas concentration can be deduced by comparing the measured spectra. Absorption spectroscopy requires quantitative knowledge of the gas absorption characteristics which is the realm of molecular spectroscopy, a proven and highly developed subject. Each molecule has a unique set of rotational, vibrational, and electronic energy levels. The energies of these levels depend on the molecular structure, the bond strengths, and the electron distribution within the molecule. Transitions between these energy levels are governed by selection rules, and can be caused by absorption or emission of electromagnetic radiation. Absorption or emission of radiation may thus change the electronic or vibrational or rotational state of the molecule. In general, pure rotational transitions occur in the microwave and millimeter wave ranges, vibrational transitions in the infrared range, and electronic transitions in the visible and ultraviolet ranges. Each molecule is characterized by unique spectral signatures in these ranges and has specific values of absorption parameters. Its spectrum can thus be

used to identify and quantify trace amounts of a molecule in, for example, the atmosphere or other gaseous samples. Wavelength tunable laser light is the most preferred light source for spectroscopic applications because of its high intensity and narrow spectral line width.

Among the many laser technologies, laser diodes stand out as they are very similar to electronic components - small, efficient and rugged. Other laser technologies have some limitations in spectroscopy because of high cost, low power conversion efficiency, large size and mass. All field useable laser-based sensing spectrometers can use the laser diode as a light source for spectroscopic gas detection. Commercial, environmental, and present industrial diode-laser spectrometers use the readily available near infrared lasers developed for telecommunication applications. Unfortunately, molecular absorption in the near-infrared region is weak and commercial devices are currently limited to the detection of a few small gaseous compounds such as CO_2 and CH_4. On the other hand, the vast majority of gaseous chemical substances exhibit fundamental vibrational absorption bands in the mid-infrared spectral region (≈ 2.5 – 25 μm) and the absorption of light by these fundamental bands provides a nearly universal means for their detection [2]. Mid-infrared absorption spectroscopy can be used to detect environmentally important toxic gases (NO, CO_2, etc.), hydrocarbon molecule like methane, ethylene and gaseous precursors of aerosol particles such as benzene and the associated aromatics toluene, ethyl-benzene, and xylene (together referred to as BTEX) which are by-products of the petrochemical industry and automobile vehicles. Another major advantage of mid-infrared laser spectroscopy is its suitability for open path sensing in so-called atmospheric windows that is in wavelength regions with minimal atmospheric absorption. The development of new and better techniques for laser-

based mid-infrared spectroscopic trace gas sensing with broadly tunable diode lasers promises to revolutionize trace gas monitoring and its applications.

1.2 The Tunable Diode Laser

The semiconductor diode laser started its journey with the invention of coherent light emitting GaAs junctions in 1962 [10, 11]. The laser diode gradually became the most commercially important and probably the most socially important invention of laser technologies. Today, the laser diode can be found in a wide range of applications including barcode readers, laser pointers, CD/DVD/Blu-ray players, laser printers, scanners and fiber-optic communications. Most of these applications use fixed wavelength lasers. However there are many other important applications that require the laser wavelength to be tunable. The design and development of wavelength tunable diode lasers has become a major area of interest. The use of tunable diode lasers has been reported to improve the functionality of optical networks by enabling wavelength conversion, wavelength-based switching, routing and virtual networking in large scale all optical networks [12, 13]. Tunable diode lasers can also play a key role in applications like dense wavelength division multiplexing (DWDM), spectroscopy, medical diagnostics and space technology. In principle, laser-based spectroscopic trace gas sensing allows one to selectively detect several different molecular gas species simultaneously by means of a single, tunable and portable sensing device that is capable of high sensitivity and rapid response time. Unfortunately most of the present gas sensors cannot meet these demanding requirements. Current field useable diode laser spectrometers are limited to using the distributed feedback (DFB) laser as light source. This type of laser is

spectrally pure but its tuning range is very limited and the spectrometer is useful only for detection of few species such as CO_2 and CH_4. In order to be generally useful for spectroscopy, the diode laser should not only emit in the mid infrared but it should also be broadly tunable.

Conventional mechanisms for wavelength tuning of diode lasers are variation of the laser injection current or changing the temperature of the chip. Although wavelength tuning using current or temperature variation is simple, it only allows for a limited range of tuning. Another disadvantage of thermal tuning is that it affects the effective laser gain, which causes a decrease of the laser output power with increasing temperature of the laser chip. In an external cavity laser (ECL), wavelength tuning is achieved by varying the length of an external cavity. This approach has attracted significant interest as it can provide a large tuning range while maintaining a single longitudinal mode. The presence of an external cavity yields a number of performance enhancements such as narrow linewidth (~1 kHz) and a high side mode suppression ratio (>30 dB) [12].

1.3 The External Cavity Tunable Diode Laser

A typical external cavity semiconductor diode laser (ECSDL) has a semiconductor gain medium with its front facet normally anti-reflection (AR) coated. The output from the AR coated facet is reflected back into the waveguide by an external reflector. Most of the ECLs have been designed either using a mirror or a grating as the external reflector. The tunability of an ECL depends on the gain medium and the properties of the external cavity, such as the

type of the external reflector, cavity length, and feedback strength (i.e., coupling efficiency of the external cavity). The type of the reflector determines the general characteristics of the laser. The gain chip is normally used to provide broad optical gain to enable continuous tuning over a large range. Once the reflector type is chosen, the cavity length and feedback strength are the main contributors in determining the characteristics of the ECL, such as tuning range, resolution and tuning behavior (discretely, quasi-continuously, or continuously etc.).

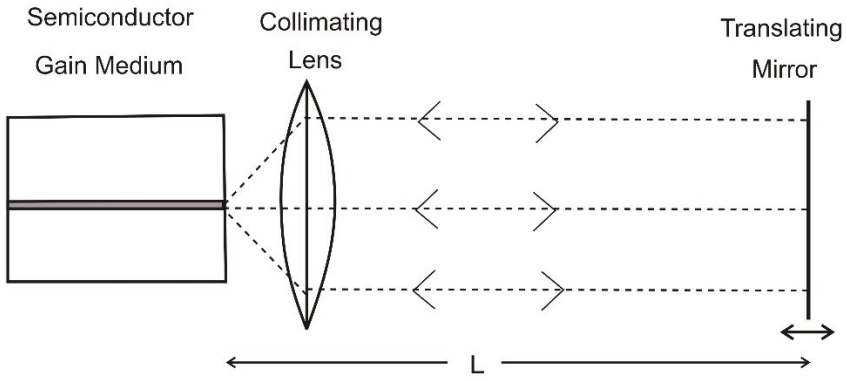

Figure 1.1 Schematic of an External Cavity Laser

The mirror configuration shown in Figure 1.1 is the simplest structure for an ECL and is often used for research and development. However, this mirror configuration does not provide single mode operation, which is required for many applications such as spectroscopy and telecommunications. The performance can be improved by the use of wavelength selective components, such as a grating, as external reflector. Two types of standard grating configurations have been developed, namely the Littrow scheme (Figure 1.2a) and the Littman scheme [14] (Figure 1.2b). In the Littrow scheme, the laser beam is collimated onto a

movable grating and the diffracted light from the blazed grating is reflected back into the gain medium. In the Littman configuration, the light incident on the grating is diffracted onto a movable mirror that reflects the light back, via the grating, into the gain medium. An advantage of the Littman configuration is that the light is diffracted twice by the grating per round trip through the cavity, leading to better out-of-band suppression in the grating filter. The laser in grating configuration operates based on the simultaneous action of two filters: 1) the cavity itself with a free spectral range (FSR) that is determined by the cavity length and 2) the grating that only reflects only a narrow band of wavelengths back into the gain medium [15]. The wavelength selection of these two filters must be aligned with each other to achieve lasing of the gain medium, which means that the cavity length must be accurately controlled at sub-wavelength level.

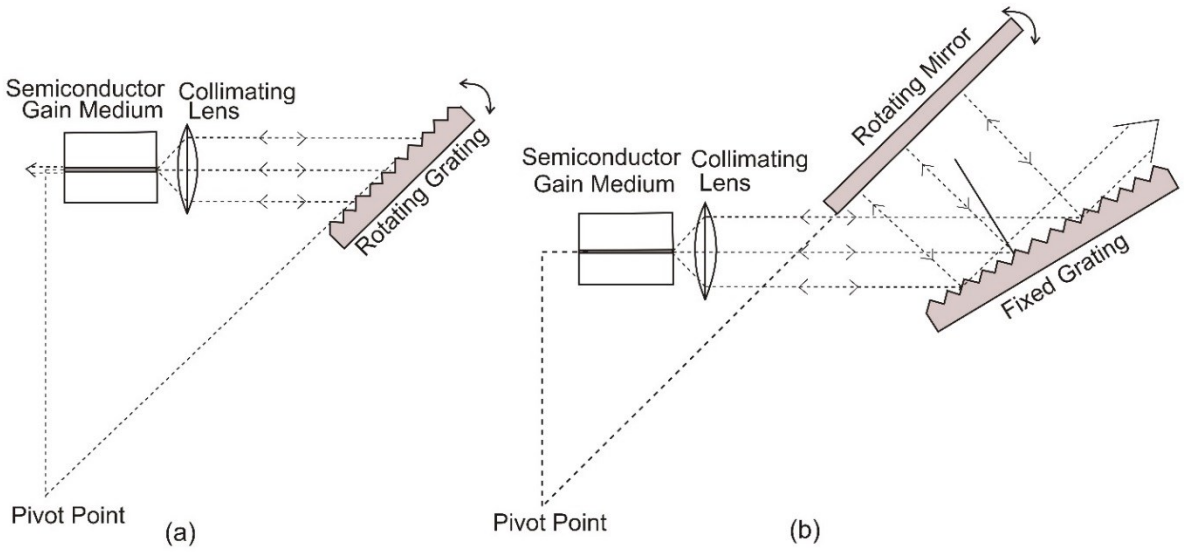

Figure 1.2 Grating based ECL configurations; (a) Littrow; (b) Littman

Efforts to use diode lasers in external cavity (EC) configuration have so far been concentrated on telecommunication lasers and have only been moderately successful. Most of the current ECLs for spectroscopic applications suffer a number of disadvantages like bulkiness, poor sensitivity, and cost. The conventional ECL usually uses a stepper motor or a piezoelectric actuator to change the cavity length. The problem of a piezoelectric actuator is that it suffers hysteresis and needs precise temperature control. Motorized tuning control has the problem that it is not robust and can create shock and vibration. On the other hand, micro electromechanical systems (MEMS) based actuators have a natural synergism with external cavity tunable diode lasers in a number of ways. The sizes of a semiconductor diode laser chips and MEMS devices are on the same scale, typically several hundred micrometer long. MEMS based actuators enable fine tuning of mirror or grating position with high repeatability. Also, very short external cavities (<100 μm) can be formed which cannot be realized using discrete optical components [2]. The small size of MEMS devices can make the laser lightweight, portable, and can bring a large array of enhanced mechanical-related properties (e.g., tuning speed, tuning resolution/accuracy, and mechanical reliability/stability). ECLs with MEMS integration have the potential to provide spectroscopic system of small size and with high sensitivity and multiple gas detection capability at reasonable cost.

1.4 MEMS

Research and development of MEMS devices have made significant progress since the earliest MEMS device was fabricated in 1965 [16]. Micro-fabrication technologies, which are used to produce the vast majority of MEMS devices, make it now possible to build

mechanical component with sub-micrometer precision. Moreover, the technology enables batch fabrication of MEMS devices with significant cost reduction and there is always the possibility to integrate micro mechanical elements with electronic circuits and thus enable fully integrated micro-scale systems. With the emergence of wafer bonding, thin film technology, and deep reactive ion etching, the fabrication of 3-dimensional MEMS structures is now quite common. Materials, such as SU-8, a polymer to form microfluidic devices, and pyrex which can be anodically bonded to Si, are being used in MEMS fabrication processes, and enable the design and construction of more complex structures. Metals, like gold, are also being utilized to provide better optical or electrical properties of the MEMS devices. MEMS systems can be integrated with electronics, mechanics, light, or fluids. Modern MEMS devices can fulfill many functions, for example, sense, actuate, or communicate. They can redirect light, control flow of fluids, and detect molecules, heat, pressure, or motion. MEMS devices are being used widely in many applications such as in automobiles to measure tire or fuel pressure or trigger the deployment of airbags [17], in biomedicine [18], telecommunications [19], microfluidics and optics [15].

Optical applications, in particular, make up a large portion of today's MEMS industrial products. It all started with two papers published by Petersen [20, 21] which eventually led to a new thriving field of MEMs known as micro-opto-electromechanical systems (MOEMS). The concept of MEMS is very compatible with micro optics in the sense that even a small motion of a component can deliver a significant optical effect. For instance, a small tilt angle of a micro mirror translates into a large displacement of the reflected light beam seen at a distance. For some laser applications, only a displacement of about half a wavelength is needed to tune over the desired range. This can be easily achieved using micro actuators.

One of the most successful optical MEMS devices is the digital micro mirror developed by Texas Instruments [22]. Hundreds of thousands of micro mirrors are now widely used in portable projectors, large-screen TVs, and digital cinemas. Many optical MEMS devices such as optical switches, attenuators, add/drop multiplexers and wavelength selective switches have been developed for application in telecommunication [15, 23]. Tunable laser technology is another area which can be revolutionized by MEMS integration.

1.5 The Broad Research Project

In 2009, researchers at the University of Alberta, Norcada Inc., an Edmonton based MEMS production company, and Boreal Laser Inc., a company that develops laser based gas analyzers**,** started a collaborative research effort to develop new MOEMS integrated tunable laser technology. The main objective of that research project was to build an EC tunable diode laser in the mid-infrared (MIR) region for spectroscopic applications. As a MEMS company, Norcada was interested to expand its product line by developing MOEMS based tunable lasers. Boreal Laser was keen to combine this new technology with its core gas sensing technology to build a new class of laser based gas sensors that will detect environmentally and industrially important trace gases. Both companies partnered with researchers at the University of Alberta for much needed research support. Central aspects of this research program included characterization of gain media obtained from the Canadian Photonics Fabrication Centre of the National Research Council of Canada, development of a bench-top tunable MIR ECL using discrete components, characterization of the bench-top ECL, production of control hardware and software, development of MEMS actuators, fabrication of optical quality silicon components, on-chip integration of MEMS actuators and

optical components, and characterization of the MEMS-based ECL. Each collaboration partner was responsible for specific aspects of this research program.

1.6 Objective of my PhD Research

The main objective of my PhD research was to explore MEMS designs that will serve best in building the EC tunable diode laser either in integrated or hybrid approach to achieve a large tuning range. Most of the currently available MEMS mirror devices use the top silicon surface of the wafer as the reflecting surface. Many applications, such as ECLs, optical tomography, and optical filters, however, would greatly benefit from in-plane translational or rotational mirror movement. Use of the top silicon surface as mirror poses operational limits for these applications and makes the integration and packaging of the complete systems very difficult. Vertical MEMS mirrors with in-plane movement provide the flexibility needed in those applications.

The first goal of my research was to develop MEMS actuators with sufficiently large displacement that will enable tuning of ECLs over a significant portion of the spectral bandwidth of the gain medium. This led to the development of different types of MEMS actuators as required by ECLs in Littrow or Littman configuration. The next step was to integrate the MEMS actuators with optical components, such as micro-mirrors. A micro-mirror can be fabricated at the same time as the MEMS device or can be made separately and mounted after actuator fabrication, especially if a larger mirror is required. If optical components are to be micro-fabricated, it is necessary to develop a process to produce a

silicon sidewall surface of optical quality. A further aspect is the placement and alignment of integrated and discrete components, such as lenses, mirrors, and gratings, which may put further constraints on the MEMS device specifications. The final goal of my research was to demonstrate a complete MEMS system with an integrated micro-mirror that is capable of reflecting light and which can be used in ECLs in either Littrow or Littman configuration. During the course of this PhD research, I took part in numerous meetings with the collaboration partners, in which progress and obstacles were discussed. During these meetings, design strategies for a particular aspect were sometimes changed, depending on findings in other areas of the research project. In my PhD thesis, I present an evolution of the original MEMS actuator design, which was driven by the requirements and findings of the other sub-projects.

1.7 Outline of the Thesis

The work that I have accomplished to achieve the thesis objectives is described in the following six chapters. In this first chapter, the research background and motivation are described, and an introduction of tunable diode lasers and MEMS technology is given, followed by a brief summary of the research plan for the project. The rest of the chapters is organized as follows:

Chapter 2 addresses different types of MEMS actuators and the basic theory of an electrostatic actuator. This chapter also discusses the impact of MEMS devices on the design of ECLs and previous studies that have influenced my work.

Chapter 3 describes the design, modeling, and analysis of the designed large displacement MEMS rotary actuator. It also includes details about the fabrication procedure and voltage-displacement characterization of the actuator.

Chapter 4 presents the design of a virtual pivot point actuator for use in a Littman cavity ECL configuration. First, the design concept to achieve a virtual pivot of rotation is covered and then the analysis and fabrication procedure is described. The results from characterization of the actuator are also presented.

Chapter 5 covers the two processes that I have developed to smooth the etched surface of the actuator sidewall to achieve an optical quality silicon vertical micromirror. Two processes are discussed in detail and design and fabrication parameters are provided. This chapter also includes results from characterizations of the smoothed actuator sidewalls.

Chapter 6 introduces the evolution of a zipped comb drive to achieve an extremely long arm MEMS actuator. It also discusses a procedure to attach an external mirror on top of the extended arm of the MEMS actuator. The detailed mechanical characterization of the actuator is also presented in this chapter.

Chapter 7, the final chapter, summarizes the impact of the achieved work and discusses future potential research. The future work is broken down into two branches: (1) future plans for the MEMS tunable laser in the MIR region, and (2) other potential applications of the developed MEMS actuators.

2 MEMS Actuator: Background and Theory

2.1 MEMS Actuators

Some important applications of MEMS devices are in the areas of sensing, actuation and power generation. As sensor, a MEMS device can take a mechanical input and convert it to an electrical signal. Accelerometers are a common example of MEMS sensors that are used to detect an acceleration force. Other applications are gyroscopes, to detect change in mechanical orientation and various types of pressure sensors to measure tire or fuel pressure in automobiles, monitor blood pressure, or fluid flow etc. MEMS actuators, on the other hand, can take an electrical signal to affect mechanical motion, such as linear displacement or rotation. Micromirrors in digital projectors, nozzles and pumps in inkjet printers, auto focusing systems in digital cameras, headlight leveling and positioning mechanisms in automobile, precise dispensers in drug delivery systems are some examples of MEMS actuators being used in everyday life. A MEMS energy harvesting device generates power by exploiting, for example, strain or relative displacement [24, 25]. To achieve wavelength tuning in an external cavity laser, the cavity length needs to be changed by either linear displacement or rotation of a mirror or grating element. On a miniature scale, this task can in principle be conveniently achieved by a MEMS actuator.

2.2 Actuation Mechanism of MEMS Devices

A number of physical processes can be employed to generate the actuation force for MEMS actuators. The most common actuation mechanisms include use of electrostatic fields, magnetic fields, electro-thermal or even using the electromechanical properties of some materials, such as the reverse piezoelectric effect and shape memory alloy. Each actuation principle has its own advantages and disadvantages with respect to deflection range, power requirement, and response time. A brief overview is shown in Table 2-1[26-28].

Table 2-1 Different actuation mechanisms of MEMS actuators.

Actuation Mechanism	**Advantages**	**Challenges**	**Voltages/ Current**	**Typical Devices**
Electro-thermal	• Simple structure • Simple circuit	• Static power dissipation • Bandwidth limited by thermal time constant	• Few volts to tens of volts • mA to tens of mA	Microvalve [29]
Electrostatic	• High accuracy • Works better at micro scale • Easy to fabricate	• Relatively small force • Better operated in vacuum	• Tens of volts to hundreds of volts • nA to few mA	Micromirrors [22]
Magnetic	• Larger	• Harder to	• Low volts	Microscanner

	displacement • Can operate in harsh environment	fabricate on micro scale • High current, power dissipation	• Hundreds of mA	[30]
Piezoelectric	• Can create large force • Better for vibration and resonance	• Small displacement • Hysteresis	• Tens of volts to hundreds of volts • nA to few mA	Micropump [31]
Shape memory alloy	• Light weight and small space	• De-actuation slow • Fatigue over time	• Tens of mA to few Amps	Micropump [32]

The electrostatic force is a very commonly used actuation mechanism for microstructured devices. One of the main reasons that favors the electrostatic mechanism over others is that the electrostatic force scales more favorably in the micro-scale range [33]. Other advantages of electrostatic actuators are small size, low power consumption, high actuation speed, good fabrication compatibility, and relatively high displacement.

2.3 Theory of Electrostatic Actuation

Electrostatic actuation can be achieved by the capacitive action between two electrodes. There are two main types of electrode configuration found in literature on which electrostatic actuators are based. Figure 2.1 shows these two basic forms, i.e. the parallel plate (Figure 2.1(a-b)) and the interdigitated (Figure 2.1(c-d)) configuration. The energy, *E*, stored in a capacitor is given by:

$$E = \frac{1}{2}CV^2 \qquad \textit{Equation 2.1}$$

Here, C is the capacitance and V is the applied voltage between the electrodes. The electrostatic force is the derivative of this energy with respect to the pertinent direction. The electrostatic force for electrode movement in a particular direction can be expressed as:

$$F = \frac{\partial E}{\partial x} = \frac{1}{2}V^2\frac{\partial C}{\partial x} \qquad \textit{Equation 2.2}$$

Equation 2.2 reveals that the force in an electrostatic actuator is proportional to the change of capacitance between the electrodes. The electric flux distribution for an idealized parallel plate capacitor is shown in Figure 2.1(a). The capacitance between the electrodes is given by:

$$C = \frac{\varepsilon A}{z} \qquad \textit{Equation 2.3}$$

where ε is the permittivity of air, z is the distance between two electrodes and A is the electrode surface area.

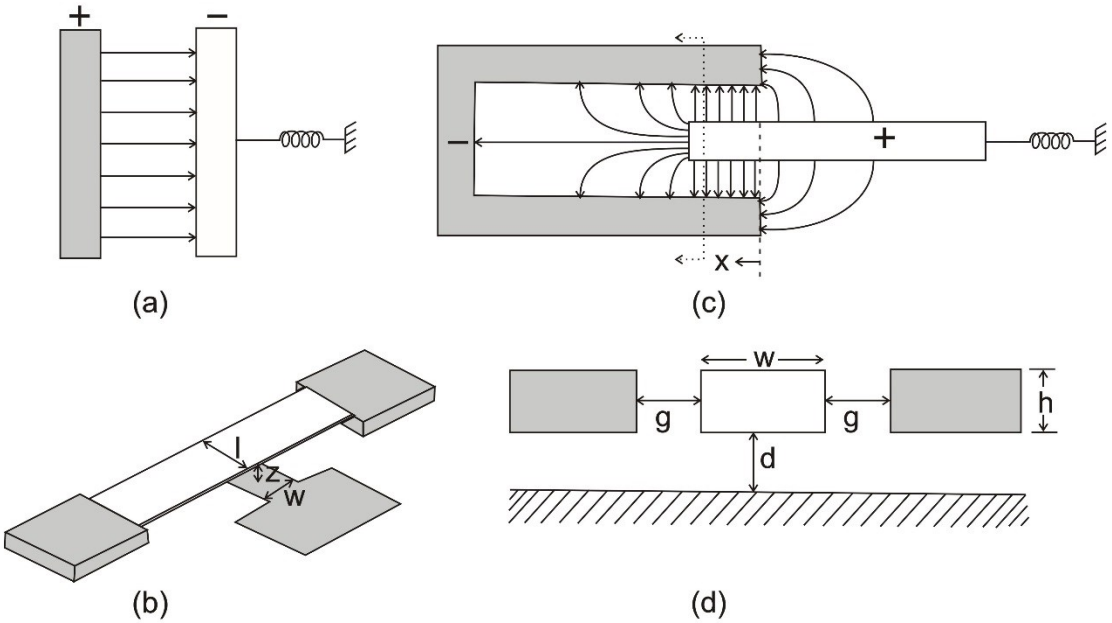

Figure 2.1 Basic forms of electrode combination in electrostatic actuators and their electric flux distributions.

In the parallel plate electrode configuration, the electrode can move only in a single direction (i.e. the *z*-direction in Figure 2.1b). Therefore, the force generated in this configuration is given by:

$$F_z = -\frac{\varepsilon w l V^2}{z^2} \qquad \textit{Equation 2.4}$$

where w is the width and l is the length of the overlap area of the electrodes. Similarly, the force induced in an interdigitated comb drive can be calculated from the change of capacitance with the lateral displacement of the structure. The electrostatic flux distribution between the electrodes of an interdigitated comb drive is shown in Figure 2.1(c). From this figure, the capacitance between the fixed and moving electrodes can be modeled by two capacitors — one is due to the normal field between the parallel combinations of two

electrodes (C_n) and the other is due to fringing field between the two electrodes (C_f). C_n is linearly proportional to the translational displacement of the two electrodes. The fringing field, however, is almost independent of displacement and depends on the dimensions of the electrode such as height (h) of the electrode, separation between the electrodes (g), and the distance between lower end of electrode and the substrate (d). The normal capacitance and its derivative in the translational direction are given by:

$$C = \frac{2\varepsilon x h}{g} \qquad \textit{Equation 2.5}$$

$$\frac{\partial C}{\partial x} = \frac{2\varepsilon h}{g} \qquad \textit{Equation 2.6}$$

Here, x is the overlap between the two electrodes (as defined in Figure 2.1(c)), h is the electrode height, and g is the separation between the two electrodes. The capacitance due to fringing field is normally determined with the help of simulations as it changes based on the size, shape, and geometry of the electrodes. Tang [34] simulated the effects of different electrode parameters for interdigitated comb drives using the finite element method and calculated the changes of capacitance for translational movement between the electrodes including fringing fields and fitted it to an empirical formula which is given by:

$$\frac{\partial C}{\partial x} = \frac{2\alpha\varepsilon h}{g^{\beta}} \qquad \textit{Equation 2.7}$$

Two adjustable parameters, α and β, are introduced in Equation 2.7 to account the fringing electric field between the interdigitated electrodes. The value of α and β for variation of h, d and w were simulated in details in Tang's PhD dissertation [34] to determine their effect on

fringing electric field and a table (Table 2-2) was presented for variation of electrode height which has the largest contribution in fringing electric field.

Table 2-2 Value of α and β for different h from simulations [34].

Parameter	h = 1 μm	h = 2 μm	h = 4 μm	h = 8 μm	h = 12 μm
α	2.19	1.61	1.33	1.17	1.12
β	0.78	0.85	0.89	0.93	0.95

Further increase of h leads the value of both α and β close 1 as expected of a two identical, idealized parallel plate capacitor. The induced electrostatic force in interdigitated comb drive can be derived by inserting Equation 2.7 into Equation 2.2 and can be expressed as:

$$F = \frac{\alpha \varepsilon h V^2}{g^\beta} \qquad \textit{Equation 2.8}$$

2.4 Choice of MEMS Electrostatic Actuator for an ECL

An electrostatic actuator is usually made of two or more conductive electrodes separated by an air or dielectric layer and driven by a voltage source or a charge pump to create a static electric field between and in the surrounding medium of the electrodes. The force imparted onto each electrode results from the electrostatic field acting on the free charge of that electrode. There are many different types and designs of MEMS electrostatic actuators described in the literatures. Based on the electrode movement and suspension design, electrostatic actuators can be categorized into gap closing actuators, where the electrode

spacing decreases, and actuators in which the electrode overlap increases upon actuation. A schematic diagram of a 'decrease in electrode spacing actuator' is shown in Figure 2.2(a).

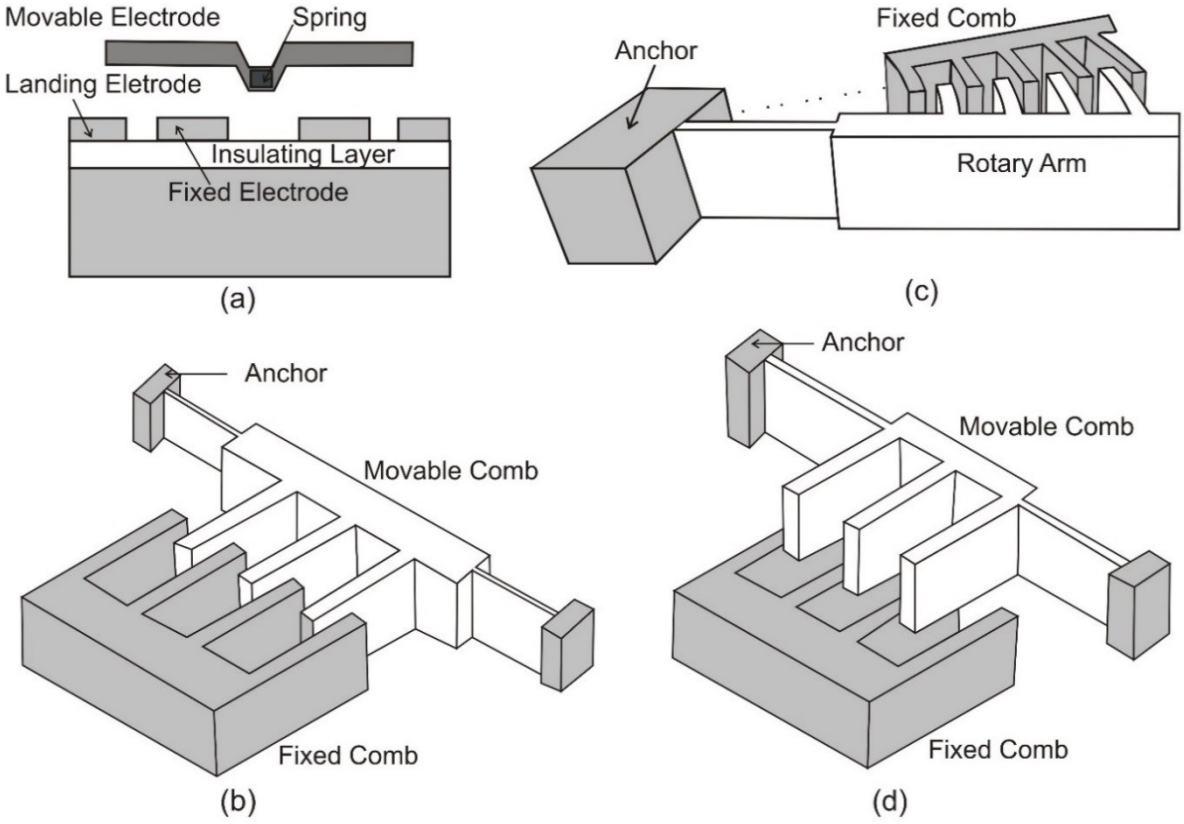

Figure 2.2 Different types of electrostatic actuators.

This type of actuator is often used in MEMS design because of its simplicity and, partly, its compatibility with surface micromachining. Typical examples of this type of actuator are parallel plate designs and micromirrors. There are some drawbacks of the 'decrease in electrode spacing actuators' despite its popularity. They have a highly non-linear relationship between extent of displacement and actuation voltage (as seen from Equation 2.4). Also, electrical pull-in can happen when the displacement or rotation passes a critical point,

irrespective of spring design. The pull-in effect limits the range of displacement or rotation and an external circuit control is required to avoid snapping of the beams. Since the development of the interdigitated comb drive, there has been a major shift from ‘decrease in electrode spacing actuators’ to ‘increase in electrode overlap actuators’ in MEMS design. This type of actuator exhibits less pull in effect and it can be designed to have a linear relationship between displacement and voltage. Electrostatic actuators can also be categorized based on their movement — translational and rotational actuators. Figure 2.2(b) and Figure 2.2(c) illustrate the simplest examples of these two types of actuators. With the evolution of bulk micromachining technology, electrostatic actuators can be designed in more and more versatile ways to meet the application requirements. They can be designed in single or multiple structural layers and can provide in-plane or out-of-plane movement. Figure 2.2(d) shows an example of multiple layer and out-of-plane movement actuators known as staggered comb drive actuators [35, 36].

To select the type of actuator suitable for tuning of an ECL, let us study the ECL configuration with grating (see Figure 1.2). To tune the wavelength of the ECL, the rotating element (grating for Littrow or mirror for Littman configuration) needs to be rotated so that the center wavelength of the grating filter that is fed back into the gain medium is changed. But the rotation and translation of the rotating element should occur in such a way that the cavity mode stays aligned with the grating filter for continuous mode-hop-free wavelength tuning. This can only be achieved if the rotating element is rotated about a pivot point that is located at the intersection of the line through the rotating surface and the normal to the optical axis, at a point that is a distance of $n \times \lambda$ from the rotating element along the optical axis (n is the number of wavelengths in the cavity and λ is the wavelength) [14, 37]. A rotary MEMS

actuator that can provide in-plane rotation about a pivot point is thus suitable for use in an ECL. One limitation of the Littrow configuration is that the wavelength tuning range cannot be very large because of the different frequency selection methods of the two interacting filters, i.e. the cavity length and the grating angle, if the pivot point for the grating rotation is fixed. To overcome this problem, the position of the pivot point should be moved with the rotation of the grating. However, this is very difficult to realize because of the complicated mechanical structures required. In contrast, the geometric arrangement of Littman scheme does not impose any constraint to the tuning range and a large tuning range can be easily obtained with a fixed pivot point. The specific ECL configuration plays thus a major role in designing the characteristics of rotary comb actuator.

2.5 Tuning Principle of a MEMS ECL

The physics of tuning of a diode laser in the presence of external optical feedback has been extensively studied and reviewed in [38-40]. In the presence of external back-reflection of light, the output laser frequency changes with the change of the external cavity length L (as shown in Figure 2.3). Under weak feedback conditions, the shift of emission frequency from the center frequency was derived in [38-40] , and is given by:

$$\Delta\lambda = \frac{\lambda_0^2}{2\pi L}\frac{C\sin(2\pi\tau_L\nu_0 + \arctan(\alpha))}{1 + C\cos(2\pi\tau_L\nu_0 + \arctan(\alpha))} \qquad \textit{Equation 2.9}$$

Here, λ_0, v_0 and L are the central wavelength, frequency and external cavity length respectively, τ_L is the roundtrip propagation delay of light due to the EC given by $\tau_L = 2L/c_0$ (c_0 denotes the speed of light in vacuum), α is the equivalent linewidth enhancement factor given by $\alpha = \alpha_0/\Gamma_0$ (α_0 is linewidth enhancement factor of the gain medium and Γ_0 is the optical confinement factor). The term $C = (L/\mu_0 d_0)\xi\sqrt{(1 + \alpha^2)}$ represents the external feedback strength, where μ_0 is the refractive index of the laser gain medium, d_0 is the length of the internal laser cavity and $\xi = r_3(1 - r_2^2)/r_2$ is the relative reflectance of the external mirror. Here, r_2 is the reflectance of the laser facet facing the external mirror respectively, but r_3 is the coupling efficiency of the EC considering external mirror reflectance and coupling losses (due to the mirror misalignment and the spreading of a laser beam, for example).

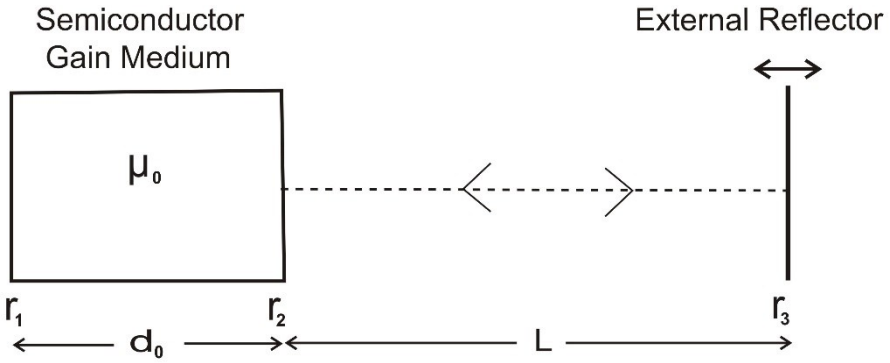

Figure 2.3 Schematic diagram of a diode laser with external feedback.

The combination of MEMS devices and tunable diode lasers may further affect the tuning behavior of the external cavity laser. In particular, the small size of the MEMS devices lead to further requirements, such as short cavity length and high coupling efficiency. The adaptation of conventional laser theories has also been studied for MEMS cases [40, 41]. The dominant

factors that distinguish MEMS based lasers from conventional ones in terms of tuning behavior such as the continuous tuning range, stability of tuning and mode hopping range, are the short cavity length and the high coupling efficiency. Equation 2.9 shows the basic relationship between the wavelength shift and the change of the external cavity length for a conventional laser. The derivation of Equation 2.9 is based on one explicit assumption, i.e. ξ <<1 which requires r_3 << r_2 (called the weak feedback condition), and two implicit assumptions: single longitudinal mode emission of laser and small tuning condition applies. However, for MEMS based ECLs, the external cavity can be extremely short and the assumption $r_3 << r_2$ may not always be valid. An extension of the model was presented to cover both the weak and medium feedback regions based on the assumption that $r_3 r_2 << 1$ [41]. This model is more suitable for some MEMS lasers, especially those with extremely short cavity and high feedback coupling efficiency. The wavelength shift in the medium feedback condition can be expressed as [41]:

$$\Delta\lambda = \frac{\lambda_0^2 T_0^2}{2\pi c} \frac{\alpha ln T_0 + \arcsin[\xi \sin(2\pi\tau_L \nu_0)/T_0]}{t_d T_0^2 + \tau_L \xi[\xi + \cos(2\pi\tau_L \nu_0) - \alpha \sin(2\pi\tau_L \nu_0)]} \qquad \textit{Equation 2.10}$$

where $T = \sqrt{(1 + \xi^2 + 2\xi\, cos(2\pi\, \tau_L\, \nu))}$ and $T_0 = T_{\nu=\nu_0}$ represents the value of T at $\nu=\nu_0$, $t_d = 2d\bar{\mu}_e e/c_0$ is the group round-trip delay in the lasing cavity and $\bar{\mu}_e$ is the effective group refractive index. One of the most important parameters of the tunable laser is the shift range $\Delta\lambda_r$ which was derived by Liu from Equation 2.9 and is given by [40]:

$$\Delta\lambda_r = \frac{\lambda_0^2}{2\pi} \frac{A_0}{\frac{1}{r_3^2} - A_0^2 L^2} \qquad \textit{Equation 2.11}$$

Here, $A_0 = (1 - r_2^2)\sqrt{(1 + \alpha^2)}/r_2\mu_0 d_0$ is a variable determined by the parameters of the internal laser cavity. Equation 2.11 directly links the wavelength shift to the external mirror reflectance and the external cavity length. Higher coupling efficiency results in a larger shift range for a given cavity length.

2.6 State of the art of MEMS Actuator for an ECL

The use of MEMS actuators to tune the wavelength of a variety of semiconductor lasers, such as vertical cavity surface emitting lasers (VCSEL), DFB lasers or edge emitting semiconductor lasers, has been widely reported in literature. The top and bottom mirrors of a VCSEL are usually two oppositely doped distributed Bragg reflectors and the cavity layer, which consists of the active region and an air gap, is in between. Micromachined movable mirrors, suspended by a soft beam, such as cantilever beam or membrane, have been used as the top reflector of the VCSEL cavity to tune the wavelength [42, 43]. However, the achieved tuning range reported in literature so far is only around 30 - 40 nm [44]. VCSELs also do not have sufficient space to support additional optical components because of their extremely short cavity. Another laser technology where MEMS actuators have been employed is DFB laser. MEMS rotational mirrors were used to select a wavelength from an array of DFB lasers to produce tunable lasers [45]. A parallel array of DFB laser is formed with each laser having a slightly different grating pitch. Thus each laser lases at a slightly different wavelength and a range of wavelength can be achieved. Only the laser with the particular wavelength of interest is activated by the MEMS mirror and thus wavelength tuning is performed. The problem of this technology is cost and insertion loss. The number of lasers needed to cover a wide tuning range is prohibitively large and makes this technology

impractical for wide tuning ranges. Moreover, coupling of N lasers into one output waveguide is very difficult and results in very low efficiency. The present tendency is to use edge-emitting lasers that make use of MEMS technology to construct external cavities for wavelength tuning.

A comb drive actuated external mirror used to tune a semiconductor laser diode was demonstrated in the literature back in 1996 [46]. The maximum displacement of the actuator was 10 μm and the achieved wavelength tuning range was ~20 nm. However, the mirror and actuator were fabricated by nickel plating which is not quite a good material for actuation in terms of voltage-displacement and mass-frequency ratio. It will also bring incompatibility with other electronics integration in the same chip. Zhang demonstrated another tunable laser using a micromirror actuated by a two stage lateral comb drive actuator [13]. The whole structure was fabricated by employing surface micromachining processes. After fabrication and release steps, the micromirror was uplifted to the vertical position and held in place by position holders. A tuning range of 16 nm was obtained with just few micron displacement of the actuator. The same group then developed an improved version of the MEMS design where a 75 μm circular mirror was fabricated by deep etch and actuated by a lateral comb drive to focus the diverging laser light. This led to an improvement in the feedback coupling efficiency [12]. Deep etching technology offers more advantages than surface micromachining technology to fabricate MEMS structures for tunable lasers since it can provide larger thickness and produce various vertical optical components such as flat mirrors, circular mirrors, gratings or microlenses as well as some trenches and guides for optical alignment. Though high compactness and reasonable tuning range was achieved, the laser could generally be operated only in multiple longitudinal modes. The use of rotary comb

actuator to rotate a microfabricated blazed grating was reported in the same literature to overcome the mode-hopping problem and the laser was operated nearly in single longitudinal mode. A rotary comb actuator was also used to tune the wavelength of a tunable laser in Littrow configuration and a mixed mode injection-locked tunable laser [47, 48]. Tuning ranges around 30 nm were achieved in both cases. MEMS actuators have also been reported to tune the wavelength of Littman configured tunable lasers. Huang *et al.* used a lateral comb drive with flexure to rotate a mirror for tuning of the wavelength [49]. Berger *et al.* fabricated a complex rotary actuator to rotate a mirror that was mounted on top of the actuator to tune the wavelength in the range of 40 nm [50].

Most of these developed MEMS actuators have limitation in terms of design, displacement or rotation and surface quality of optical components that limits the tuning ranges to around 50 nm. These MEMS based lasers fall mostly into the near infrared or within the telecommunication band and no work on MEMS driven tunable MIR lasers has so far been reported. There is, therefore, an urgent need for increased efforts in research and technological developments in this regime. There are mainly three reasons that limit the wavelength tuning of ECLs: emission bandwidth of the gain medium, maximum displacement of the actuator and reflectivity of the external surface. While an increase of the emission bandwidth of the gain medium is not the focus of this research, there is still room to develop MEMS actuators with increased displacement or rotation and innovative design for variant ECLs configuration, and improve the optical quality of the surface of micromachined mirrors and gratings surface. In this PhD research, I focused on developing MEMS actuator with optical quality vertical surface for both Littman and Littow configuration ECLs. The MEMS

devices will support building ECLs in both integrated or hybrid approach based on application system requirements.

2.7 Summary

MEMS actuators, their actuation mechanisms as well as advantages and disadvantages were discussed in this chapter. Electrostatic actuators were found to be the most suitable for application in external cavity lasers and the theory of electrostatic actuation was presented. Different types of electrostatic actuators were analyzed with respect to their application in external cavity lasers. The effect of implementation of MEMS technology on the tuning characteristics of an ECL was discussed and a detailed review of the MEMS electrostatic actuator in the design of external cavity laser was given. These analyses and reviews form the foundation for the design of my MEMS rotary comb actuators to build an external cavity laser. In next chapters, I will present the design, fabrication and characterization of developed MEMS actuators suitable for building an external cavity laser in Littrow or Littman configuration.

3 Design and Fabrication of a MEMS Rotary Comb Drive Actuator[1]

3.1 Introduction

In this chapter, the design and fabrication of a rotary comb-drive electrostatic actuators are described. MEMS based rotational comb-drive actuators are of great interest because of their applications in a wide variety of systems involving external cavity laser, optical switching and attenuation, interferometry, micro-gear actuation, gyroscopes and energy harvesting microstructures [12, 15, 25, 40, 51, 52]. In a rotational actuation system, a movable comb arm consisting arcuate comb fingers is anchored with a beam, and actuated through an electrostatic force from another fixed comb arm with interdigitated arcuate comb fingers. Optical applications of rotary comb-drive actuators involve either the attachment of an optical component on the rotary arm [48] or patterning optical component on silicon sidewall using micromachining [12].

---

[1] This chapter is a modified version of the first part of the paper*: M. Q. Huda, T. M. F. Amin, Y. Ning, G. McKinnon, J. Tulip, and W. Jäger, "Rotary MEMS comb-drive actuator with smooth sidewall for photonic applications," Journal of Micro/Nanolithography, MEMS, and MOEMS, vol.11, p. 023012, 2012.

*My contribution: I performed the design of the actuators and all the necessary simulations to optimize and verify the design. I fabricated the devices using wet release method which is different than the method that was described in the paper. I also developed the smoothing process of the sidewall that was presented in the paper, which is included in chapter 5 of this thesis.

The rotation of the actuator depends on the electrostatic force generated by the comb fingers and the spring design of actuator. The amount of rotation or displacement of the actuator and its structural stability sometime determine the type of applications where the actuator can be used. Many applications require very small displacement for their operation such as optical switching whereas applications like external cavity laser requires very large rotation or displacement for better operation. Requirements of larger angular rotation in an actuator can be met by the use of multiple sets of comb arms connected together through a system of suspension springs in a circular arrangement. A structure with four sets of arms and a deflection of 7 degrees at a voltage of 180 V has been reported [51]. Use of twelve sets of comb arms for a 1 mm radial structure has resulted in 2.5 degrees of rotation with a low voltage of 5 V [52]. However, in many integrated systems with optical path alignment requirements, such as external cavity lasers, multiple sets of comb arms in a circular arrangement would effectively block space for any optical components. Sufficient space for the optical components between the gain chip and the actuator is necessary if the MEMS structure to be implemented into a hybrid system.

In this research, a rotary comb-drive electrostatic actuator consisting of a single rotary arm of 2 mm length with an angular deflection of 3 degree is presented. The fabricated structure provides a long movable truss that is accessible for hybrid integration. The fabricated structures can be reliably operated in the kilohertz (kHz) range.

3.2 Device Design and Electromechanical Analysis

A systematic approach was taken in designing and simulating the rotary comb-drive actuators with arm lengths of up to 2 mm and angular deflection of up to 3 degrees. System parameters were carefully designed to meet our requirement of larger deflection of the beam with stable operating performance in the kHz range. A schematic drawing of the rotary comb drive actuator is shown in Figure 3.1. All the comb fingers with radial profiles and other moving structures are supported by a beam of dimensions (L, w, h) to an anchor point. Another set of fixed comb fingers, attached with the base layer, is interdigitated with the rotary fingers with an overlapping angle θ_i and maintaining a fixed radial gap g with the moving fingers. The angular movements of the rotary arm are described by θ and γ, which represent the in-plane (yaw) and out-of-plane (pitch) displacements, respectively. The rotary comb structure was designed with long rotary arm for enabling its use in optical application. The forces generated in radially outward and in-plane moving directions is determined by the derivatives of the electrostatic energy due to capacitive effects between stationary and movable fingers.

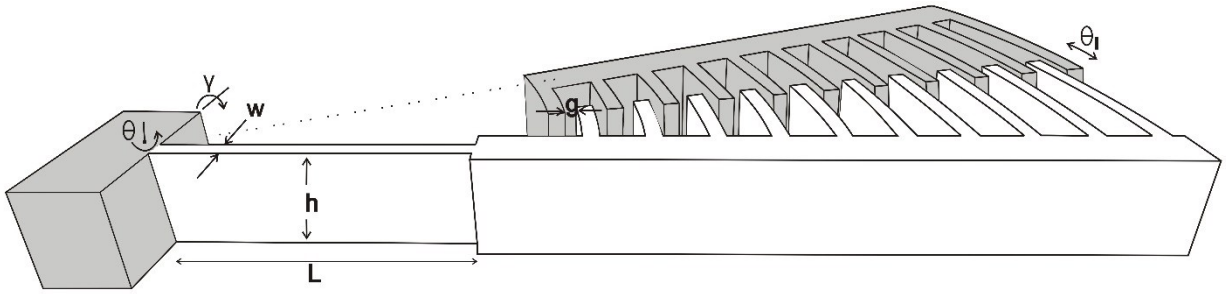

Figure 3.1 A schematic diagram of the rotary comb actuator (Fixed portion are shaded).

The in-plane force in the x direction can be derived using Equation 2.8 and is given by:

$$F_x = \frac{N\varepsilon h V^2}{g} \qquad \textit{Equation 3.1}$$

Here, N is the number of moving comb fingers of the structure. Both α and β parameter of Equation 2.8 are considered to be 1 due to high thickness (≈ 100 μm) of the structure. Unlike linear translational comb drive, rotary comb drive usually has some radial force due to different overlap area on both sides of the comb fingers. The radial force can be calculated as:

$$F_r = \frac{\varepsilon h V^2}{g^2} \sum_{i=1}^{N} R_i \, \theta_i \qquad \textit{Equation 3.2}$$

Where R_i and θ_i are the radius and angular overlap of i^{th} comb fingers, respectively. An important parameter, the effective electrostatic spring constant [53] can be derived as:

$$K_e = \frac{\partial F_r}{\partial g} = \frac{2\varepsilon h V^2}{g^3} \sum_{i=1}^{N} R_i \, \theta_i \qquad \textit{Equation 3.3}$$

For stable operation without snapping of fingers, the value of K_e needs to be smaller than the mechanical spring constant in radial direction, given as:

$$K_r = \frac{Ewh}{L} \qquad \textit{Equation 3.4}$$

Here, L is the length of the beam and E is the Young's modulus of elasticity of the beam material. The structure should have reasonably low stiffness in the working direction to get the desired rotation within the operating voltage. On the other hand, a large stiffness is required in the out of plane direction to avoid any undesired vibration from by surrounding effects. The stiffness ratio for the pitch-yaw movement is given by:

$$\frac{K_\gamma}{K_x} = \left(\frac{h}{w}\right)^2$$ *Equation 3.5*

The actuator is designed with high thickness to ensure the in-plane movement of the rotary arm without noticeable out-of-plane bending. A cantilever beam is used as a restoring spring element to balance the electrostatic force. According to Hook's law, force generated in a spring element is given by:

$$F_{spring} = Kx$$ *Equation 3.6*

Where K is the spring constant in the moving direction and x is the displacement of the spring. In this design, K is the spring constant of the cantilever beam in the x direction. For a cantilever beam with applied point force at its tip, the spring constant is given by:

$$K_x = \frac{3EI}{L^3}$$ *Equation 3.7*

Here, I is the area moment of inertia of the beam ($I = \frac{1}{12}hw^3$). In our design, the generated force by the comb fingers are distributed along the truss, not like a typical design with point force at the beam tip. Figure 3.2(a) shows a 2-d picture of the rotary comb actuator showing the distribution of force generated by the comb fingers. A simplified model with a point force F_x, equivalent to the total force generated by all the comb fingers, and applied at the middle position of the comb fingers span length, is shown in Figure 3.2(b). The displacement at the farthest end of the actuator can then be solved using moment area method [54] and is given by (please see Appendix A for complete derivation):

$$x = \frac{4N\varepsilon V^2}{Eg}\left(\frac{L}{w}\right)^3\left[1 + \frac{L_F}{\frac{L}{3}} + \frac{L_x}{\frac{2L}{3}} + \frac{L_F^2}{\frac{L^2}{3}} + \frac{L_F L_x}{\frac{L^2}{3}} + \frac{L_F^2 L_x}{\frac{2YL^3}{3}} + \frac{L_F^3}{YL^3}\right] \qquad \textit{Equation 3.8}$$

Where L_F and L_x represent the distance from beam tip to the force position, and from force position to the end of the truss, respectively. Putting L_F and L_x zero in Equation 3.8 transformed it into the displacement equation of a simple cantilever beam with force at its tip.

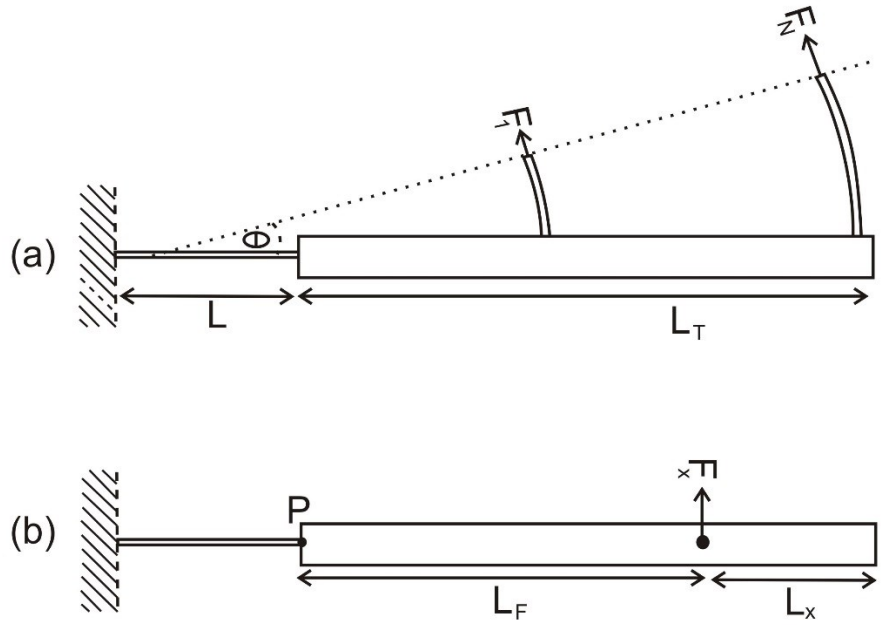

Figure 3.2 (a)The rotary comb actuator showing force generated by comb fingers; (b) A simplified model with a point force equivalent to the total force generated by all comb fingers and applied at the middle position of fingers span length.

The design constraints provided by the equations Equation 3.1 to Equation 3.8 are the limiting factor for designing rotary comb-drive actuator system with large deflections. The thickness of the device has little influence on deflection, rather it provides a larger stiffness ratio for the out of plane movement. However, increasing the thickness of the structure would increase the overall mass with a concomitant reduction of the resonance frequency. Apart from that, realizing higher aspect-ratio comb fingers, while maintaining a smooth vertical sidewall, has practical limits in deep reactive ion etching (DRIE) processes [55-58].

For this work, I confined the analysis to devices with heights of up to 100 μm. The gap between the comb fingers plays an important role in generating the actuation force. As evident from Equation 3.1 and Equation 3.3, a reduction of the finger gap increases the in-plane force, but also increases the electrostatic spring constant with the third power. The finger gap also needs to be correlated with the device height, in terms of a reasonable aspect ratio, for processing wafer. The finger gap was maintained at 5 μm for this design based on design requirements and processing consideration. The length to width ratio of the beam plays a significant role in beam deflection, as seen from Equation 3.8. However, larger values of the beam length reduce the radial stiffness of the structure with simultaneous increases in electrostatic stiffness, due to changes in the finger radii. A reduction of the beam width would also adversely affect the stability because of a reduction in rotational, K_x and radial stiffness, K_r. Thus controlling of the design parameters by careful design of mask and processing of silicon is very important during fabrication of devices.

Table 3-1 Device dimensions for virtual pivot actuators design

Beam Parameter, L x w x h (μm)	**Finger Parameters: width, gap (μm)**	**Total No. of Finger, N**	**Angular span of Moving Finger, θ (deg.)**	**Truss Width, (μm)**	**Total Length, (μm)**
210 x 7 x 100	8.2, 5	51	6.3	30	2030
225 x 7 x 100	8.2, 5	47	6.9	38	1535
250 x 6.5 x 100	8.2, 5	36	7.9	25	1105

3.3 Fabrication

Based on the above analysis, I designed rotary comb actuators system with the parameters given in Table 3-1. Three different designs were fabricated to get different amount of rotation, and different level of structural stability. The maximum arm length of the three designs varied from 1 mm up to a maximum of 2 mm. The devices were fabricated starting with silicon-on-insulator (SOI) wafer with a device layer thicknesses of 100 μm, buried oxide layers of 2 μm and a handle layer of 500 μm, as depicted in Figure 3.3(a)-(e). Bulk micromachining of the device layer followed by removal of the buried oxide using a single mask process was used in the fabrication process. Thick photoresist and oxide layers were used as mask for the high aspect ratio deep etches. At first, wafers were oxidized to a thickness of 1.8 μm using wet oxidation at a temperature of 1050 °C. The wafer was then spin coated with HPR 506 photoresist, and following exposure with ultra-violet light and development in Shipley Microposit 354 developer to pattern the photoresist. After photolithography, the pattern was transferred into the oxide layer through reactive ion etching (RIE) of the exposed oxide.

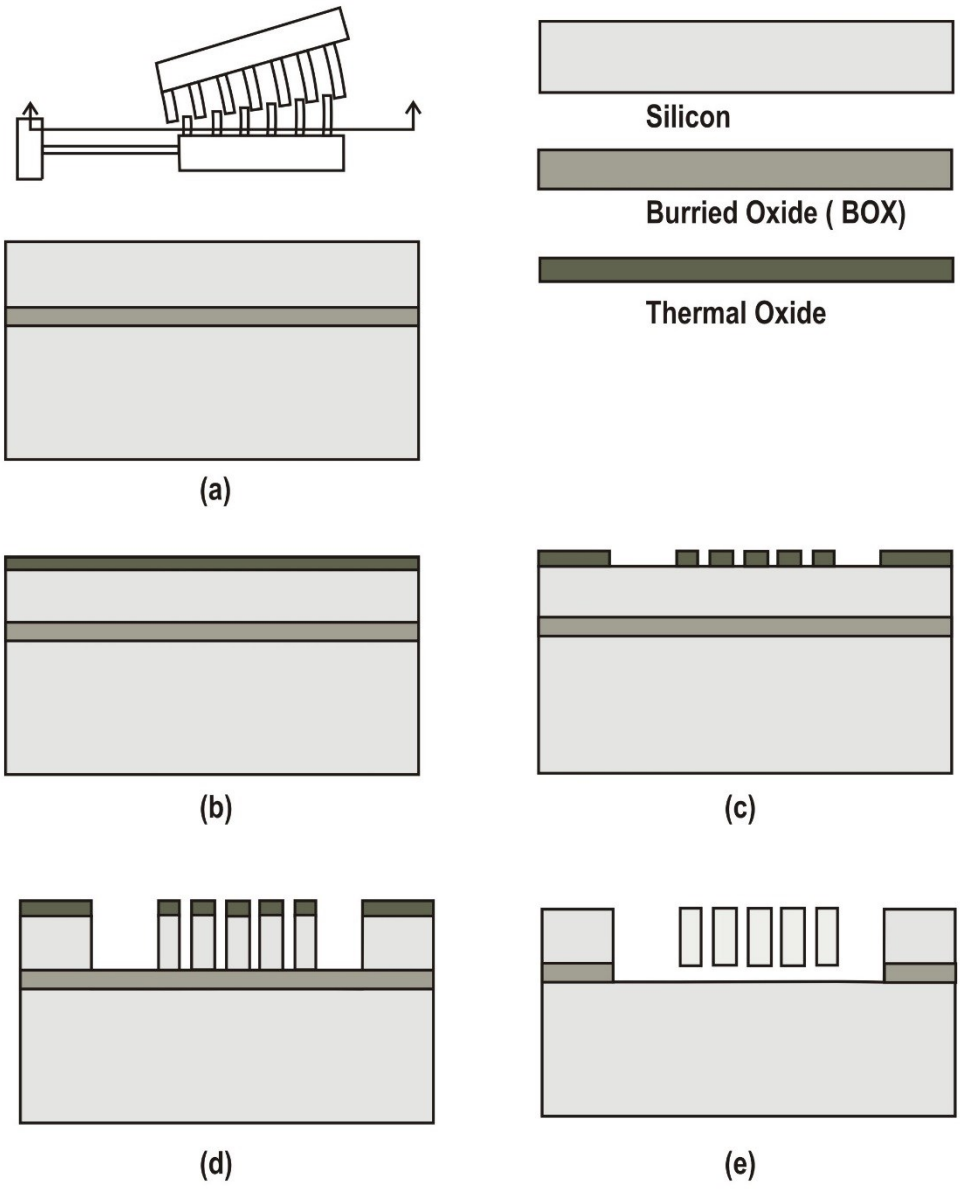

Figure 3.3 Process flow of rotary comb-drive actuator fabrication: (a) Initial SOI wafer; (b) Thermal oxidation; (c) Patterning (d) DRIE etching of device layer and; (e) BOX removal, device release and critical drying

At this stage, the wafer was diced into individual dies using a Disco DAD 321 dicing saw. After that, processing was performed by mounting 15-20 dies onto a carrier wafer in one batch. Deep reactive ion etching (DRIE) of those samples were performed using a STS ICP machine to define the pattern into the device layer. The sacrificial buried oxide was thus exposed and removed through wet etch process using buffered oxide etch (BOE) for 120 minutes. Release of the movable structure occurred through the completion of BOE of sacrificial oxide underneath the device layer. The released devices were then dried in a critical point dryer using liquid CO_2 super critical drying method. A thin layer of Cr (~20 nm), followed by a layer of Au (100 nm), were then deposited on the structure with a sputtering process to facilitate good electrical contact. The chromium layer helps to improve the adhesion of metal layer with the silicon substrate. A complete process flow for the MEMS rotary comb-drive actuator fabrication is given in Figure 3.3. SEM images of a fabricated device are shown in Figure 3.4.

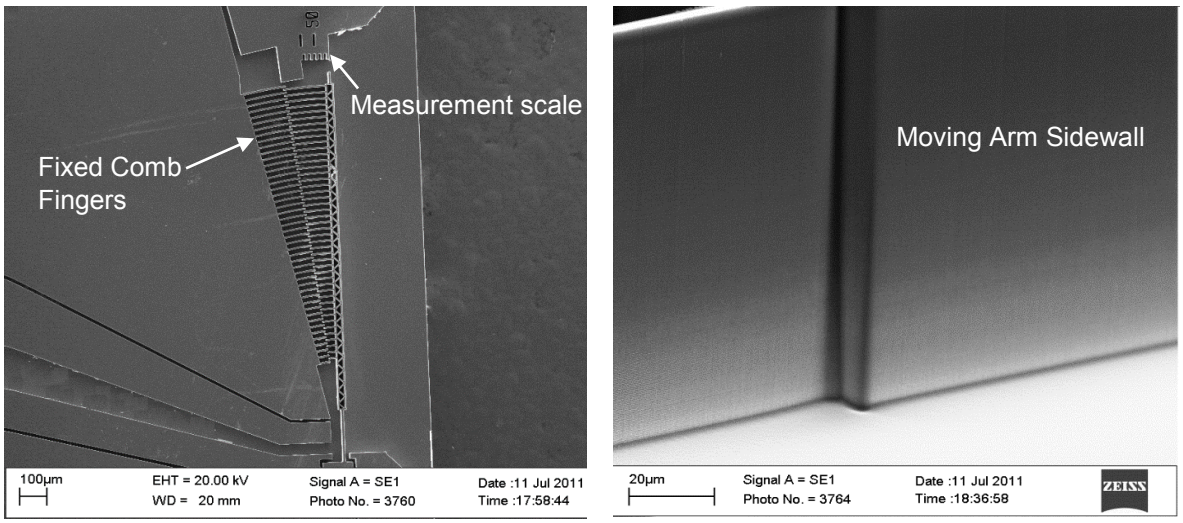

Figure 3.4 SEM images of the fabricated rotary actuator: top view (left), and (b) rotary arm from side (right)

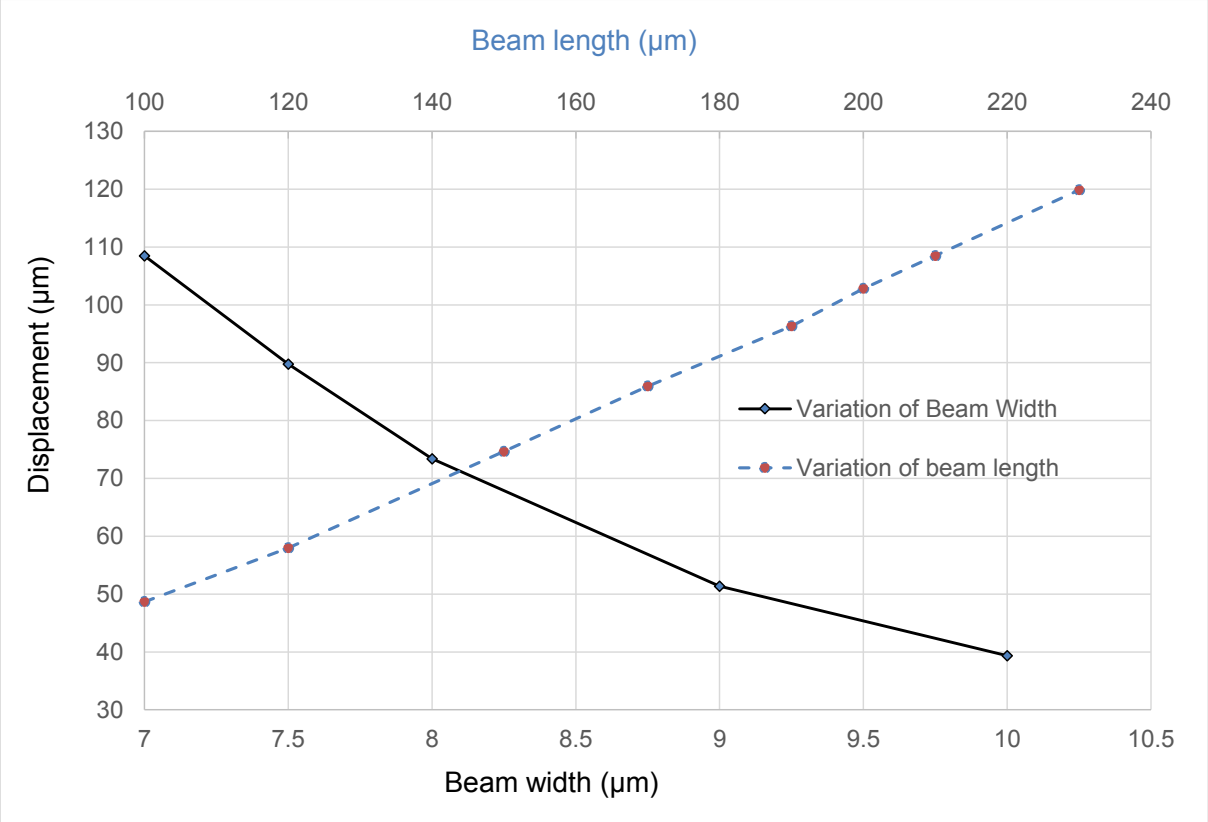

Figure 3.5 Simulation data showing displacement with variations of beam length and width

3.4 Results

The actuator structure was simulated using the simulation software Intellisuite [59] to verify analytical model, and optimize design parameters. The simulated results for various values of the beam dimensions at an applied voltage of 100 V are shown in Figure 3.5. The displacement at the end of movable arm is plotted against the beam width for a beam length of 210 µm. The simulation was performed only for points that have been shown by marker in the plot and the best fit of all the points estimated the dependence of displacement on beam

width as a polynomial function of power 2.9. The displacement results thus show strong influence of the beam width parameter, and closely follow the theoretical results of cubic behavior predicted in Equation 3.8. On the other hand, the displacement of the beam shows almost a linear behavior with the variation of beam length, and deviates greatly from the usual cubic relationship of cantilever beam. This deviation can be explained by the fact that a point force at the beam tip is considered for simple cantilever beam case, whereas force is applied far from the tip through a connecting truss in this design. The displacement is thus influenced by both beam length and the distance between the beam tip and force applied position, as shown in Equation 3.8.

The actuators were arranged as 8 mm x 4 mm chip, and a linear scale was inscribed just above the movable arm tip at each chip in the mask design to take experimental measurements. The bars on the inscribed scale have a separation of of 20 μm. After fabrication of the device, the displacement of the movable arm tip was measured using a wafer probing station. Experimental results was taken by observing the inscribed scale on the device with the help of an optical microscope (8X optical zoom) which is connected to a computer through a camcorder (up to 3X zoom). As the scale is linear, but the movement of the actuator is rotational, it is expected that there is some parallax error during the experimental measurements. The parallax error was estimated to be a maximum of ±5 μm (shown as error bars in the experimental plot in Figure 3.6) and the maximum error occurs at the largest displacement.

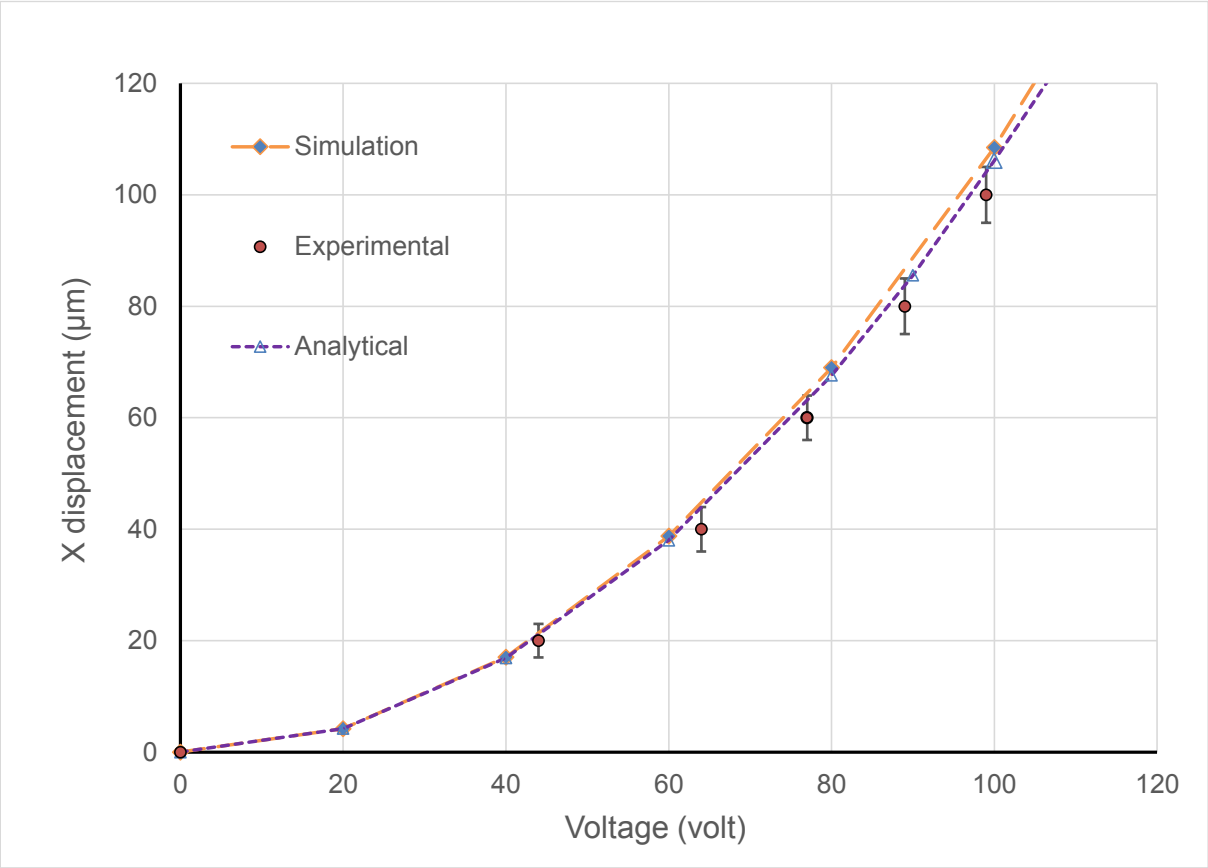

Figure 3.6 Experimental and simulated displacement as a function of actuation voltage.

The experimentally measured, analytically calculated, and the simulated displacements are shown in Figure 3.6 as a function of the actuation voltage. The results follow the theoretical relationship with the square of the applied voltage, but there are slight deviations among the displacements from the three methods. The slight deviation between simulated and experimental displacement is mostly due to the variation of the beam dimension from the wafer processing. The analytical model follows the simulated displacement more closely, and the slight deviation can be attributed to the fact that the truss is considered solid in the analytical calculation, but it contains grid holes in the real design which reduces the truss

strength. The largest displacement shown in Figure 3.6 (108 μm) corresponds to an angular deflection of 3 degrees at an applied voltage of 100 V.

3.5 Summary

In this chapter, I have described the design and fabrication of rotary comb-drive actuators with a maximum movable arm length of 2 mm. The devices were fabricated using a single-mask process by bulk-micromachining of front side. The maximum rotation of the actuators is 3 degree at an applied voltage of 100V which is sufficient to achieve a tuning range of over 100 nm. The device can operate in the kHz range, which is large enough for tuning frequency in many applications including spectroscopy. The actuator can be readily used in photonics applications by integrating optical components with the movable arm or using the sidewall of the movable arm with a reflecting surface of 2 × 0.1 mm. Sidewall smoothing techniques, which are developed and will be discussed in Chapter 5, can be applied to increase the surface quality of the etched sidewall. The actuators were also fabricated by my co-researcher [60] using a complex two level masking process involving employment of sidewall smoothing process and back cavity release technique [61]. The movable arm is then accessible in three dimensional geometry, and is suitable for chip level optical applications and implementations in hybrid structures.

4 Design and Fabrication of a Virtual Pivot Point MEMS Rotary Comb Actuator[2]

4.1 Introduction

In many optical applications, the optical path layout of the MOEMS system puts constraints on the actuator design. An ECL in Littman configuration is shown in Figure 4.1 as an example. The mirror orientation with respect to the grating is used to select the lasing wavelength. Continuous wavelength tuning in a Littman system is achieved by rotating the mirror about a pivot point. However, as can be seen in Figure 4.1, the arm of the rotating mirror in a Littman system blocks the optical path between the gain chip and the grating. The sidewall of the movable arm of a real pivot rotary comb actuator can therefore not be used as reflector in a Littman configured ECL and an actuator/mirror system with a virtual pivot point is required. In many cases, Littman configured ECLs are the preferred layout for ECLs,

[2] This chapter is prepared from the proceeding paper*: T. M. F. Amin, M. Q. Huda, Y. Ning, G. McKinnon, J. Tulip, and W. Jäger, "Design and fabrication of a virtual pivot point MEMS rotary comb actuator for optical applications," Proc. Of SPIE 8490, 8490D (2012).

*Note: An article prepared based on this proceeding and the 2-step oxide +BOE smoothing technique (discussed in chapter 5) has been submitted in the Journal of Micromechanics and Microengineering.

because of its advantages over the Littrow configuration, such as better out of band suppression and larger continuous tuning range. One major limitation of the Littrow configuration is that the wavelength tuning range cannot be very large (typically <30 nm) if the pivot for the grating rotation is fixed [40, 62]. The wavelength selection by the two filters in a grating based Littrow configured ECL is at mismatch for large grating rotation angles. In the grating filter, the wavelength variation is proportional to the sine of the rotation angle, whereas the wavelength change in the cavity filter is proportional to the tangential curve of

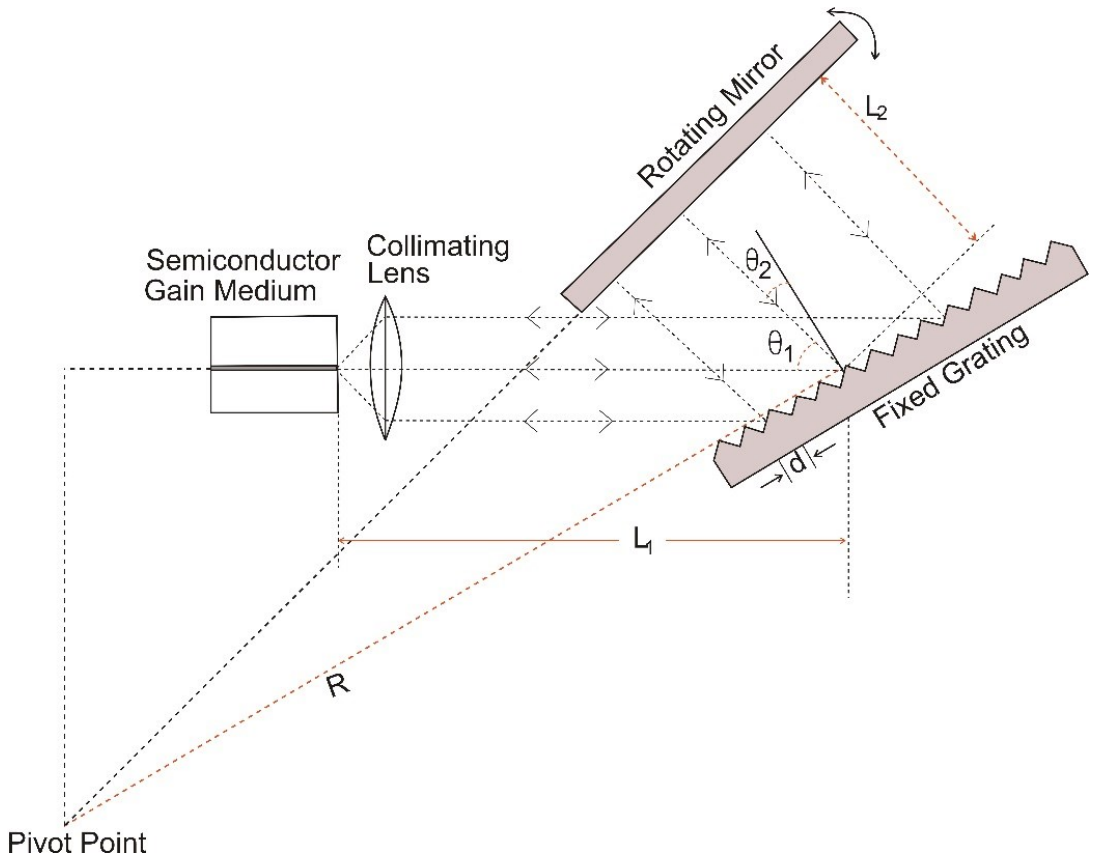

Figure 4.1 Configuration of an external cavity laser in Littman configuration.

the rotation angle. The problem can be resolved by moving the pivot position with the rotation of grating, which is, however, very difficult to realize due to the required complicated mechanical structures. In contrast, the geometric arrangement of the Littman scheme does not impose any constraints onto the tuning range, as the wavelength in both the grating and cavity filter changes as a function of the sine of the rotation angle. Thus, a large tuning range can be easily obtained with a fixed pivot theoretically in Littman configured ECLs.

A virtual pivot point (VPP) rotary comb actuator was first reported by Berger *et al.* [63], who attached an external mirror to a movable comb arm. The design of a virtual pivot actuator through the use of a MEMS flexure mount was also reported [49]. In this chapter, I present design and fabrication of a virtual pivot point rotary comb actuator with a distance of up to 2.8 mm between pivot point and physical device structure. This clearance will allow in-plane optical ray propagation and placement of required optical lens for collimation of light. This design also provides options for utilizing the sidewall of the movable arm as an optical mirror surface.

4.2 MEMS Actuator Design and Analysis

The requirement of angular movement about a virtual pivot point can be achieved through the use of folded truss in the actuator design [49, 64, 65]. The concept is shown in Figure 4.2. Figure 4.2(a) shows a structure where the movable comb-arm is attached to a beam flexure through a folded truss. Movement of the movable comb-arm, originating from

electrostatic beam deflection, occurs about a virtual center of rotation. However, as indicated in the figure, the virtual pivot point moves during the rotational movement of a single beam design. More control over the virtual pivot point of rotation can be achieved by the use of a structure with multiple beams, as shown in Figure 4.2(b). With a two (or more) beam configuration, a stationary virtual pivot point of the comb-drive can be achieved. A schematic diagram of the designed virtual pivot point MEMS rotary comb-drive actuator is shown in Figure 4.3. The device was designed with six sets of movable comb fingers which are connected through rigid arc-shaped trusses at the top and bottom of the device. The entire movable structure, consisting of the six sets of comb fingers, is anchored through three beams. These beams are positioned in a geometrical arrangement such that their extrapolated lengths intersect at the designed virtual point of rotation.

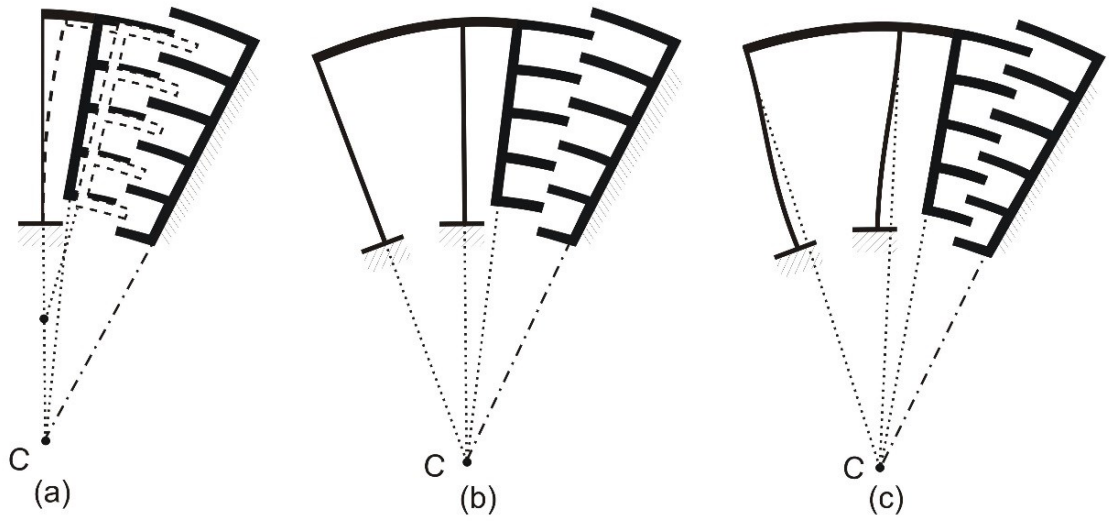

Figure 4.2 Virtual pivot point for folded cantilever structures: (a) general concept with single beam; (b) two or more beams are required for a fixed virtual pivot point; (c) an actuation force causes the beams to bend, but the location of the virtual pivot point remains fixed.

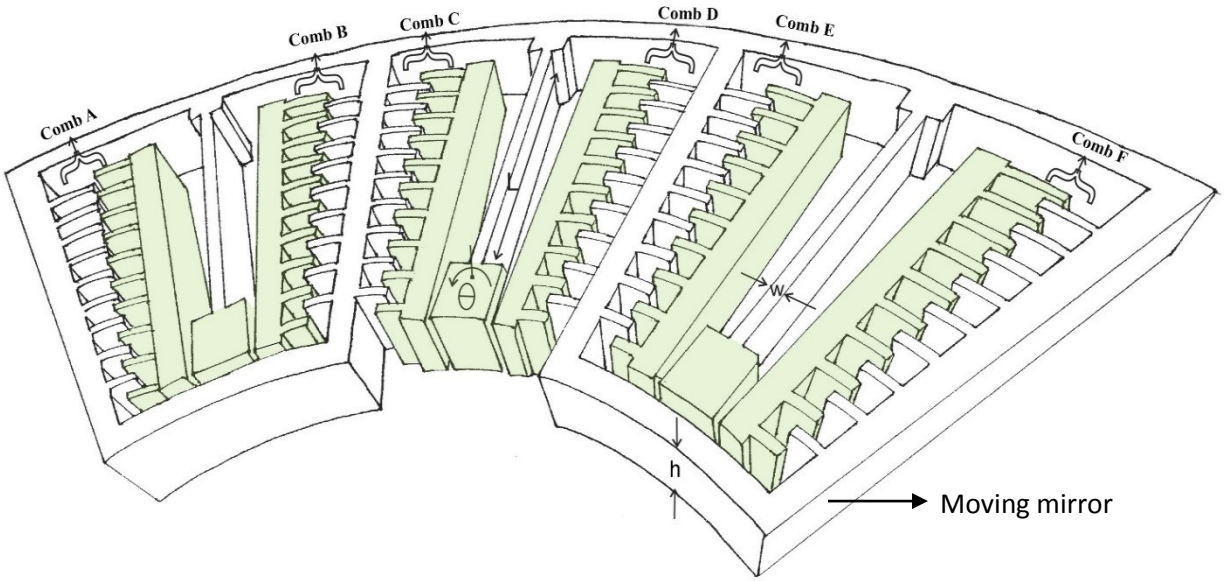

Figure 4.3 Design of a virtual pivot point rotary comb actuator. The fixed part of the structure is shaded.

The comb pairs A, C and E are used to rotate the actuator in clockwise direction and the comb pairs B, D and F are used for rotation in counter-clockwise direction. The movable arms provide long sidewalls (from 1.2 to 1.5 mm in length) that can be used as mirrors for optical applications. A clearance of 1.6 to 2.8 mm was maintained between the virtual pivot point of rotation and the movable arm structure. An iterative process of design and simulation was used to determine structural parameters which allow a maximum rotational angle of ± 1.5 degrees. Distortion of the beam flexures during angular movement results in a reduction of the radius of rotation of the movable arm (see Figure 4.4(a)). This results in touching and snapping of comb arms and fingers even at small displacements. The effect was addressed by introducing inclination angles of a few degrees from the standard radial arrangements of the comb-fingers in both fixed and movable arms [64]. A schematic diagram of the comb finger arrangement is shown in Figure 4.4(b).

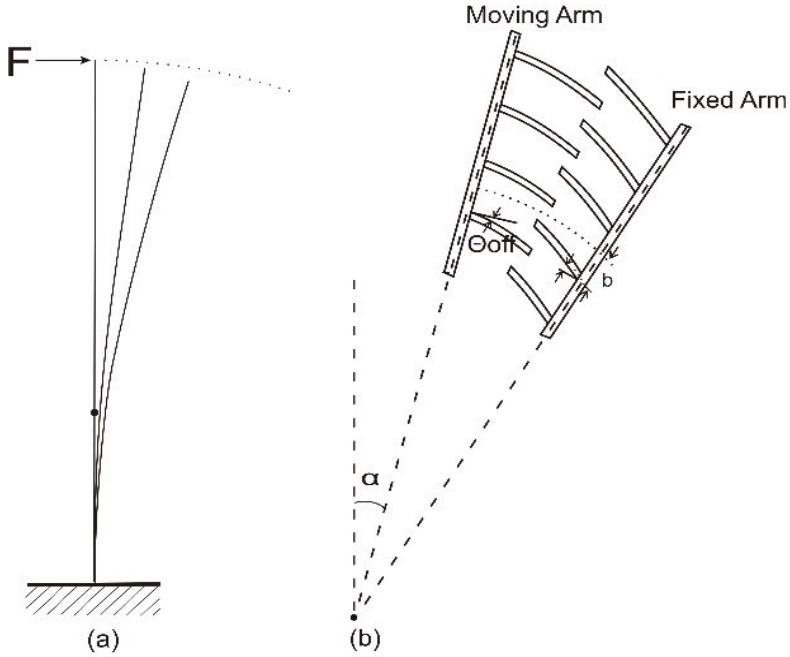

Figure 4.4 (a) Bending pattern of a cantilever beam showing the deviation from a circular path; (b) design of comb fingers with an offset angle.

In the design, I used a different inclination angle for each finger and changed the center of the finger arc accordingly to determine the locus of each comb finger. Jerman *et al.* [64] approximated the loci of the comb fingers using a varying radius as a function of rotation angle in their design. The effective location, x'_{oi}, y'_{oi}, of the center of each comb finger locus in the offset arrangement for this design is given by:

$$x'_{0i} = x_0 + \frac{R_i \sin(\theta_{off_i}) \cos(\alpha - \frac{\theta_{off_i}}{2})}{\cos(\frac{\theta_{off_i}}{2})} \qquad \textit{Equation 4.1}$$

$$y'_{0i} = y_0 - \frac{R_i \sin(\theta_{off_i}) \sin(\alpha - \frac{\theta_{off_i}}{2})}{\cos(\frac{\theta_{off_i}}{2})} \qquad \textit{Equation 4.2}$$

Here, x_0 and y_0 are the coordinates of the designed virtual pivot point, θ_{off_i} is the inclination angle of the i^{th} finger, which is zero for perpendicular arrangement of comb finger and comb-arm and negative if the finger is inclined clockwise, R_i is the radius of curvature of the i^{th} finger and α is the angle between the y-axis and the movable arm truss at no actuation. The force generated by each of the comb set of *N* rotary comb fingers can be calculated by Equation 3.1.

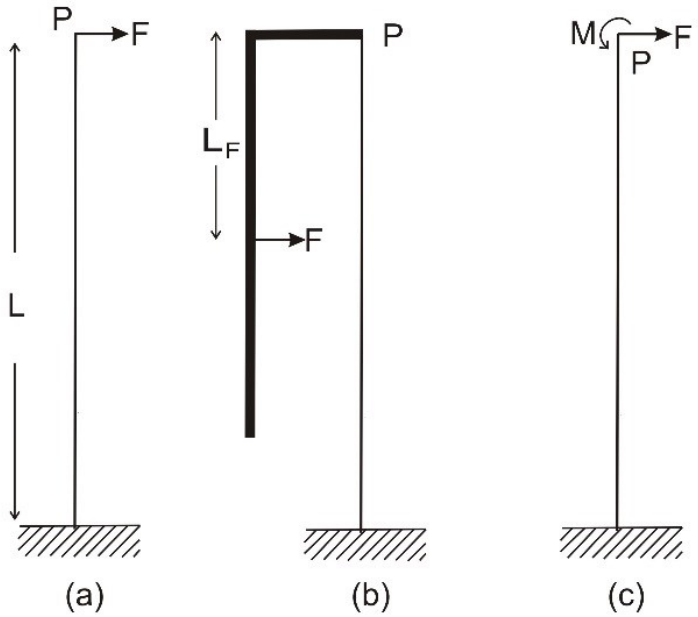

Figure 4.5 (a) A simple cantilever beam with force at the tip (point P); (b) An approximate model for the virtual pivot point structure; (c) an equivalent model for the virtual pivot structure.

Figure 4.5(a) shows a simple cantilever beam with force at its tip which is a common configuration for analysis of mechanical structure. The virtual pivot structure can be represented by an approximate model using a single beam flexure with force applied on its

folded truss which is shown in Figure 4.5(b). The effect of the force on the beam can be approximated by the equivalent structure in Figure 4.5(c), where the moment applied at the beam tip P is given as: $M=FL_F$. The moment M, due to its reverse orientation with respect to the force direction, results in a lower angular displacement of the beam tip compared to a simple cantilever beam (Figure 4.5(a)). The displacement x at the beam-tip was derived using the moment area method [54] and is expressed as:

$$x = \frac{2FL^3\left[\left(1-\frac{L_F}{L}\right)^2\left(2+\frac{L_F}{L}\right)-\left(\frac{L_F}{L}\right)^3\right]}{Ehw^3} \qquad \textit{Equation 4.3}$$

Here, L_F is the distance between the beam tip P and the point where the force is applied. Figure 4.6 shows a comparison of the calculated displacement for the approximate virtual pivot point model with simulation results for the approximate model and with simulation results for the actual device structure for a beam with length, width, and height of 1175 μm, 8.2 μm, and 50 μm, respectively. This graph was plotted using the simulated points shown by the marker in the plot and then best fitted them considering quadratic relationship between displacement and voltage as seen in Equation 4.3. The equivalent force is applied at a distance of 621 μm from the cantilever tip in the approximate model calculation. As shown in the figure, the calculated and simulated displacements for the approximate model are quite close to each other. The truss is considered to be completely rigid in the analytical calculation. The simulation results reflect this and show a somewhat smaller displacement. However, the simulated displacement for the actual device is slightly larger than both the calculated and simulated displacements for the approximate virtual pivot point model.

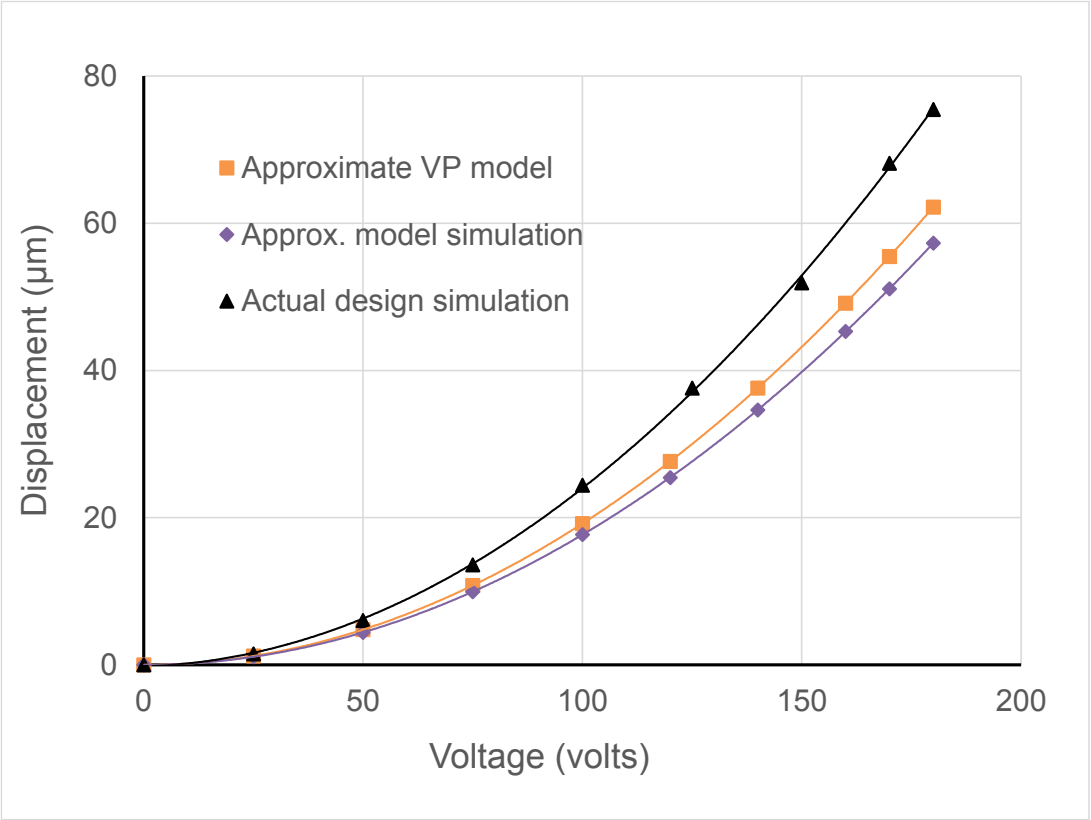

Figure 4.6 Calculated displacement of the approximate virtual pivot point model in Figure 4.5 (b) in comparison to finite element analysis simulation of this approximate model and actual device simulation

A number of factors may contribute to this larger displacement. The larger restoring truss stiffness of the actual design compared to the approximate model which has a free truss end is probably one of the major reasons. Equation 4.3 and the corresponding plot in Figure 4.6 were only used as an initial reference for our design. Device parameters were optimized using the finite element method as implemented into the finite element analysis software Intellisuite [59] for all three designs.

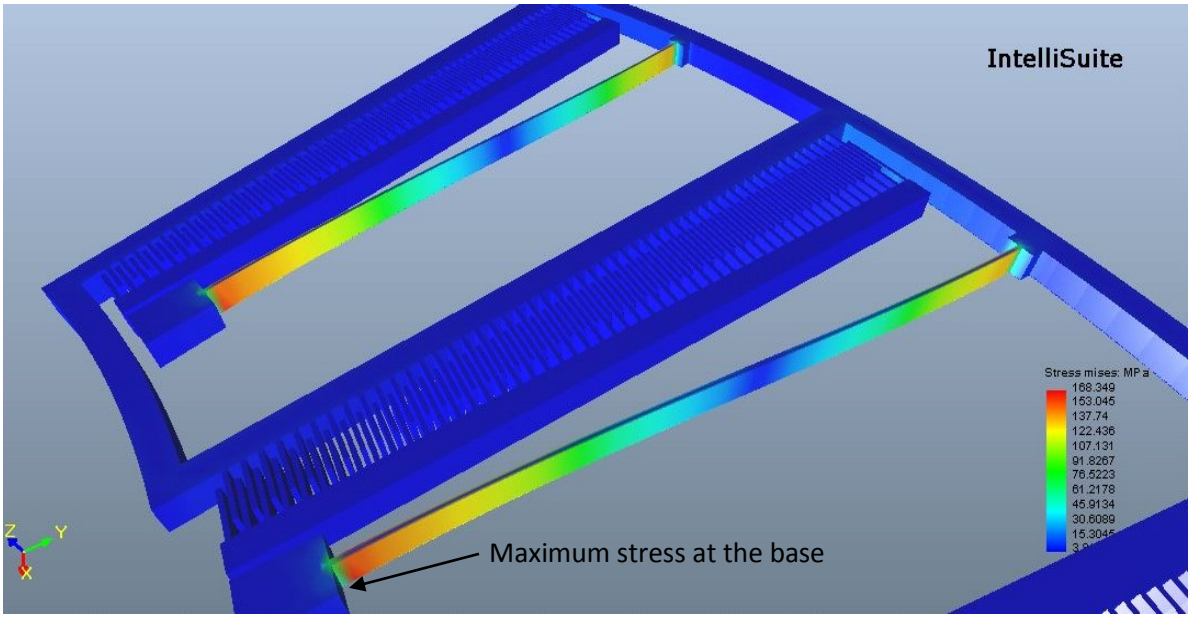

Figure 4.7 Stress distribution along the beam of the virtual pivot point MEMS actuator.

Resonance frequencies on the order of 1 kHz were found for the simulated structures. The stress distribution along the beam of the MEMS design for maximum rotation angle to one side is shown in Figure 4.7. The maximum stress (~ 160 MPa) produced in the structure for a voltage of 190 V is much lower than the yield stress (7000 MPa) of Silicon [66]. Sooriakumar *et al.* observed that stress concentration factors can go up to a value of 33 at the sharp corners of aniostropically etched Si [67]. The maximum stress generated in our design is still lower by a factor of about 2, even considering this extreme case for anisotropically etched Si. The positions of the two sidewalls of an actuator at different applied voltages were simulated and are plotted in Figure 4.8. The extrapolated positions of the movable arm sidewalls are seen to converge to a point which is distant from the device structure. This point of intersection represents the virtual pivot point of angular movement of the actuator.

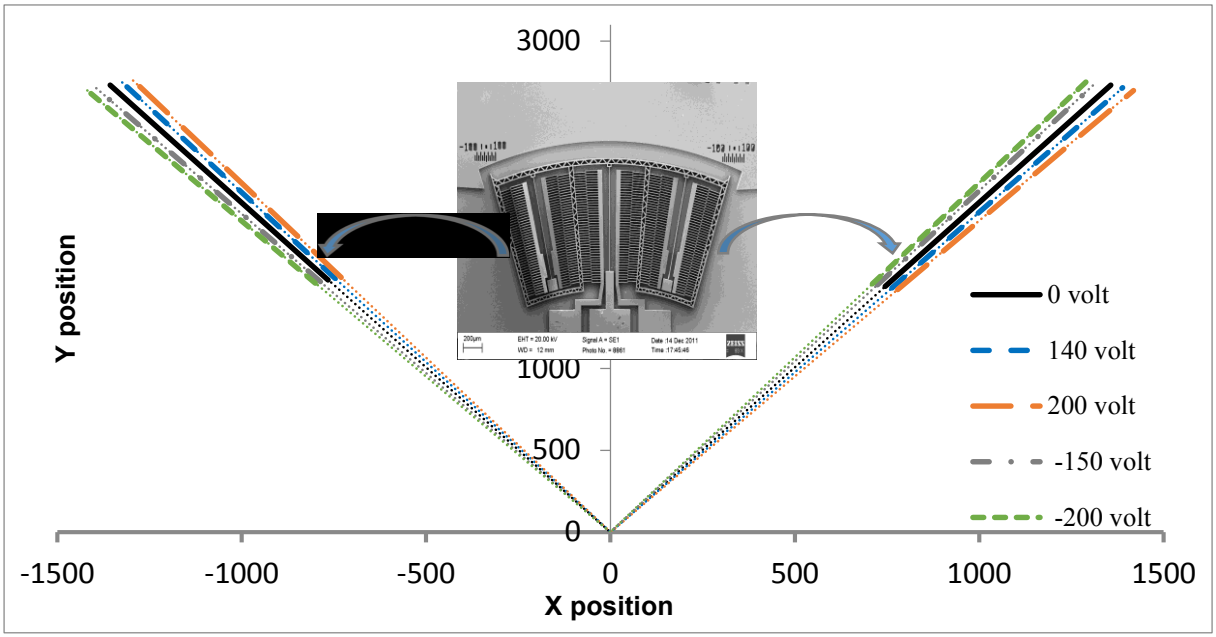

Figure 4.8 Simulations showing the position of the movable arm sidewall for different actuation voltages. Extrapolation of sidewall profiles intersect at the virtual pivot point of rotation.

Table 4-1 Design parameters for the virtual pivot point MEMS actuators.

Maximum radius from pivot point (mm)	**Beam design parameters**		**Finger design parameters**		**Device thick-ness** (μm)	**Angular inclina-tion of fingers** (degree)	**Number of fingers in each comb set**	**Clearance from virtual pivot point** (mm)
	length (μm)	width (μm)	gap (μm)	width (μm)				
3.1	1175	8.2	4.2–4.8	7.5	50	2.50–1.47	52	1.6
3.5	1175	9.0	4.2–4.8	8.0	50	2.25–1.44	50	2.0
4.0	925	5.4	4.2–4.8	5.6	50	2.25–1.70	43	2.8

4.3 Fabrication

The comb-drive actuators were designed with the parameters given in Table 4-1. Three designs with movable arm maximum tip radii of 3.1 mm, 3.5 mm, and 4 mm, respectively, were fabricated. Silicon on insulator (SOI) wafers with device layer thickness of 50 μm and buried oxide (BOX) layer of 2 μm were used. First, an oxide layer of 1.4 μm was grown using the wet oxidation method for masking in the DRIE process. The wafers were patterned through photolithography using HPR 506 photoresist. Reactive ion etching was then used to transfer the pattern onto the oxide layer. The patterned wafer was diced into individual devices using a Disco DAD 321 dicing saw. An STS inductively coupled plasma (ICP) system was used to define the pattern in the device structure. Bosch [68] process was used to anisotropically etch the silicon device layer.

A recipe was developed by carefully experimenting with different plasma parameters such as etch/passivation steps time ratio, etch and passivation gases, RF and platen power, and electromagnet control parameters of etch and passivation steps of Bosch process. Making the etch step stronger usually increases the etch rate and keeps the surface cleaner with no grass (narrow pillar like silicon structures formed at the bottom), however the profile angle goes negative and the surface roughness worsens. On the other hand, making the passivation step stronger improves the surface roughness and makes the profile angle toward 900 or positive, but decreases the etch rate and grass condition at the bottom etched surface. So optimization needs to be performed based on the requirements. A step by step example of parameter changes is shown in Section 5.2 of Chapter 5. For this device, the DRIE process was optimized to achieve a reasonable sidewall surface quality with a vertical

etch profile. A Plasmalab RIE process was run for 45 minutes after DRIE to ensure removal of the passivation polymer from the sidewall of the etched structure.

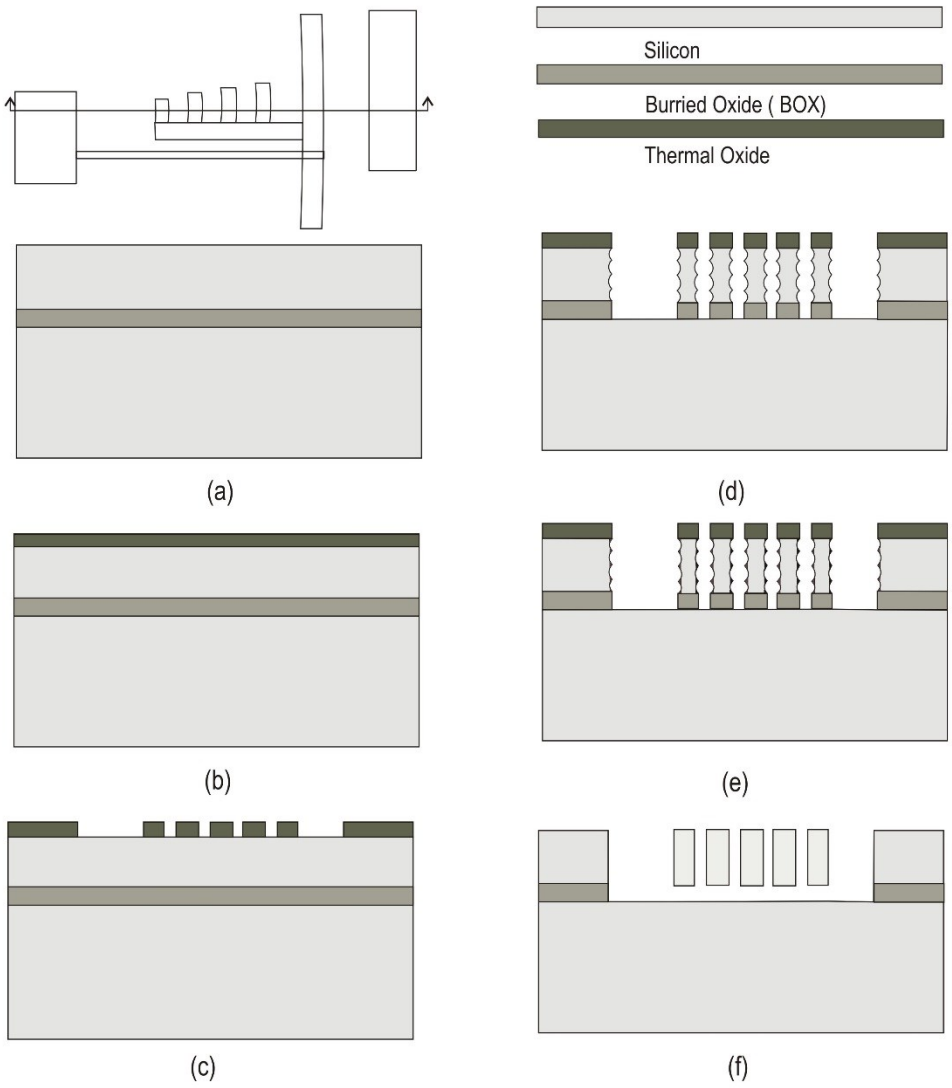

Figure 4.9 Fabrication process flow diagram: (a) SOI wafer; (b) oxidation; (c) patterning; (d) DRIE etching of device layer; (e) thermal oxidation + BOE (applied twice); (f) BOX removal, device release, and critical drying.

At this stage, a two-step thermal oxidation + BOE process, to be discussed in the next chapter, was applied to smooth the etched sidewall. Release of the movable arm was achieved by completion of sacrificial oxide etch underneath the device layer in the second BOE step of the sidewall smoothing process. Critical point drying was used to avoid stiction of movable structures during the release process. The released structures were first chromium and then gold sputtered for better electrical contact and also to improve sidewall reflectivity. The process flow diagram for the fabrication is shown in Figure 4.9. Test structures, fabricated using the same fabrication process, were cut using a dicing saw (Disco DAD 321). A LEO 1430 Scanning electron microscope (SEM) and a VEECO Dimension 3100 Atomic force microscope (AFM) were used to characterize the sidewalls of the test structures. SEM images of a fabricated VPP actuator are shown in Figure 4.10

4.4 Results and Discussion

The displacements of the movable arm tip of the fabricated structures were measured using a Wentworth wafer probing station. Two linear measurement scales with range of +/- 100 μm were carved on both sides of each device to facilitate the measurements. The displacements were measured through visual observation of the rotational movement of the arm tip and mapping it onto the inscribed scale on the device by drawing an imaginary parallel line from the scale. The specific arrangement of scale and moveable arm leads to some parallax error in the experimental data. However, an optical microscope (8X optical magnification) connected to a computer through a camcorder (3X zoom) was used for the measurements, and the parallax error should not exceed one-third of a measurement bar (20 μm) and is estimated to be a maximum of about ±6 μm.

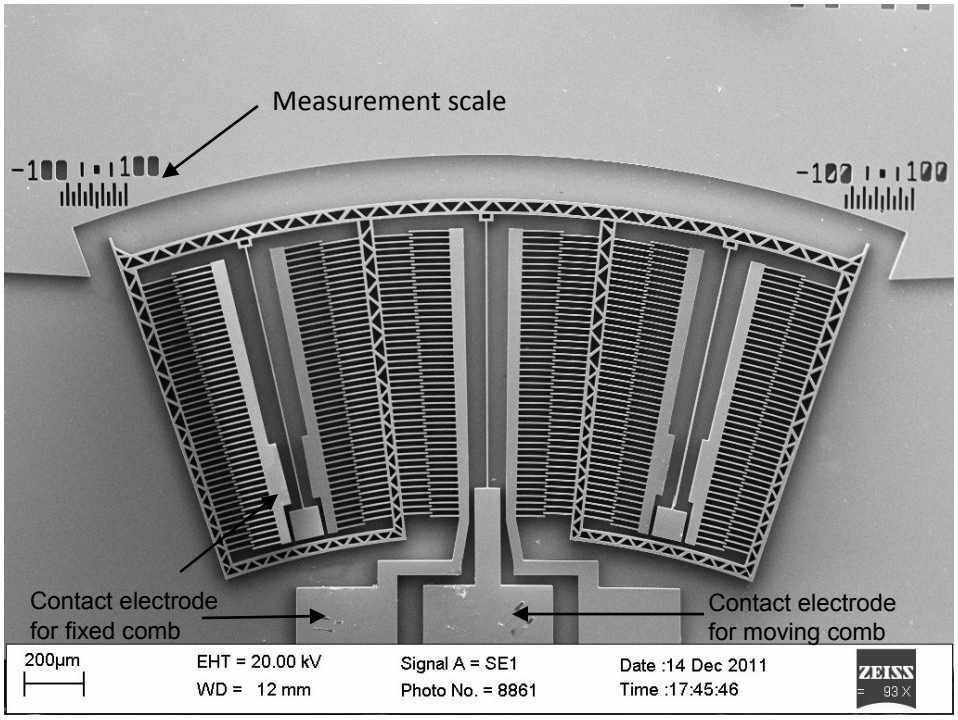

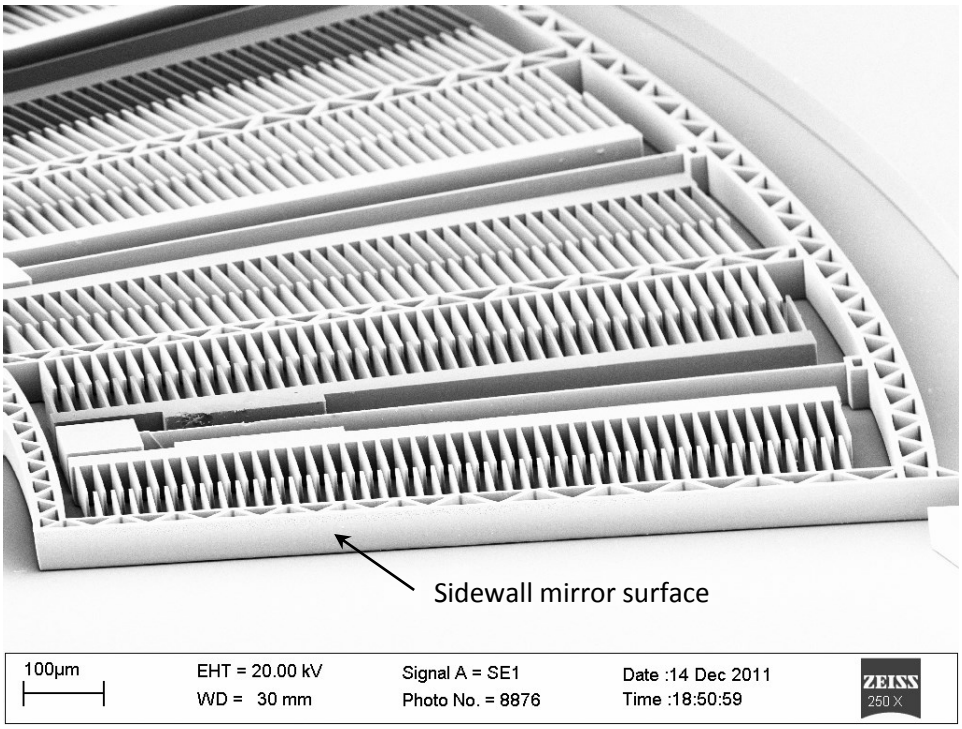

Figure 4.10 SEM images of a fabricated virtual pivot point rotary actuator.

Tip displacements against the actuation voltage for two designs are shown in Figure 4.11, together with the error bars. There is good agreement between the experimental results and the values obtained from the simulations. Symmetrical displacements in clockwise and counter-clockwise directions were achieved. The largest displacement (≈77 μm) for the 3.1 mm design corresponds to an angular deflection of 1.5 degrees.

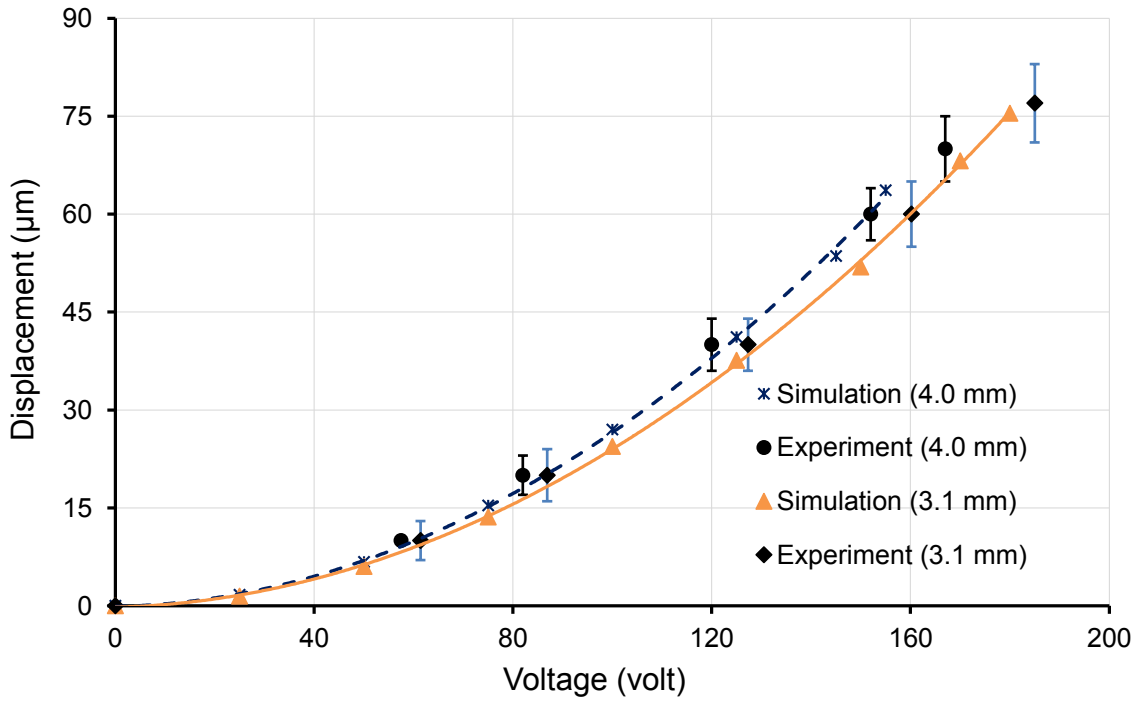

Figure 4.11 Experimental and simulated tip displacements as a function of actuation voltage.

The measured displacements for the 4 mm design show slight over-actuation compared to the simulated values. This effect can be attributed to beam width narrowing due to notching effects during the DRIE process. This is in agreement with Equation 4.3, where a cubic

relation of displacement against beam width was observed. The sidewalls of the movable arm structure are accessible for optical applications and the surfaces have near optical quality as shown in Figure 4.10. The smoothed sidewall surface was tested optically by shooting visible light on to the surface. The schematic diagram of the experimental setup is shown in Figure 4.12(a).

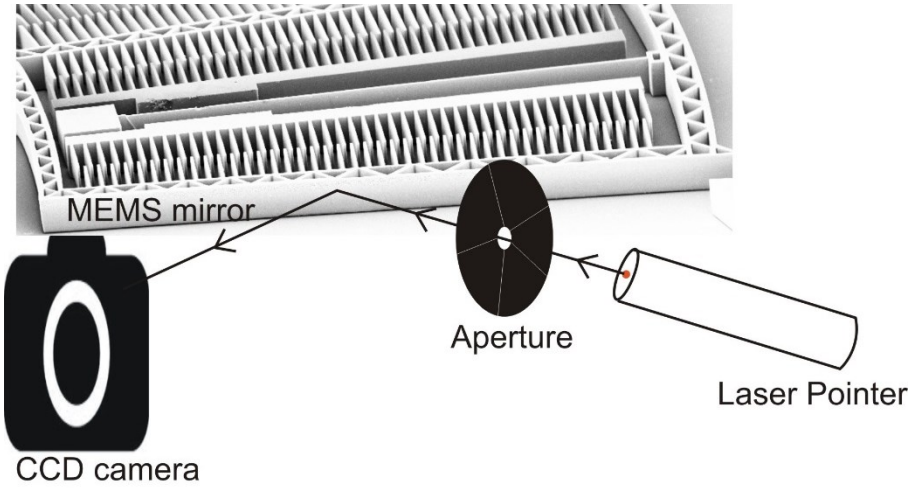

(a) Schematic diagram of the experimental setup.

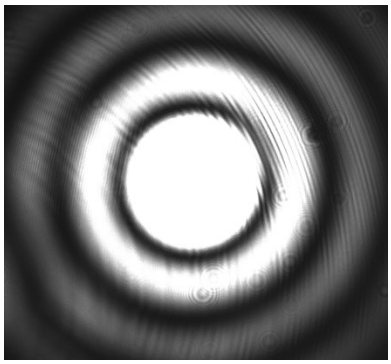

(b) Original beam captured at a distance of 4 cm from the aperture.

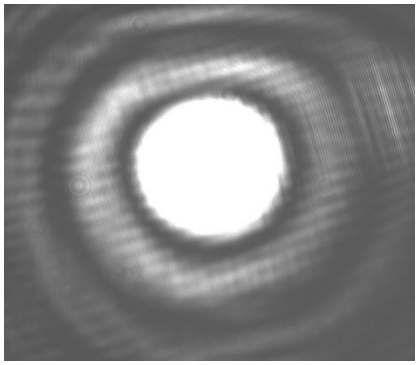

(c) Reflected beam from the smoothed surface.

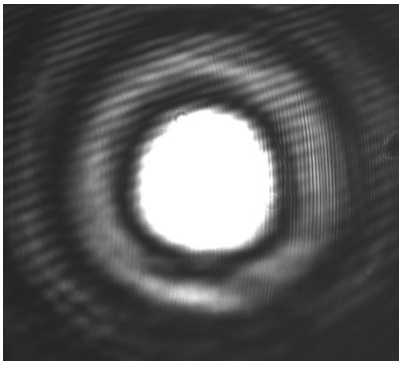

(d) Reflected beam from the standard etched surface.

Figure 4.12 Optical testing of sidewall mirror surface; (a) schematic; (b)-(d) captured CCD images.

A beam of a laser pointer (maximum output < 4 mw, 630-680 nm) was aligned through a 50 μm circular aperture onto the sidewall surface of both the smoothed and the standard etched surface. The beam spot size on the aperture was around 4 mm x 2.5mm, which was 1.2 mm distant from the laser. The reflected light was captured with a CCD camera (Pointgrey Chameleon, 1.3 MP, 4.8 mm x 3.6 mm). The distance between the aperture and the mirror surface was between 6–7 mm and the distance between the CCD camera and the mirror surface was approximately 3.5 cm. Figure 4.12(b) shows an image of un-reflected light beam at a distance of around 4 cm from the aperture. Diffraction effects due to the aperture are clearly visible. The diameter of the central circle in Figure 4.12 (b) is around 1.3 mm. The light beam reflected from the smoothed surface, obtained using the 2-step oxidation + BOE procedure, and a standard etched surface was also captured with the CCD camera. The resulting images of the light beams are shown in Figure 4.12 (c) and (d) respectively. Both mirrors have a height of about 100 μm. The secondary diffraction patterns seen on the images shows surface scallops and are less pronounced in the case of the smoothed surface.

To measure the intensity of the reflected light, I replaced the CCD camera with a photodetector (Alphalas, UPD-500-SP, 0.5 mm^2) and kept the experimental dimensions the same. The measured intensity of the light reflected from the smoothed mirror surface is about 56.3% of that of the original light beam, whereas that from the standard etched surface is about 20.3% of the original light beam. Similar measurements were done with a fabricated VPP actuator, which has a mirror thickness of 50 μm. The distance between the aperture and the accessible movable mirror of the actuator was 1.2 cm and the distance between the CCD camera and the mirror surface was approximately 4 cm in this experiment. Only a portion of

the original light beam reflected from the 50 μm wide mirror because of the diverging nature of the beam after the aperture. With the 50 μm mirror, the measured intensity corresponding to the detected light reflected from the smoothed surface is about 1% of that of the original light beam whereas that from the standard etched surface is about 0.25% of the original light beam. With the smoothing process, the actuator mirror surface roughness has thus improved significantly that causes less scattering of light from the surface, resulting in higher intensity.

4.5 Summary

In this chapter, I presented the design and fabrication of virtual pivot point comb-drive actuators with a maximum deflection range of up to ±1.5 degrees. The total angular deflection of 3 degrees is sufficient for tuning wavelength range of more than 100 nm. Movable arm-tip radii of 4 mm and clearances of up to 2.8 mm from the virtual pivotal point to the device structure were achieved, which provides enough workable space for placing collimating lens. These actuators can be used, for example, to provide mirror rotation in miniaturized external cavity lasers in Littman configuration and also in other systems with space constraints for optical path alignment. The sidewalls of the movable arms of the actuator structures are accessible for on-chip optical applications. Sidewall smoothing techniques were developed to significantly reduce the surface roughness. This will be discussed in detail in the next chapter.

5 Sidewall Smoothing of Etched Silicon[3]

5.1 Introduction

The advances in micro and nano fabrication technologies make it feasible to use silicon as material for micro-optical components. MEMS devices with optical functionality are now very common. While many of the MOEMS applications use the top shiny smooth surface of the silicon wafer for optical reflection, research efforts have been progressed to fabricate micro-etched optical components which offer extra advantages such as easier packaging and better integration with other components.

[3] This chapter is prepared based on the conference proceeding (I) and sidewall smoothing section of the following articles (II* and III):

I. T. M. F. Amin , M. Q. Huda, J. Tulip, and W. Jäger, "Sidewall roughness control in deep reactive ion etch process for micromachined Si devices", 7th ICECE, 82-85 (2012).
II. M. Q. Huda, T. M. F. Amin, Y. Ning, G. McKinnon, J. Tulip, and W. Jäger, "Rotary MEMS comb-drive actuator with smooth sidewall for photonic applications," Journal of Micro/Nanolithography, MEMS, and MOEMS, 11, 023012 (2012).
*Note: In addition of the design of the actuator, sidewall smoothing section of this articles is my contribution in this article.
III. T. M. F. Amin, M. Q. Huda, J. Tulip, and W. Jäger, "A virtual pivot point MEMS actuator with optical quality sidewall," Journal of Micromechanics and Micro-engineering (2014), under review.

Especially in ECLs, it needs vertical mirror with good surface quality to avoid unnecessary scattering of light. However, a significant challenge in the use of micro-etched structures for optical applications is the quality of the sidewall, mainly in terms of its surface roughness. According to Marechal's criterion, the rms roughness of the surface should be below λ/14 to avoid significant light scattering [69] (λ is the wavelength of the light).

Control over sidewall smoothness has been extensively investigated by many researchers and a wide range of wet etching or dry etching techniques have been proposed for the fabrication of Si microstructures. Chemical wet etching techniques, such as using KOH solution after DRIE for (110) Si or KOH + IPA (iso propyle alcohol) on a (100) Si wafer [70, 71], have been used to fabricate smooth sidewall structures with good optical characteristics. However, these processes become less practical for MEMS structures with high aspect ratio. Another major drawback of wet etching is the strong dependence on crystal orientation and the stringent requirement of alignment along the crystal orientation. On the other hand, dry etching techniques have no dependence on crystal orientation and may be more flexible for designing and fabricating micro-optical components. A variety of high density plasma etching systems, such as electron cyclotron resonance (ECR), helical resonator, and inductively coupled plasma (ICP), are available for advanced dry etching. Control of sidewall smoothness can be achieved by varying the plasma process parameters of advanced Si etch techniques, as reported by Lärmer and Schilp [68]. Sidewalls with rms roughness as low as 8 nm were achieved by other researchers using this advanced Si etching technique [72, 73]. There are also efforts to develop techniques to smooth the etched sidewall after the DRIE process. A technique using focused ion beam milling after deep etch has been described in [74] to achieve an rms roughness of ~2 nm. The complexity of precise alignment of the

sidewall in the direction of the ion beam, poor selectivity over mask, and the difficulty of focusing the beam on multiple devices are some of the drawbacks of this method. Good quality sidewall surfaces were also produced through silicon surface reflow, at high temperature, in low pressure hydrogen ambient [75]. This process is also difficult to apply to MEMS actuators since the surface reflow would deform the high aspect ratio elements of the structure, e.g., the supporting beam and the comb fingers. The use of thermal oxidation or boron diffusion was also reported to reduce the sidewall roughness [57, 76]. However, none of the processes was tested to smooth deeply etched micro structures.

In this chapter, I present the development of two different sidewall smoothing methods for micro-etched silicon devices. In describing the first method, I give a systematic and detailed study of etch/passivation effects on the DRIE etched sidewalls and report a slightly over-passivated DRIE cycle for the production of smooth sidewalls. In the second case, a two-step oxidation plus BOE process is presented to smooth the scalloped sidewall of the actuator arm. Both of these methods have been applied to fabricate optical quality smooth sidewalls of MEMS actuators.

5.2 Over-Passivated Bosch Process

A systematic approach was taken in developing the over-passivated Bosch process to obtain a smooth sidewall. Etching parameters, such as ICP power, etch/passivation time ratio, platen power, gas flows, EM delay etc., were carefully varied and their effects were monitored step by step towards achieving an optimized recipe. Etching non-uniformity, profile

angle, and loading effects were addressed during the development of the recipe. The idea of the process is to cover the scallops using the polymer from the passivation step of the Bosch process.

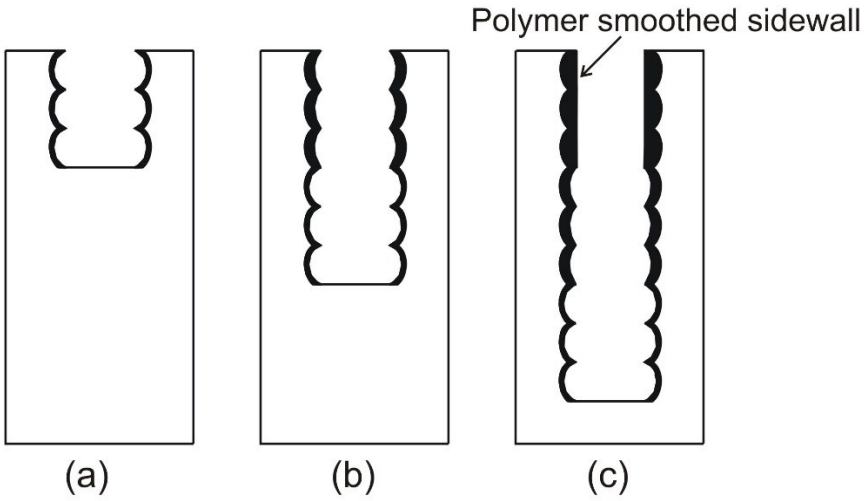

Figure 5.1 Basic concept of the sidewall smoothing process.

The Bosch DRIE process usually starts with a passivation cycle using C_4F_8 followed by an etch cycle typically involving SF_6 and O_2. The passivation cycle introduces sacrificial polymer that protects the sidewall. The polymer at the bottom of the feature is removed completely in the etch cycle while the polymer on the sidewall remains to some extent due to the directional etching. The balance between etch and passivation cycles therefore determines the surface morphology of the sidewall. In our developed recipe, the passivation polymer was used in a controlled way to gradually cover the inherent scallops of the sidewall. Figure 5.1 shows the basic idea of the over-passivated smoothing process. The first figure from the left shows a usual etched sidewall produced with the Bosch process. The next figure shows a

slightly over-passivated sidewall which begins to smooth at the top portion as etch progresses in the bottom. The final figure shows a completely smoothed sidewall at the top as the smoothing process propagates to the bottom. Etching continues until a maximum depth is reached, after which problems occur, as described below.

5.2.1 Experiment

The quality of the mask is very important for the DRIE process. A soft mask, such as photoresist, usually has defects that can propagate through the structure unless special type of resist is used. Hard masks are thus preferred for etching deep micro structures. A thermally grown oxide layer of 1.8 μm thickness was used to ensure high mask quality.Test structures were first patterned using photolithography. Samples for DRIE were then prepared by RIE of the oxide layer using photoresist (HPR 506) as mask. The test structures consisted of a series of different features with sizes ranging from 5 μm to hundreds of μm. The structures were then deep etched using a modified Bosch recipe as discussed in the following section in a STS ICP RIE chamber. After DRIE, the devices were cut using a dicing saw (Disco DAD 321) along the etched area of larger features (≈ 100 μm or greater). A thin layer of chromium (~15 nm) followed by gold (~50 nm) was then deposited on some of the samples using a sputtering process. Finally the quality of the sidewalls was characterized using a LEO 1430 scanning electron Microscope (SEM) and a Veeco Dimension 3100 atomic force microscope (AFM). SEM image provides an overall view and single point measurement of surface profile. On the other hand, AFM measurement provides a more detailed two dimensional measurement of a tiny (5 μm x 5 μm) surface area.

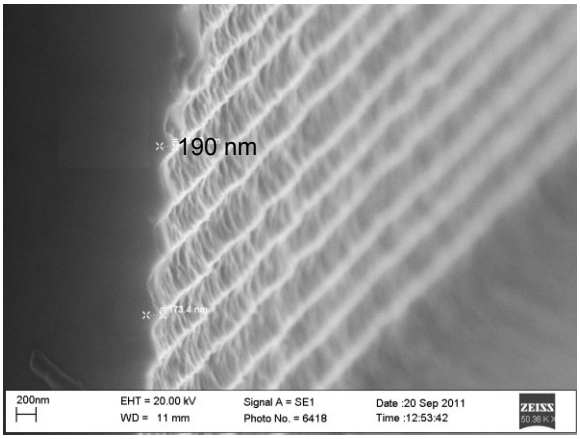

(a)

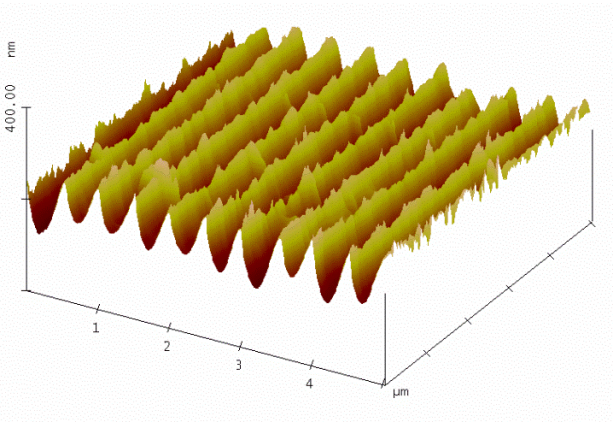

(b)

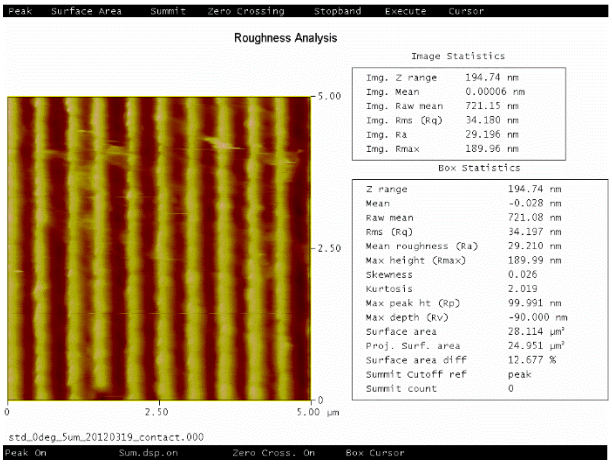

(c)

Figure 5.2 Images of a standard etched sidewall specimen: (a) SEM image; (b) AFM 3D sidewall image; (c) AFM Surface roughness measurement.

5.2.2 Results and Discussion

A sidewall profile from a standard Bosch process with typical etch/passivation cycle parameters is shown in Figure 5.2. The maximum peak-to-valley height of the sidewall scallops was determined to be around 190 nm from the SEM image. A more detailed surface profile is shown in Figure 5.2 (b) and (c) from a two-dimensional scan by AFM. A common

measure of the smoothness of a surface profile is its rms roughness. From an AFM image, the rms roughness is calculated by first determining a mean data plane, whose z-value is the arithmetic average of all z-values within the enclosed area, and then calculating the root mean square average of the height deviations with respect to the mean data plane. The measured rms roughness from the 2-dimensional AFM image for the surface is 34 nm. A significant improvement in scallop roughness was achieved by decreasing the etch/passivation cycle time ratio as seen in Figure 5.3(a)-(c). In this case, the maximum scallop peak to valley height was found to be around 110 nm from an SEM image and the rms roughness was reduced to 19.6 nm (Figure 5.3(c)), as measured by AFM. A reduction of the SF_6 gas flow compared to the previous step weakened the strength of etching cycle and a further reduction of scallop roughness was observed. The peak to valley sidewall height reduced to 81 nm for this recipe. The sidewall profiles shown in Figure 5.3 (d)-(f) correspond to an rms roughness of about 12 nm with reduction in scallop size.

A slight over-passivation was achieved in the next sample shown in Figure 5.4 by further reducing etch/passivation cycle time ratio. A remarkable difference was achieved by the controlled over-passivation. The polymer formed by the passivation cycle covered the scallops through a surface reflow process and thus resulted in a smooth sidewall. The rms surface roughness improved by a factor of 2 with a measured value of 5.2 nm. A further improvement in sidewall surface roughness and etch profile was achieved for the sample in Figure 5.5 with reduction of the etch cycle power. The platen electrode power and electromagnet settings were adjusted to avoid growing grass at the bottom of the trench.

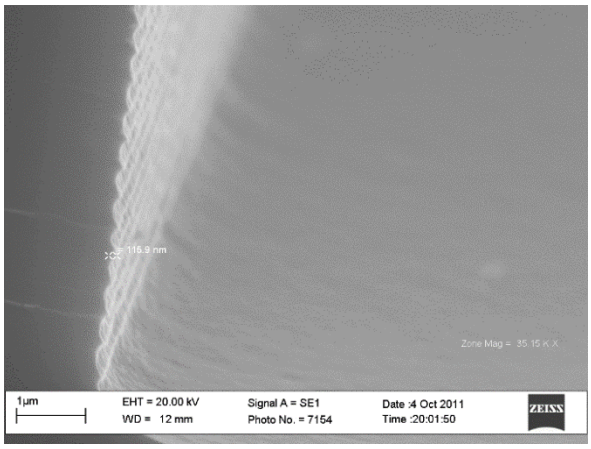

(a)

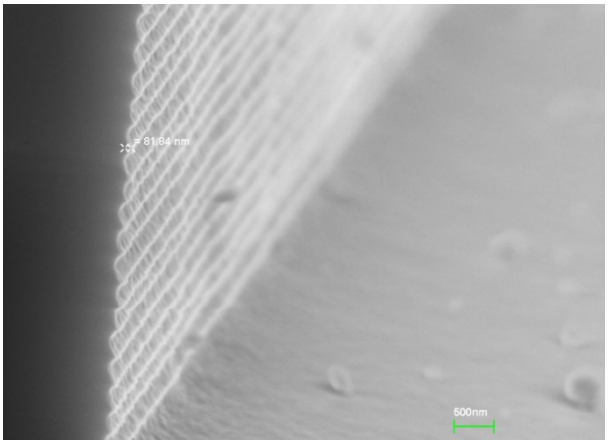

(d)

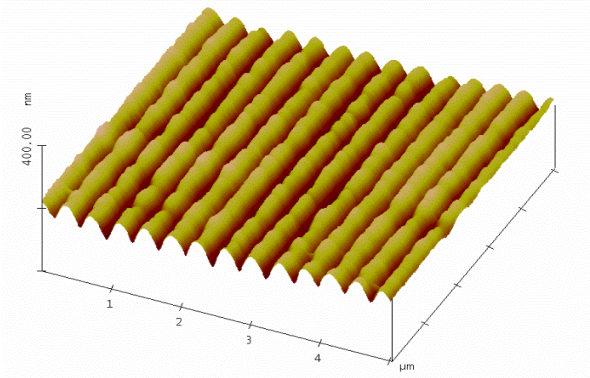

(b)

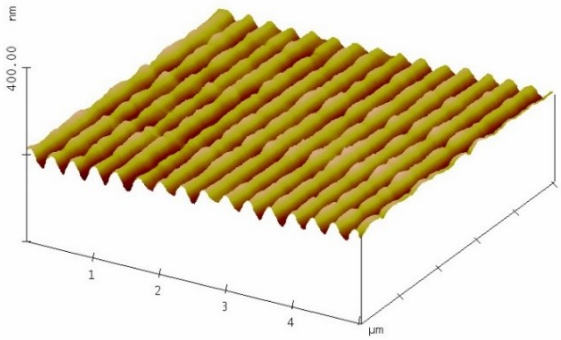

(e)

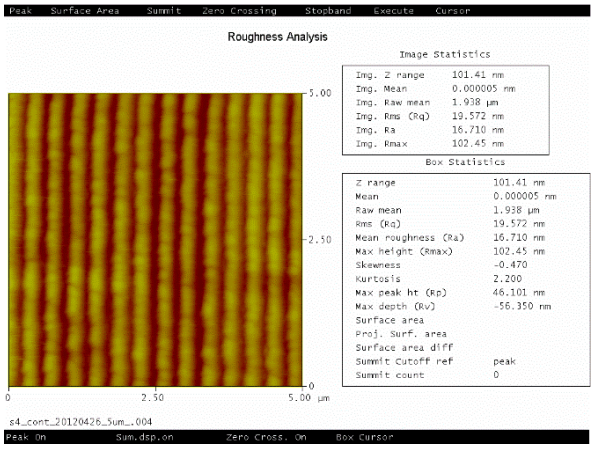

(c)

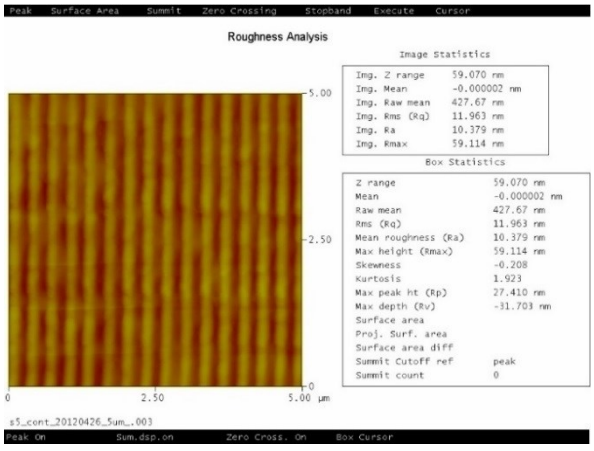

(f)

Figure 5.3 Images of the etched sidewall using two intermediate recipes: after changing the etch/passivation cycle time- (a) SEM image; (b) AFM sidewall image; (c) surface roughness (AFM); and after changing the etch gas flow- (d) SEM image; (e) AFM sidewall image; (f) surface roughness (AFM).

Eventually, the formation of a smooth vertical wall of up to a maximum trench depth of 120 μm was achieved with the over-passivated recipe as shown in Figure 5.5 (a)-(f). The vertical profile of the structure is at an angle near 89°. Figure 5.5(e) shows an AFM image of the sidewall profile of the structure. The rms roughness resulting from the final developed recipe was found to be 4.8 nm (Figure 5.5(f)).

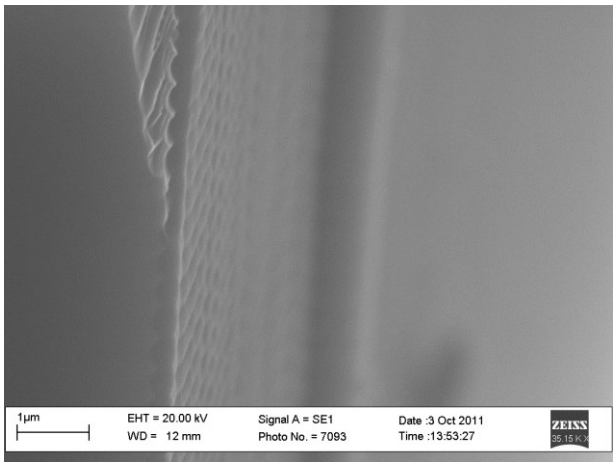

(a)

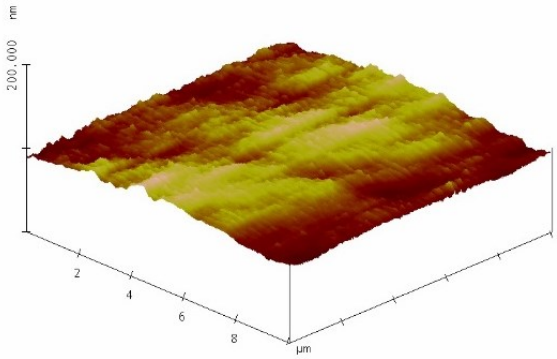

(b)

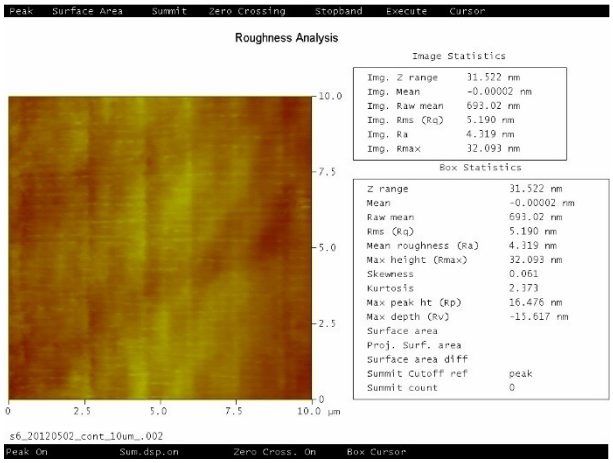

(c)

Figure 5.4 Images of an etched sidewall after further adjustment of the etch/passivation cycle time: (a) SEM image; (b) AFM 3D sidewall profile; (c) AFM surface roughness measurement.

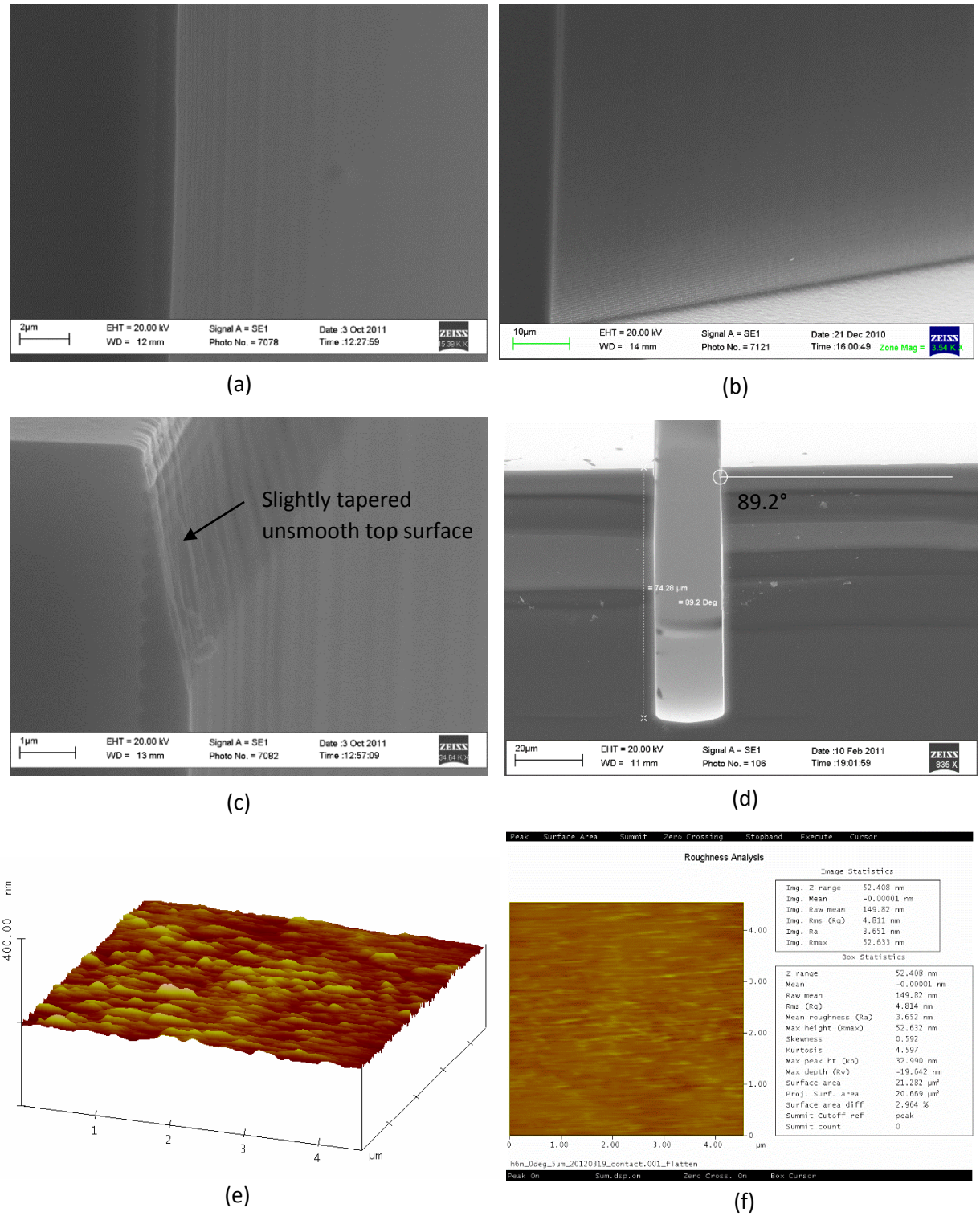

Figure 5.5 Images of the etched sidewall for the controlled over-passivated recipe: (a) SEM image of polymer covered smooth sidewall; (b) SEM image at the bottom; (c) slightly tapered profile on top edge (d) profile angle; (e) 3D sidewall image (AFM); (f) sidewall surface roughness (AFM)

The roughness of the sidewalls was furthered improved by the metallization process. Thin layers of chromium and gold were deposited on the sidewall using a sputtering process to increase reflectivity. The final rms roughness of the sidewall after metallization of the features was 3.9 nm (Figure 5.6(b)). Details of the initial, intermediate and final etch process parameters are summarized in Table 5-1.

Table 5-1 Process parameters for initial and final developed recipe.

Process	**Step**	**Gas Flow (sccm)**			**Cycle Time**	**RF Power**	**Platen Power**	**EM Delay**
		SF_6	O_2	C_4F_8	(sec)	(watt)	(watt)	(sec)
Initial	Passivation	0	0	200	1.3	1000	0	0
(Figure 5.2)	Etch	350	35	0	4	3000	50	2
Intermediate	Passivation	0	0	200	1.3	1000	0	0
(Figure 5.3 a-c)	Etch	350	35	0	3	3000	50	2
Intermediate	Passivation	0	0	200	1.3	1000	0	0
(Figure 5.3 d-f)	Etch	300	35	0	3	3000	50	3
Intermediate	Passivation	0	0	200	2	1000	0	0
(Figure 5.4)	Etch	300	35	0	4	3000	45	3
Final	Passivation	0	0	180	2	1000	0	0
(Figure 5.5)	Etch	300	35	0	4	2500	45	4

The controlled over-passivated sidewall smoothing technique was then applied for fabrication of rotary comb actuators discussed in Chapter 3. Figure 5.6(c)-(d) show the smooth sidewall of the moving arm of the fabricated rotary comb actuators [61] for photonic applications. There is some roughness observed in the first few μm of the top and bottom portions of the structures smoothed by the over-passivated recipe, as shown in Figure 5.5 (b)-(c).

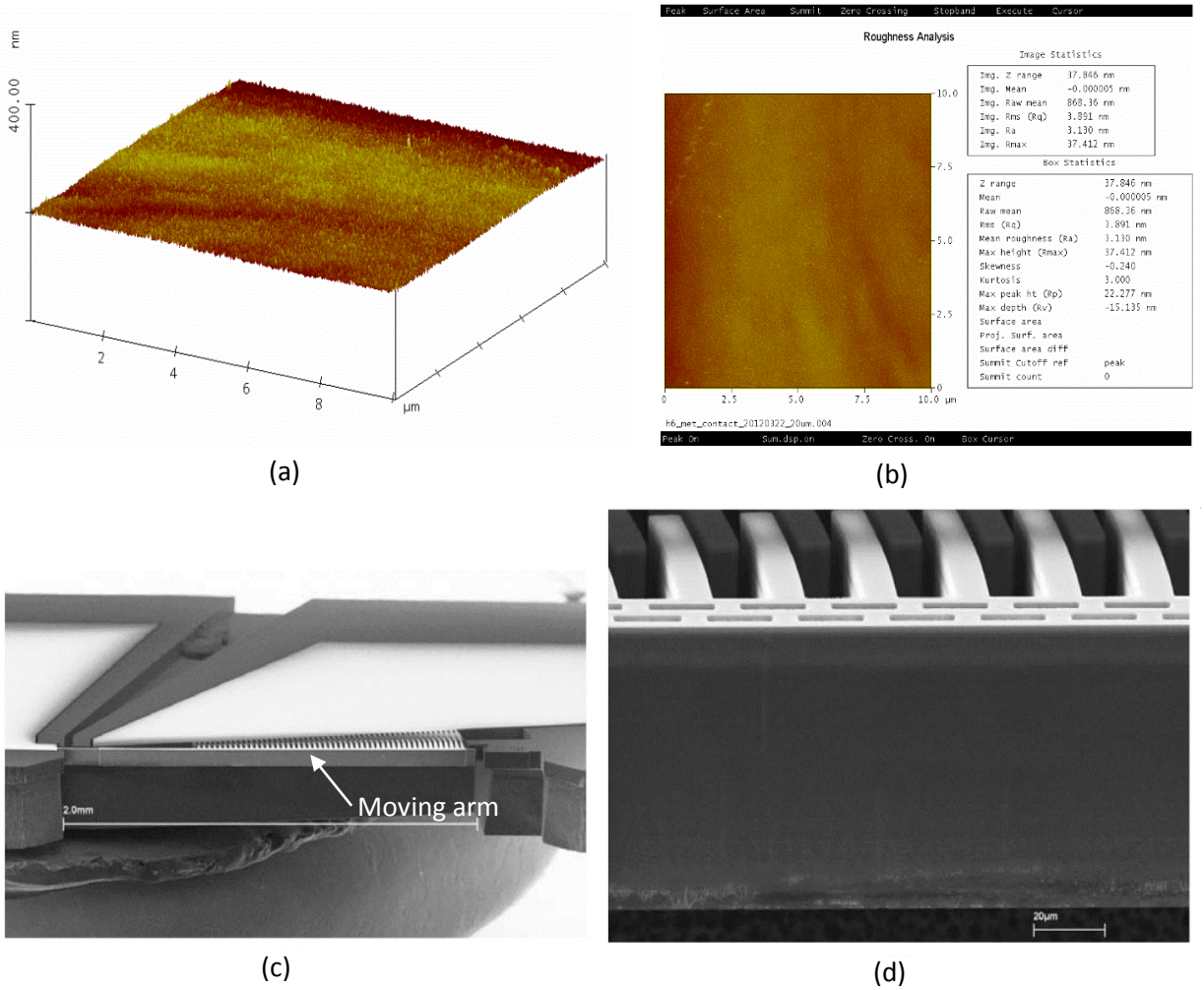

Figure 5.6 Images of the etched sidewall using a controlled over-passivated recipe after metallization: (a) AFM image 3D sidewall; (b) surface roughness profile (AFM); (c) SEM image of a fabricated rotary comb actuator using the over-passivated recipe; (d) enlarged view of smooth sidewall of the moving arm.

The roughness in the bottom portion is expected as this is the freshly etched section which is yet to be smoothed by the polymer. The roughness in the top portion can be explained by the etching of the polymer through unidirectional ions and radicals. The maximum achievable smooth sidewall using the developed controlled over-passivation method is around ~120 μm. Vertical striation in the sidewall becomes prominent with further increase of the profile depth. Figure 5.7 shows a picture of severely vertically striped sidewall for a trench deeper than 150 μm. Pike et al. [77] analyzed the vertical striation of an over-passivated sidewall. According to their study, charging of the polymer film disrupts the ion flux during the etch step of Bosch DRIE process. The build-up of polymer can reach to a critical level at which charging is unstable with respect to lateral uniformity of the process and vertical striation starts to form in the sidewall.

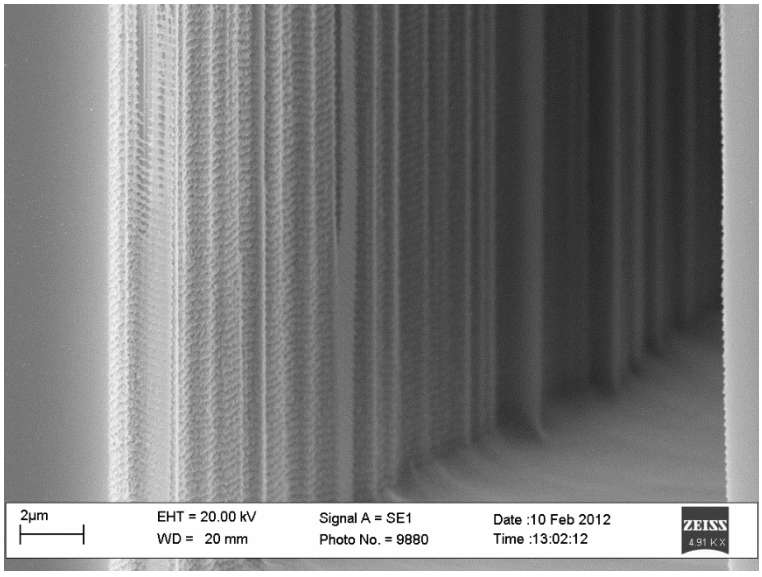

Figure 5.7 Vertical striation of sidewall after an etching depth of 150 μm with the DRIE process.

5.3 Two Steps Oxidation + BOE Sidewall Smoothing Method

A second method for smoothing of a silicon sidewall after the DRIE process was developed by performing oxidation of silicon and then removal of the oxide. This method is particularly useful for applications that require wet chemical processing after the deep etching step. The controlled over-passivated process, discussed in the previous section, puts a limitation on device processing, that is, it does not allow a wet chemical process that can attack the polymer on the sidewall. However, wet chemical processing such as piranha cleaning, MEMS device release using BOE, etc. can be a necessary step in many instances and the method described below provides an excellent solution for those cases.

Thermal oxidation of silicon is well described by the Deal-Grove model [78]. The thickness of the oxide layer after dry or wet oxidation can be perfectly calculated by this model for a planar surface. However, this model is not useful to determine the growth of the oxide layer on curved surfaces. It has been experimentally demonstrated that the oxidation rate of curved silicon surfaces is retarded compared to that of planar surfaces [79-81]. Kay *et al.* [81] modeled the oxidation of curved surfaces and proposed that the stress from the two-dimensional oxide deformation affects the kinetic parameters in the Deal-Grove model. In particular, the viscous stress associated with the non-uniform deformation of the oxide is identified as the fundamental force of retardation of oxidation which reduces the surface reaction rate on curved surfaces. A convex surface oxidizes faster than a planar surface because of a greater supply of oxidants. In addition, the tensile pressure in a convex structure enhances oxidant transport and oxide flow, as opposed to a concave structure,

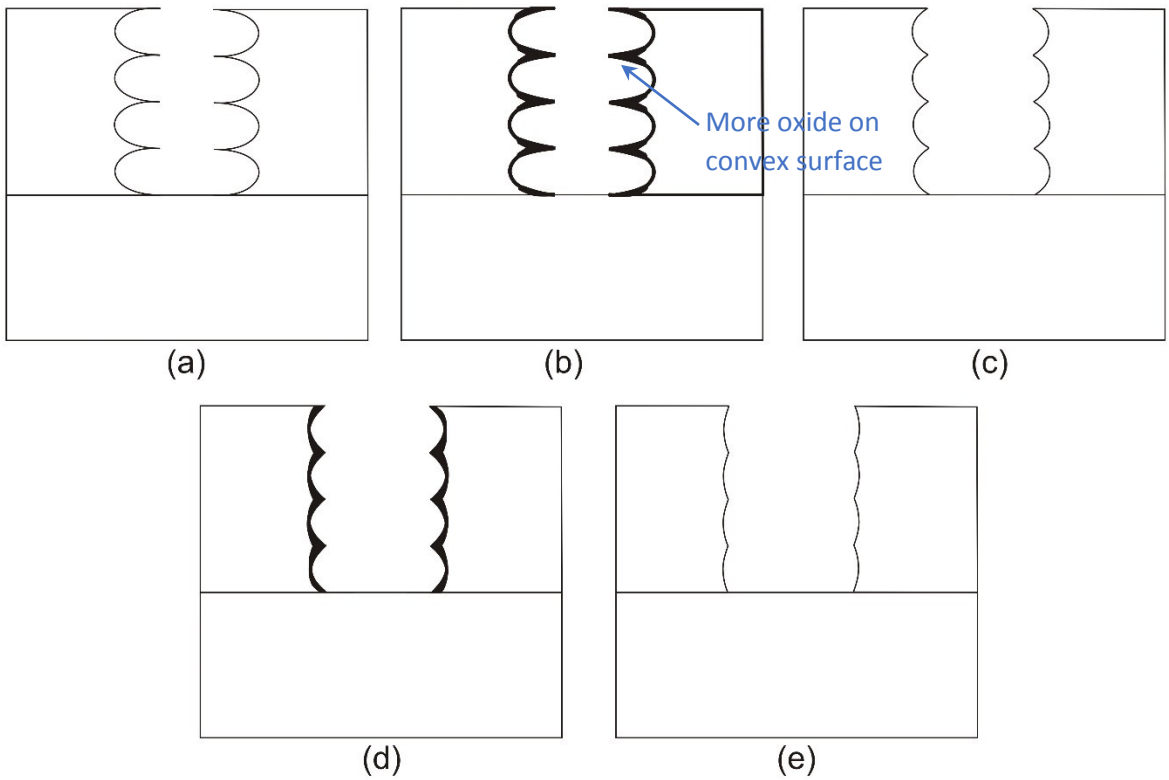

Figure 5.8 The detailed concept of the sidewall smoothing process using oxidation + BOE technique: (a) Etched Si sidewall; (b) oxidized sidewall (convex surface is oxidized more than concave surface); (c) sidewall after removing oxide using BOE; (d) oxidation of sidewall (2nd time) and; (e) smooth sidewall after oxide removal using BOE.

where compressive pressure makes oxidant transport and flow more difficult. These special characteristics of oxidation of curved surfaces can be used to smooth the deeply etched and scalloped sidewalls from a DRIE process. Ripples along Si sidewalls contain both concave and convex surfaces. The different oxidation rates of convex versus concave surfaces result in smoother sidewall morphology after the SiO_2 is removed. The process is schematically described in Figure 5.8.

5.3.1 Experiment

An STS ICP RIE system was used to etch the silicon structures. The Standard Bosch DRIE recipe provided by the manufacturer produced highly scalloped sidewalls, and the rms roughness was found around 34.197 nm, as seen from AFM Figure 5.2. To improve the surface quality and the structure profile, I modified the Bosch process by optimizing plasma process parameters such as etch/passivation cycle time, gas flow, ICP coil power, chamber pressure etc. Silicon structures of varying thicknesses were anisotropically etched in a silicon substrate, down to a maximum depth of 100 μm using the optimized recipe. The structures then underwent an oxygen plasma ash process and piranha cleaning to remove any residual polymer on the sidewall as thermal oxidation requires a clean surface. The samples were put into a 3-zone oxidation tube furnace on a carrier wafer. Wet oxidation of the samples was performed for 3 hours at a temperature of 1050 °C. The relatively high temperature was chosen as the smoothing process is more effective at higher temperature [57].

The temperature dependence of sidewall smoothness during oxidation process can be related to the temperature dependent viscous stress for two dimensional oxide growth [80]. At low oxidation temperature, the retardation of oxide growth is more severe. At higher oxidation temperatures, oxide viscosity is reduced, oxide starts to flow and stress becomes lower. This results in a higher oxidation rate and also smoother Si–SiO_2 interface. After the first oxidation step, one-third of the samples was kept separated for longer oxidation, and the rest of the samples was wet etched in BOE solution for 40 minutes to remove the grown oxide from sample surfaces. Another cycle of oxidation + BOE was then performed on the samples that were reserved after the first oxidation as well as on half of the samples with removed oxide layer from first cycle.

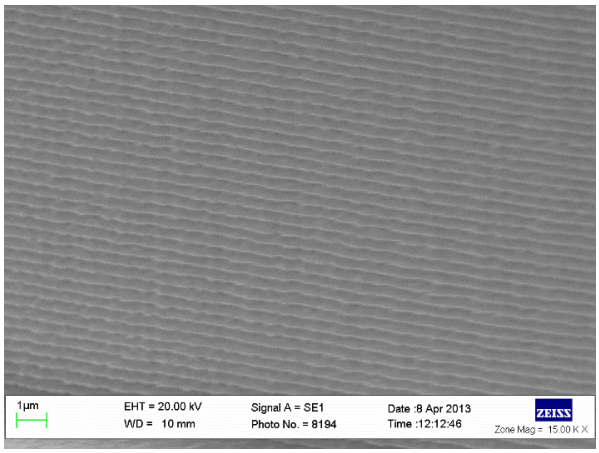

(a)

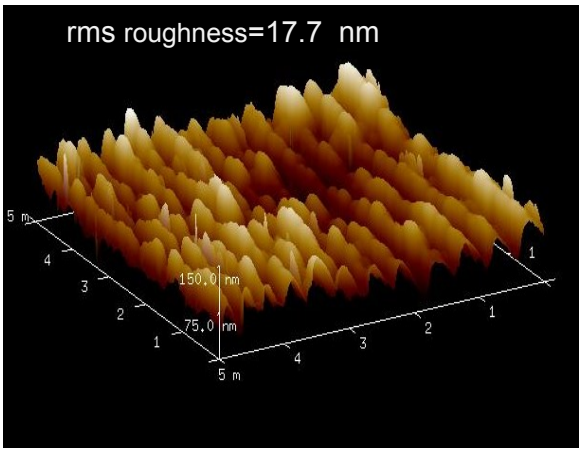

(b)

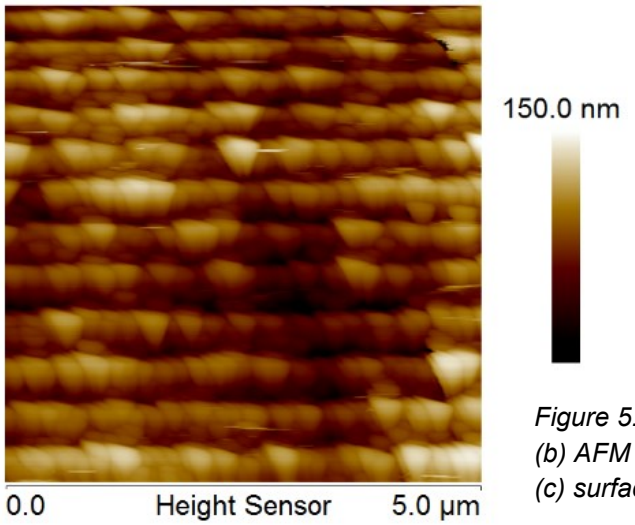

(c)

Figure 5.9 (a) SEM image after DRIE optimization; (b) AFM 3D image of sidewall after DRIE optimization; (c) surface roughness profile of sidewall.

The samples were cut using a dicing saw (Disco DAD 321) along the edge of the feature. A LEO 1430 Scanning electron microscope (SEM) and a VEECO Dimension 3100 Atomic force microscope (AFM) were used to characterize the sidewalls of the test structures.

5.3.2 Results and Discussion

The test structures were first etched with the optimized recipe to get relatively smooth sidewalls and vertical (close to 90 profile angle) features. The optimized DRIE recipe resulted in sidewalls with rms roughness of 17.7 nm, as shown in Figure 5.9(a) - (c). After the first cycle of oxidation + BOE, the sidewalls were characterized using SEM and AFM which is shown Figure 5.10(a)-(c). The sidewall rms roughness of the samples decreased to 5.35 nm (see Figure 5.10 (c)) which is very close to previously reported rms roughness of 5.93 nm for an oxidation time of 135 minutes at 1100 °C [57]. Additional oxidation time was found not to decrease the sidewall roughness significantly. The surface roughness after a 6 hour one-step oxidation + BOE process was measured to be 4.38 nm (see Figure 5.10 (d)-(f)).

I observed that splitting the oxidation process in two equal steps (initially 3 hours, then again 3 hours after BOE) is more effective than a longer, single oxidation + BOE process. This result can be explained by the characteristics of oxidation process which slows down as the oxide layer starts to thicken because of the difficulty of oxidant diffusing to the Si-SiO_2 interface. The rms roughness of the sidewall after a two-fold oxidation + BOE sequence was found to be around 2.56 nm, which can be compared to an rms roughness of 4.38 nm with the 6 hour one-step oxidation + BOE process. Figure 5.11 shows the final SEM images and rms roughness of the sidewall after the two-step oxidation + BOE process. A further oxidation + BOE cycle did not lead to significantly improved sidewall quality and may also affect device characteristics as the oxidation process consumes Si from structure each time at a rate of 44% of the grown oxide.

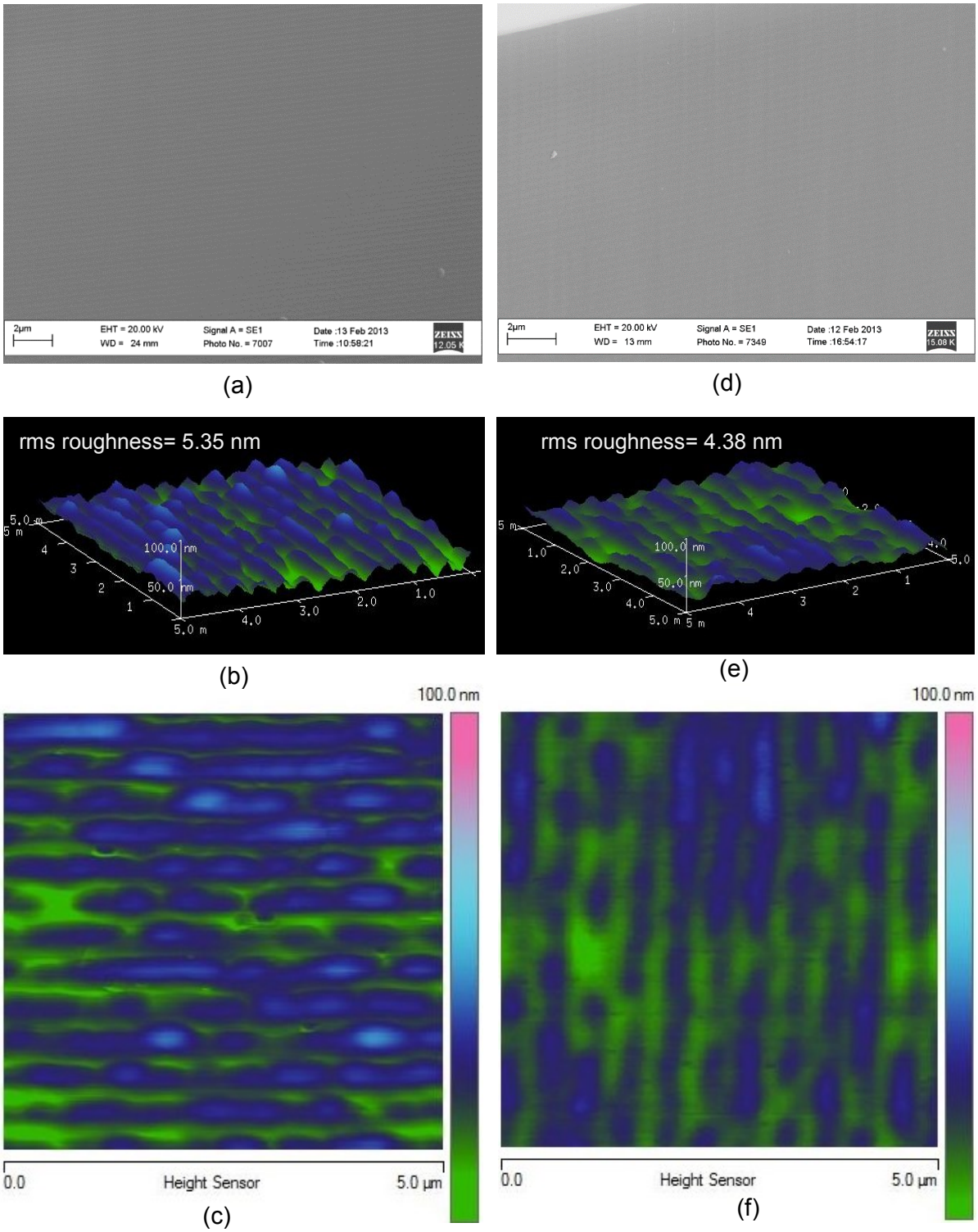

Figure 5.10 (a) SEM image after 3 hour oxidation + BOE; (b) AFM image after 3 hour oxidation + BOE; (c) AFM surface roughness (3 hour oxidation + BOE); (d) SEM image after 6 hour oxidation + BOE; (d) AFM image after 6 hour oxidation + BOE; (c) AFM surface roughness(6 hour oxidation + BOE).

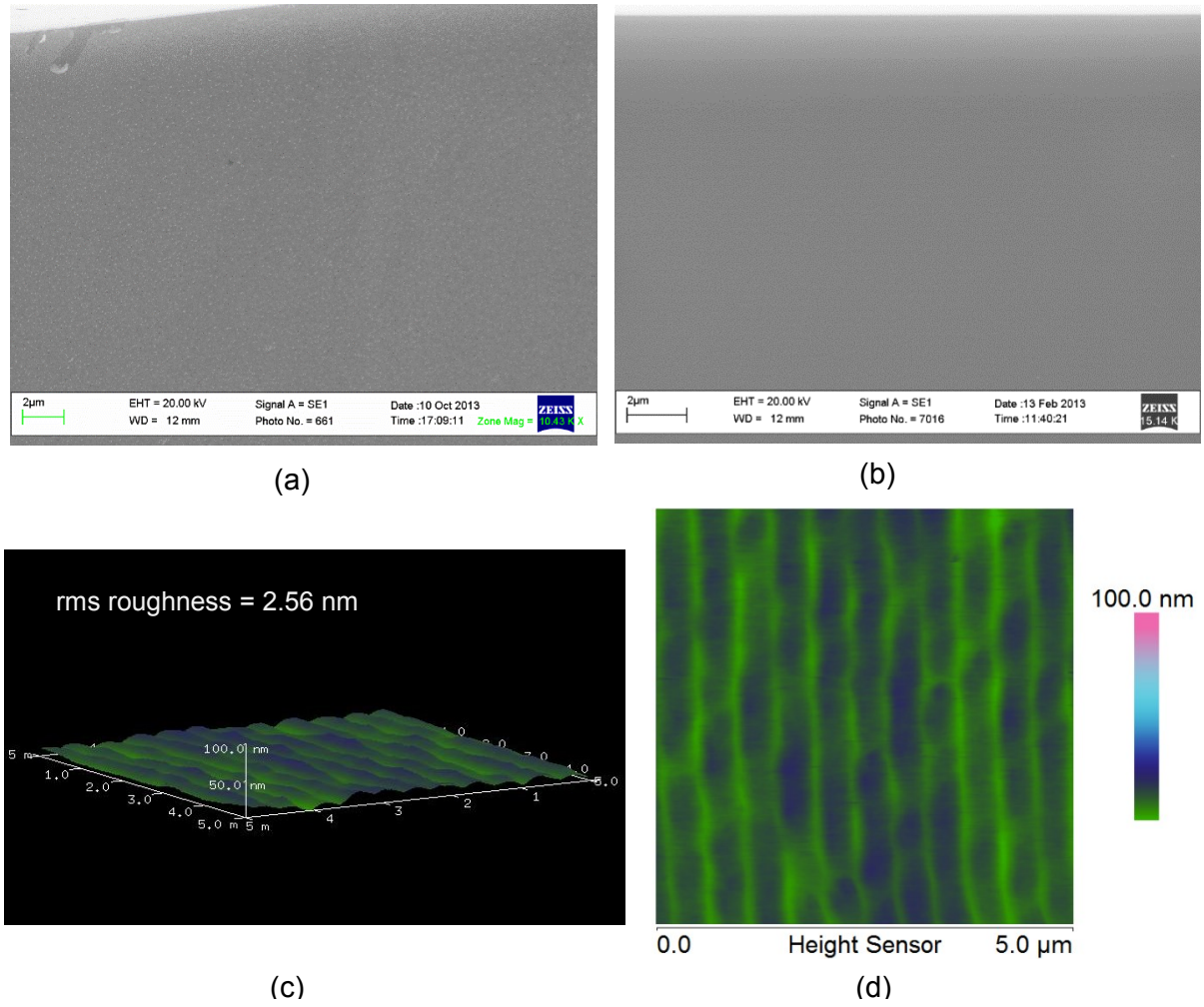

Figure 5.11 Images of the actuator sidewall after two cycles of 3 hour oxidation + BOE; (a) SEM image at the top position of the sidewall; (b) SEM image at the middle position of sidewall; (c) AFM 3D image; (d) AFM surface roughness profile.

The two step oxidation + BOE sidewall smoothing technique was applied to smooth the sidewall of the virtual pivot point actuator discussed in Chapter 4. After the smoothing process, thin layers of chromium and gold were deposited on the virtual pivot point actuators

using a sputtering process. The resultant sidewall of an actuator is shown in Figure 5.12. No sign of scalloped sidewall was found in the SEMS images of the actuator sidewall.

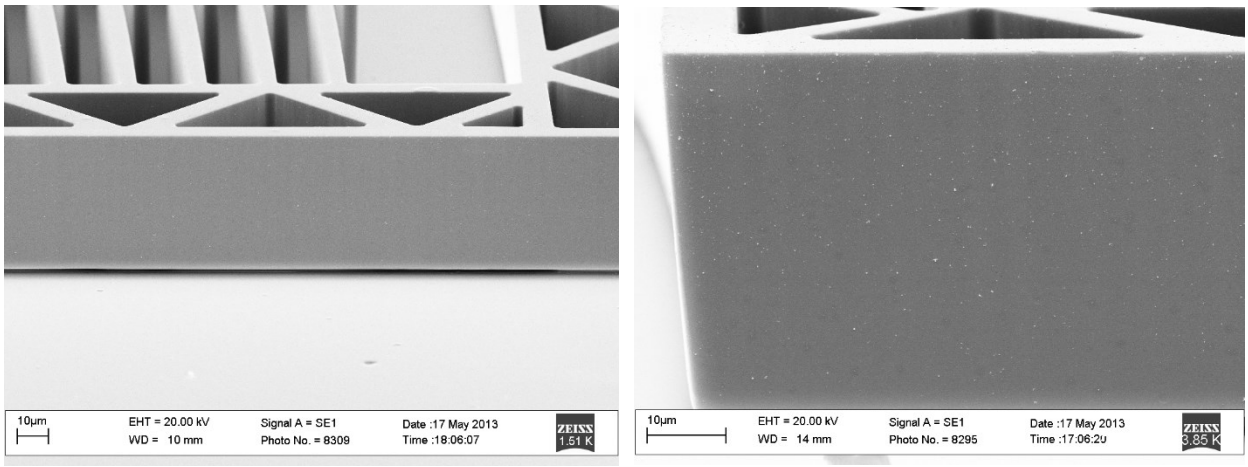

Figure 5.12 SEM images of smooth sidewall surface of a virtual pivot actuator.

5.4 Summary

In this chapter, I presented two techniques for smoothing a silicon sidewall to obtain a micro etched silicon surface of optical quality. The first method involved a systematically controlled over-passivation of the silicon sidewall during DRIE process. Different plasma parameters were carefully varied to achieve the final recipe of the controlled over-passivated smoothing technique. The rms roughness of the sidewall etched using this recipe is 3.89 nm. However, the controlled over-passivated process limits the maximum achievable sidewall depth to 120 µm. After that, vertical striation becomes visible on the sidewall. The controlled over-passivated technique also does not allow any subsequent wet chemical process of the wafer that can attack the polymer.

The second technique involved thermal oxidation of the silicon sidewall and then successive removal of the oxide. This method was applied to post-process the sidewall after DRIE. Temperature and time of the oxidation process were carefully chosen and a two-step oxidation + BOE process was found to be the optimum condition for obtaining an optical quality smooth sidewall. The rms roughness of the sidewall post-processed by two-step oxidation + BOE technique is found to be 2.56 nm. The mask for devices that will be post-processed by the two-step oxidation + BOE technique needs to be carefully designed as silicon is consumed at a rate of 44% of the grown oxide in the process. One advantage of the two-step oxidation + BOE technique is that there is no limit theoretically on the depth of the sidewall that can be smoothed by this process. The limit is imposed by the uniformly etched depth and profile verticality of the structure. Nevertheless, the mirror height cannot be greater than the substrate thickness (~ 400 μm) under optimal conditions. However, many applications may require larger sized mirrors. External mirrors need to be used in those scenarios.

6 Design, Fabrication and Characterization of a Long Arm Comb Drive Actuator with External Mounted Mirror[4]

6.1 Introduction

In previous chapters, I presented the design, fabrication and characterization of MEMS actuators with integrated sidewall mirrors, and smoothing techniques to achieve sidewalls of optical quality. MEMS devices with integrated mirrors have great potential to be used in many optical applications, including ECLs. However, the mirror should not be smaller than the diameter of the optical beam to avoid significant loss of light. Deep etched Si sidewalls have been used as mirrors or gratings in ECLs, as reported in the literature [12, 48, 49, 63, 65, 82]. The maximum reported height of those MEMS optical components is in the range of 75 to 100 μm [12, 49, 83], which limits the amount of light reflected back into the gain

[4] An article is prepared based on this chapter, and is to be submitted soon.

T. M. F. Amin , M. Q. Huda, J. Tulip, and W. Jäger, "Design and Fabrication of a Long Arm Comb Drive Actuator with Externally Mounted Mirror for Optical Applications", Journal of Microelectromechanical Systems, to be submitted.

medium from the external reflector. The achievable ECL tuning range was thus limited to about 50 nm.

Semiconductor lasers have typically elliptical beam profiles and, because of their small size, often a very diverging optical beams with divergence angles of up to 80°. The divergence angle is also different along the fast and slow axes of the beam. Collimating such a diverging light to a beam size of around 100 μm requires complicated optics, in particular, a miniature lenses with a very short focal length, which is still difficult to fabricate using micro-fabrication technology. The beam of a typical MIR semiconductor laser source for the current project has divergence angles of 25° and 50° along the slow and fast axes, respectively. Experiments with an optical bench setup, which were performed by co-researchers of the MIR ECL project [60], confirmed that it would be quite difficult to minimize the beam size to ~100 μm. These findings led then to the development of MEMS devices with mirrors of larger sizes. MEMS devices with large vertical mirrors can also benefit other applications where either the optical beam diameter is large or light scattering needs to be minimized. Examples of such applications are optical tomography, laser scanning systems, optical fiber sensing systems, high performance tunable optical filters and wavefront control systems [15, 40, 84-88].

Within the MIR ECL project, two different approaches were taken to increase the size of MEMS vertical mirror. In the first approach, which was pursued out by a collaborator [60] in the MIR ECL project, a mirror was fabricated as an extruded portion underneath the MEMS actuator, as shown in Figure 6.1. The actuator is similar in design to the one described in Chapter 3. In this process, the mirror was patterned first on the backside of the wafer along

the moving arm of the front side actuator. Everything beneath the moving portion of the actuator, except the patterned mirror, was then etched down to a depth equal to the required mirror height from the backside of the wafer. After that, everything beneath the moving portion, including the mirror, was etched until the SOI layer was reached and a polishing process was applied to smooth the mirror surface. An extended mirror of approximately 200 μm in height was fabricated beneath the MEMS actuator and then polished using a KOH + IPA recipe, as described in [89]. The collaborator used this actuator/mirror system as the external moveable mirror in a bench-top ECL and demonstrated EC lasing (see Figure 6.2). The mirror was further utilized to build a bench-top ECL in Littman configuration and a tuning range of approximately 10 nm was achieved [60].

Figure 6.1 SEM image of fabricated downward extruded mirror [89]

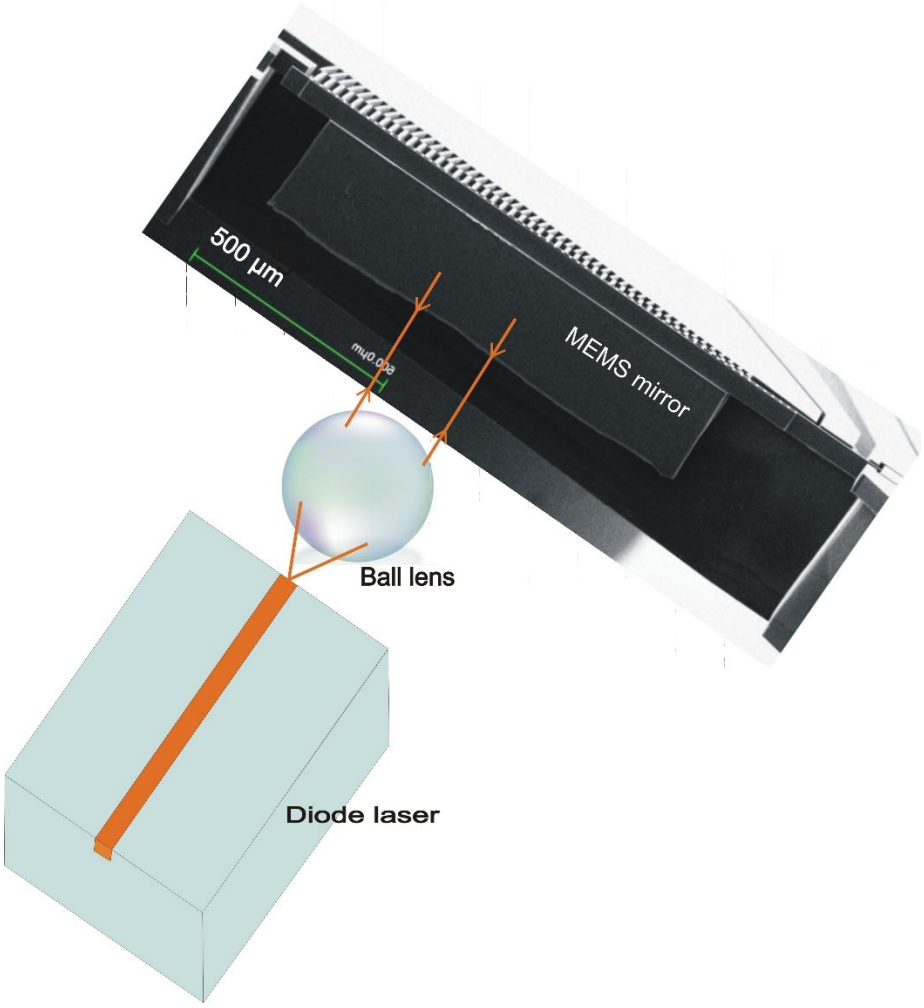

Figure 6.2 Schematic diagram of ECL demonstration setup

The maximum height of the mirror fabricated in extended bottom technique is always less than the thickness of handle layer since some silicon at the bottom of the mirror needs to be sacrificed to allow movement of the actuator. Etching process uniformity along the mirror thickness is also an issue for such MEMS mirrors. Another major constraint of deep etched micro-mirrors is the quality of the sidewall. Although the KOH + IPA technique was applied to

smooth the sidewall, the sidewall roughness was not satisfactory. Other smoothing techniques described in literature [72-74, 90] have different complicating issues, such as vertical striation as etch depth increases and non-uniformity across the etch depth, resulting in less than ideal mirrors [77, 91].

The second method pursued to fabricate a MEMS actuator with a large vertical mirror was to attach or mount an external mirror onto the actuator. As the mounted mirror or mirror material can be readily purchased, there are no issues of surface roughness in this case. In addition, this method provides flexibility with regard to the mirror size. External mirrors mounted on MEMS devices [63, 82] were also reported earlier, but the limited displacement afforded by these designs make them unsuitable for producing ECLs with large tuning range. A major challenge of this method is to develop an efficient mirror mounting process as MEMS devices are brittle and can be easily be broken during the mounting process.

In this chapter, I present the design and fabrication of an actuator with a long movable arm of 5.4 mm length which can provide 3° of rotation, equivalent to a translational displacement of 282 μm at the far end. The long arm of this actuator will provide sufficient space to work with and place optical components for building an ECL in a hybrid approach. I include the mechanical characterization of the actuator with mounted external MEMS mirror. I have also demonstrated development of a procedure for efficient mounting of external mirrors onto the MEMS devices to be used as a tuning element in an ECL.

6.2 Device design and modeling

Rotary comb actuators are particularly suitable to achieve wavelength tuning in both Littrow and Littman configured ECLs, as discussed in Chapter 2. I improved the rotary comb actuator design, discussed in Chapter 3, to support the required larger moving arm and greater displacement. Two support contact pads were inscribed at the end of the arm structure to mount the mirror onto the MEMS actuator. Comb fingers and truss were designed carefully to meet the stringent mechanical requirements of the long movable arm and the large displacement. A schematic diagram of the redesigned rotary comb actuator is shown in Figure 6.3.

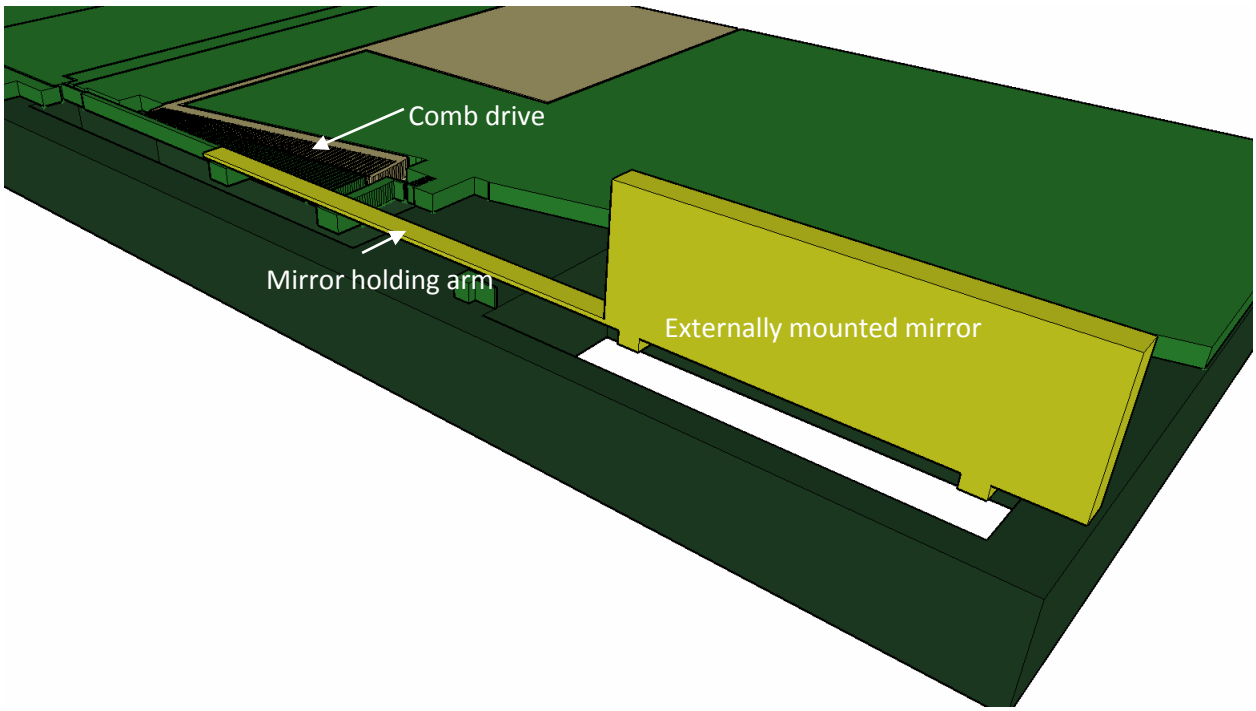

Figure 6.3 A schematic diagram of the long arm rotary comb actuator.

6.2.1 Design of the Comb Drive

The design requirements of around 3° rotation and a movable arm of more than 5 mm length brought about a number of challenges that needed to be addressed. As seen from the schematic diagram, the mirror holder and the comb drive are separated along the length of the arm. The traditional arrangement of comb fingers in a comb-drive actuator is to maintain a certain overlap between the moving and fixed fingers at all times. The arc length of the fingers needs to be greater than what corresponds to the desired rotation angle, and the arc length increases linearly with the radius in the rotary comb drive. The width of the fingers also needs to be large enough to avoid any undesired bending due to side forces created by the large overlap area and fabrication imperfections. However, this traditional arrangement would require very long comb fingers at larger radius, which must be accompanied by increased finger width. The greater finger width makes the structure heavier and also reduces the number of fingers that can be fitted within a certain length. Consequently, less force is produced to rotate the device, which increases the voltage requirement. To solve this problem, the comb fingers were designed in such a way that only a few of them are engaged initially and the rest of the comb fingers engages gradually when the structure starts to rotate, as shown in Figure 6.4. This arrangement of comb fingers is partially similar to a comb drive that was described in the literature to make space for other components [64]. This type of comb drive can be called “zipped comb drive” because of its resemblance with a zipper. A gradually engaging structure is called “zipping actuator” in the literature [92]. The engagement of all the comb fingers in a zipped comb drive occurs when the device rotates by a certain designed angle. In this way, the voltage requirement for the actuator could be kept low (130 V) because the force generated in the zipped comb actuator is same as in a

conventional comb drive if all fingers are engaged. All the comb fingers maintain the same end gap at full engagement. This design leads to reduced comb finger length at higher radial distance and more comb fingers can be accommodated within the structure. The overall reduced overlap area during engagement in the zipped design also reduces the side instability force. However, the actuation characteristics of the zipped comb drive do not follow that of the standard comb drive.

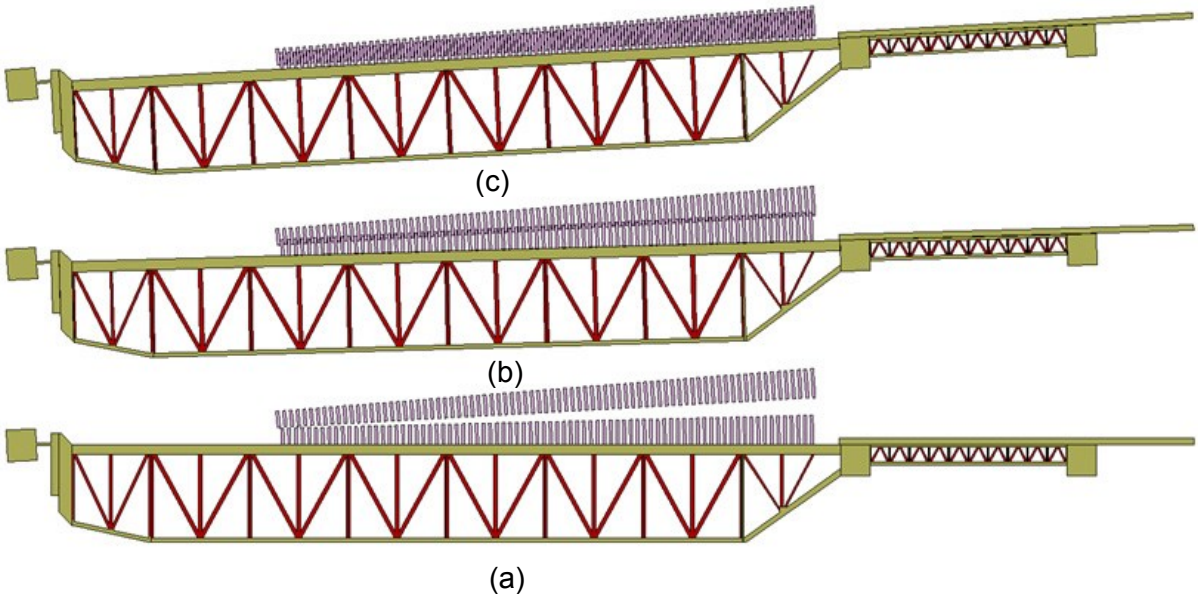

Figure 6.4 Design of the zipped comb finger: (a) Initially only a few fixed and moving fingers overlap each other; (b) all the comb fingers overlap each other at certain designed angle; (c) at completely interdigitated position, all the moving comb fingers maintain the same end gap.

The number of engaged fingers at a certain rotation angle for the zipped structure can be expressed as:

$$N(\theta) = \begin{cases} N_0 + \dfrac{\theta}{\theta_{eng}}(N_T - N_0);\ for\ \theta < \theta_{eng} \\ N_T;\ for\ \theta \geq \theta_{eng} \end{cases} \qquad \textit{Equation 6.1}$$

Here, N_0 is the number of initially engaged fingers, N_T is total number of fingers of the device and θ_{eng} is the designed rotation angle when all fingers are fully engaged. The electrostatic force created in the zipped comb drive becomes a function of angle, and is given by:

$$F(\theta) = \frac{N(\theta)\epsilon h V^2}{g} \qquad \textit{Equation 6.2}$$

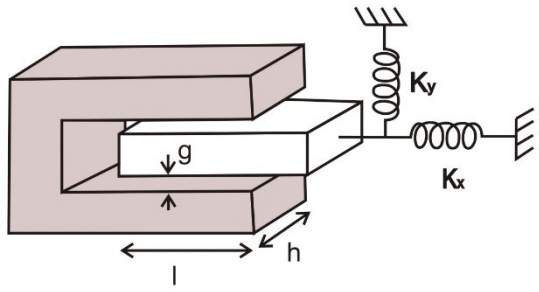

Figure 6.5 Stiffness constants of the comb drive in X and Y directions.

Equation 6.2 expresses that the force generated in the zipped comb drive is less than that of a typical comb drive at the beginning of actuation with the same total number of fingers. When all fingers are fully engaged, the force is equal to that of a traditional comb drive. In Figure 6.6, this difference between zipped comb drive and pre-engaged comb drive is represented graphically. One important thing to notice is the sharp rise of the actuation curve of the zipped comb drive near 90 V. Before complete engagement, the force in the zipped comb drive is proportional to the number of comb fingers and the square of the voltage. At lower actuation voltage, the number of comb fingers dominates in the force generation and thus the actuation curve is more linear. At higher voltage when all the comb fingers are close

to engage, the voltage factor dominates in the force generation and the relationship is parabolic. At near engagement, where the force and consequently the rotation of both pre-engaged and zipped design must be same, a sharp rise in the actuation curve is therefore observed.

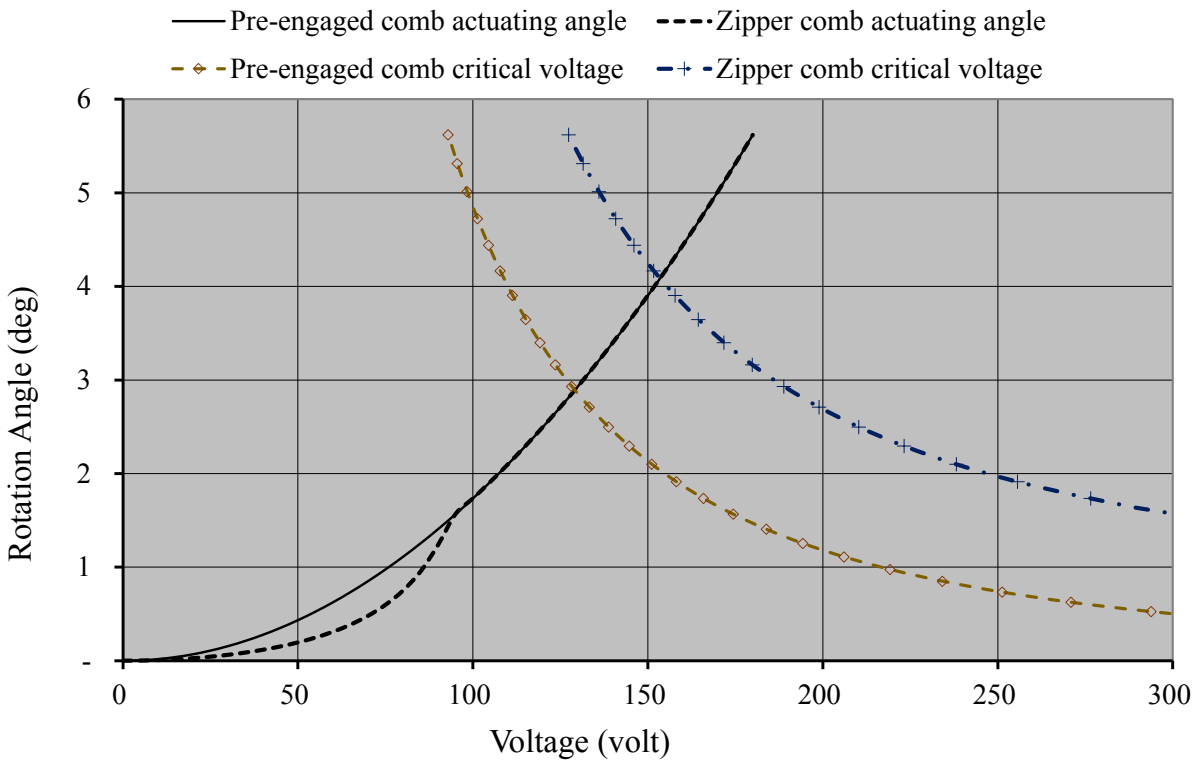

Figure 6.6 Actuation characteristics and critical voltage comparison of the pre-engaged comb design and zipper comb design.

The stability of a rotary comb actuator depends on two factors: radial stiffness of the actuator and any unbalanced radial force between the comb fingers. There is always some side unbalanced force in a rotary comb structure due to different overlap area on both sides of the moving comb. However, the main contributor to the side force is the finger gap mismatch on

both sides of a finger, which is a result of fabrication imperfections. The net electrostatic force from the finger gap mismatch between moving and fixed fingers can be expressed as:

$$F_{net} = \frac{\epsilon h l V^2}{2(g-y)^2} - \frac{\epsilon h l V^2}{2(g+y)^2} - K_y y \qquad \textit{Equation 6.3}$$

Here, l is the overlap length between the comb fingers, K_y is the stiffness constant in y-direction and y is the amount of gap mismatch, which is the displaced position of the moving comb finger from its usual middle position between fixed comb fingers.

The critical voltage is the minimum voltage at which the moving comb fingers will snap to the fixed comb fingers at the side. The critical voltage for instability can be determined by differentiating Equation 6.3 with respect to y and is given by:

$$V_{crit} = \frac{\frac{K_y y}{\epsilon h \sum_{n=1}^{n=N(\theta)} l_n}}{\frac{1}{(g-y)^3} + \frac{1}{(g+y)^3}} \qquad \textit{Equation 6.4}$$

Equation 6.4 describes the dependence of the critical voltage on the comb drive parameters. It shows that the critical voltage is inversely proportional to the total overlap area between the fingers. Thus reducing the overlapping area by zipping the comb drive also improves the side stability of the actuator significantly. Figure 6.6 shows a comparison of the critical voltage between pre-engaged comb drive and zipped comb drive assuming a gap mismatch of 1 μm between fixed and moving comb fingers. If the gap mismatch between the comb fingers can be lowered, for example through an improved fabrication process, the critical voltage will

further increase as the denominator of Equation 6.4 will become smaller. The zipping of the comb also contributes to a larger y-direction stiffness constant as it reduces the total overlap area between the comb fingers and reduces mass, which was also confirmed by simulation.

The two outside fingers of the fixed comb were designed to be thicker than the other comb fingers as they experience an electrostatic force only from one side and are therefore more prone to bending. There is no set rule to determine how much wider the last comb fingers should be. It mainly depends on the material and the length of the comb fingers. Even though the comb fingers are zipped in this design, the arc length of fingers especially at the far end is about 156 μm. I therefore designed the last comb fingers to be 3 times thicker than the other fingers.

6.2.2 Design of the Truss

The design of the truss is important as the axial bending of the truss due to the side force can lead to instability for such a long MEMS structure. Equation 6.4 reveals that K_y is one of the contributors for the critical voltage and K_y depends mainly on the axial strength of truss. I optimized the truss design to achieve a high value for the axial stiffness constant using the FEA simulation software COMSOL. Force was applied in the y direction of different truss designs to determine the displacement in y-direction and the stiffness constant was measured using Hooke's law. Figure 6.7(a) shows the simulated behavior of the structure with a typical truss design. The stiffness constant in axial direction, K_y, is approximately 9900 N/m for a truss width of 130 μm. Increasing the width of the truss and varying it over the length from 200 μm to 350 μm leads to an increase of the stiffness constant to 27300 N/m.

The truss design was then modified structurally similar to the Warren truss design [54], as shown in Figure 6.7(c), with more internal support elements to improve its rigidity. A stiffness constant of 90,000 N/m was achieved for a truss width of 450 µm.

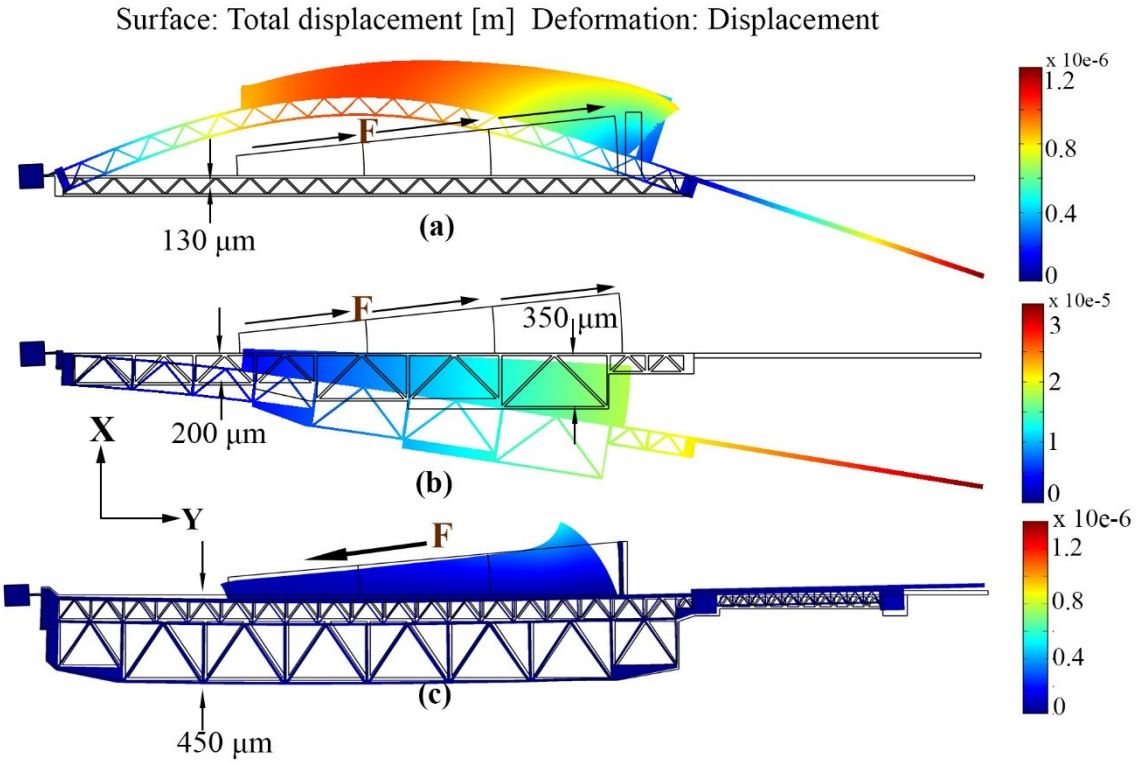

Figure 6.7 Different truss designs: (a) Traditional truss; (b) a modified design with varying truss thickness across the length; (c) final truss design with a zipped comb drive.

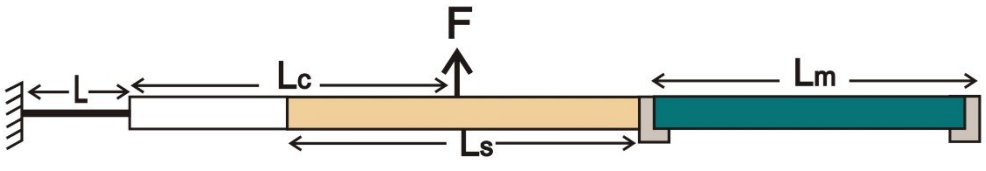

Figure 6.8 Point force equivalent model of the structure.

6.2.3 Mechanical Modeling of the Structure

For simplicity, the MEMS structure can be modeled using a point force F applied at the middle position of the engaged comb fingers, as shown in Figure 6.8. The force position from the tip of the cantilever beam can be expressed as:

$$L_f(\theta) = \left(L_c - \frac{L_s}{2}\right) + N(\theta)(w_f + g) \qquad \textit{Equation 6.5}$$

Here, L_c is the distance between the tip of cantilever beam and the point at which the force acts when all the comb fingers are engaged, w_f is the comb finger width, L_s is the span length of all the comb fingers. The displacement at the cantilever beam tip can be calculated using the moment area method [54] and is given by:

$$x = \frac{F(\theta)L^3}{3EI}\left(1 + \frac{L_f(\theta)}{\frac{2L}{3}}\right) \qquad \textit{Equation 6.6}$$

Here, E is the Young's modulus of silicon and I is the area moment of inertia of the beam. The displacement of the zipper comb drive at the cantilever tip is plotted as a function of voltage in Figure 6.6. The curve confirms the initial smaller displacement of the actuator compared to a pre-engaged comb drive, which is a result of the smaller force generated at low rotation angles, as predicted by Equation 6.2. The displacement at the end of the mirror can also be calculated using the moment area method, and the overall spring constant of the structure can then be determined using Hooke's law. The spring constant is given by (please see Appendix B):

$$K_x = \frac{3EI}{L^3}\left(1 + \frac{3L_c}{L} + \frac{3L_s}{4L} + \frac{3L_m}{2L} + \frac{3{L_c}^2}{L^2} + \frac{3L_cL_s}{2L^2} + \frac{3L_cL_m}{L^2} + \frac{{L_c}^3}{YL^3} + \frac{3{L_c}^2L_s}{4YL^3} + \frac{3{L_c}^2L_m}{2YL^3}\right) \quad \textit{Equation 6.7}$$

Here, L_m is the length of the mirror and Y is the ratio of area moment of inertia between the equivalent width of the truss and the beam.

Table 6-1 Final design parameters of the long arm actuator.

Symbol	Parameter Name	Value
L	Beam length	75 μm
w	Beam width	12 μm
h	Device thickness	100 μm
fw	Average finger width	10 μm
g	Average gap between fingers	2.5 μm
Ls	Total comb span length	2600 μm
N	Total number of comb finger	104
L_m	Mirror holder length	1395 μm
T	Total length of the device	5410 μm

The stiffness constant is an important parameter in the design of the actuator because of its influence on displacement and resonance frequency. A low value for the stiffness constant allows for large rotation angles at reasonably low voltage. On the other hand, a high value is

required to support the large external mirror, since the resonance frequency of the structure may otherwise be too low for operation at the desired frequency. The resonance frequency of a sensor or actuator device is generally desired to be relatively high as it improves shock resistance and allows for higher operating frequencies. There is therefore a trade-off necessary for the device design. The device parameter optimization was performed based on the application requirements of high actuation voltage and large mirror size. The detailed design parameters are given in Table 6-1.

Assuming a harmonic oscillator, the resonance frequency for a structure is given by:

$$f = \frac{1}{2\pi}\sqrt{\frac{K}{M}} \qquad \textit{Equation 6.8}$$

Here, M is the effective mass of the structure. The effective mass for this structure can be determined using Raleigh's method [93] and is given by:

$$M = m_b + m_t + m_f + m_m \qquad \textit{Equation 6.9}$$

Here, m_b, m_t, m_f and m_m are the effective masses of beam, truss, comb fingers and mirror respectively. The detailed analytical calculations for the individual effective masses are presented in Appendix C. Equation 6.8 describes the dependency of the resonance frequency on the effective mass of the device. The external mirror mass is the greatest contributor to the total mass of the device. An equivalent solid truss width was approximated during the analytical calculation of the resonance frequency. I performed simulations using the software Intellisuite to determine the resonance frequency. Figure 6.9 shows a

comparison of the resonance frequencies from the analytical model and the simulation. From the comparison between the two models, it can be concluded that the analytical model is quite sufficient to predict the resonance frequency of the comb-drive actuator, although the FEA analysis can be assumed to be more accurate.

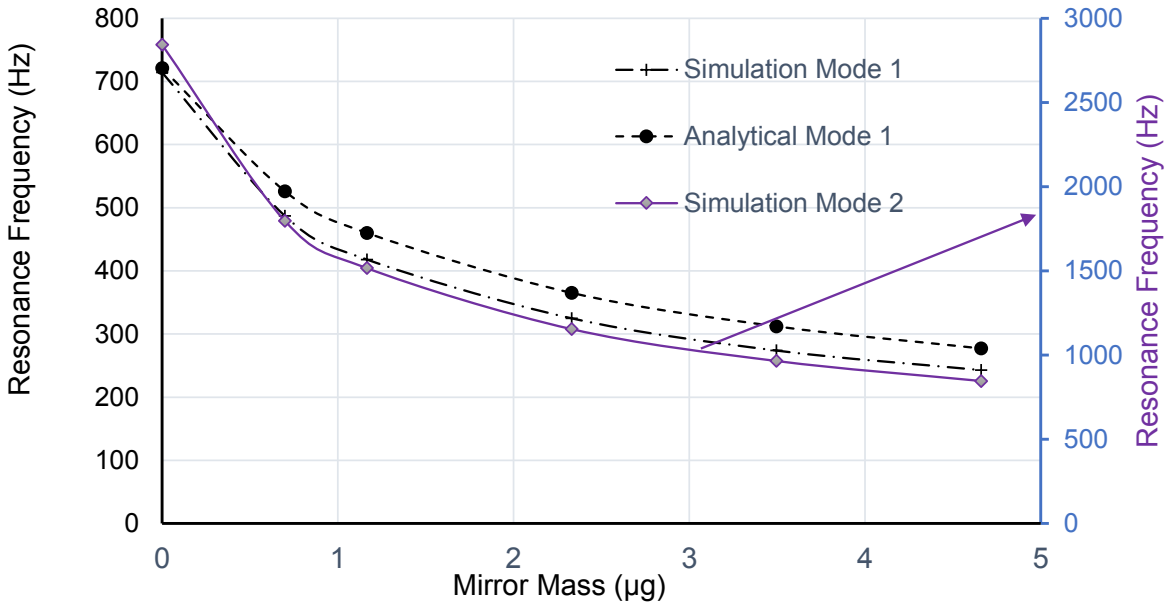

Figure 6.9 Variation of resonance frequency of the actuator as a function of mounted mirror mass

6.3 Fabrication

The actual device has dimensions of 1 mm x 6 mm and was fabricated on a 4 mm x 8 mm chip. An SOI wafer with device layer thickness of 100 µm, buried oxide layer of 2 µm, and substrate layer thickness of 300 µm was used for the device fabrication. Bulk micro-machining was performed from both sides of the wafer, involving two level masking. The mask sets were designed with largely spaced open areas around the individual devices to

facilitate easier mounting of the external mirror and easier alignment of the light beam onto the mirror (see Figure 6.10). Only the anchor, contact electrode pad and the fixed comb portion were present on the back side of the device. This requirement, however, made the fabrication process quite challenging. I initially tried using the back cavity fabrication approach, successfully implemented earlier by our group, to fabricate the rotary comb actuators [94]. The devices were very densely populated within the mask which led to continuous open areas throughout the wafer. As a result, the wafer broke during the DRIE processing step as the wafer weakened from the huge backside Si removal. The wafer could not withstand the pressure from the clamps (see Figure 6.11(a)) used to hold the wafer tightly in the DRIE chamber.

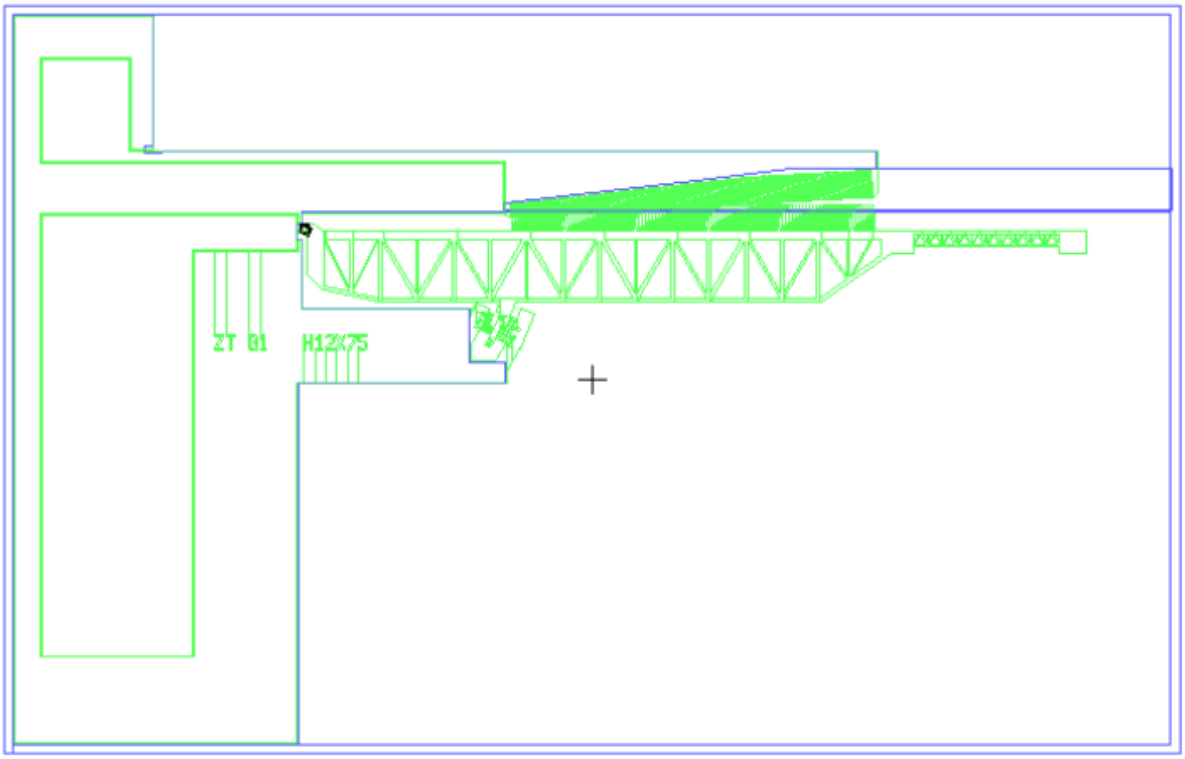

Figure 6.10 Single cell mask outline in L-Edit mask design software; the blue line shows the back side mask.

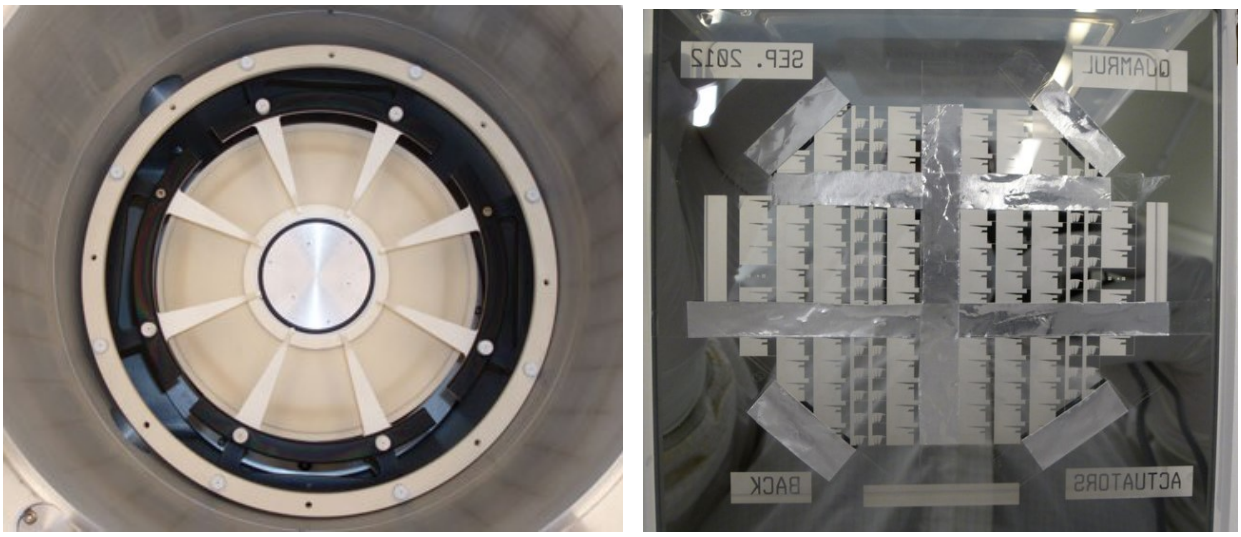

(a) (b)

Figure 6.11 (a) Clamps to seal the wafer in the DRIE chamber (picture taken by nanofab staff, Scott Munro); (b) modification of the mask using aluminium foil.

To make the wafer stronger, I modified the backside mask using aluminum foil during photolithography. Some of the continuous open areas were closed to make the wafer stronger. The wafer was also mounted on a carrier wafer to reduce the backside helium pressure on the actual wafer. The wafer could then be smoothly run through the DRIE chamber. However it broke in other processing steps such as during spinning photoresist for front side patterning, during drying after the wet process or during dicing when the wafer is rolled to remove the trapped air. Further modifications of the mask improved processing significantly, but it was still difficult to handle the full wafer because of the thinned areas and uneven wafer surface. These difficulties led to the development of a fabrication process that involved patterning of both sides of the wafer before any deep etch, which is shown schematically in Figure 6.12(a)-(j).

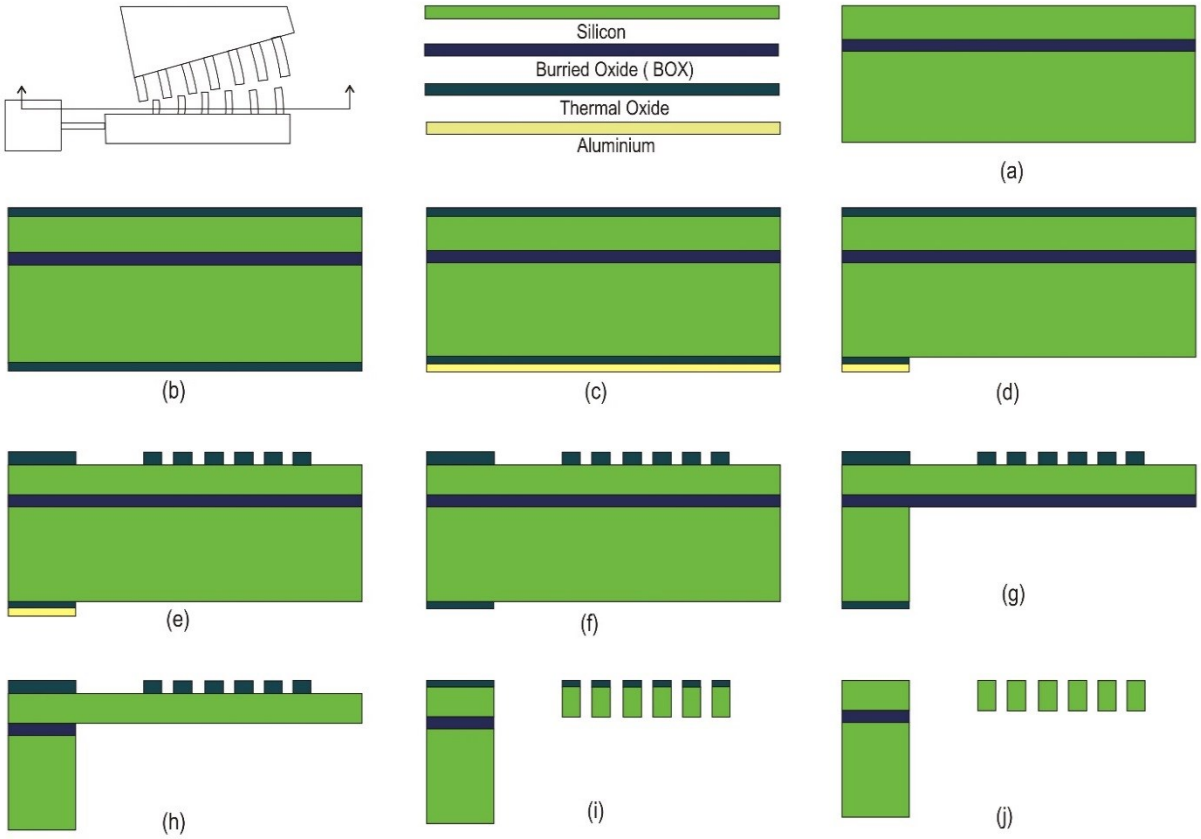

Figure 6.12 Fabrication of the actuator step by step; (a) SOI Wafer; (b) thermally grown oxide on both sides; (c) Al sputtering on back side; (d) patterning of Al, etching Al layer and oxide layer; (e) patterning of front layer; (f) removal of Al from back side; (g) removal of Si using DRIE; (h) removal of buried oxide; (i) etching of Si device layer; and (j) removal of residual thermal oxide from the top layer.

At first, a thermal oxide layer of 3.5 μm thickness was grown on both sides of the wafer by performing wet oxidation for 30 hours at 1050 °C. SiO_2 was used as masking layer to utilize its higher etching selectivity over Si (100:1). Aluminum (Al) was then deposited on the backside of the wafer with a sputtering process to assist the alignment of front and back patterns. The Al layer on the backside was patterned by photolithography using HPR 506

photoresist followed by etching with commercial Al etchant (16:1:1:2 solution of phosphoric acid, nitric acid, acetic acid, and water).

The pattern was then transferred onto the oxide layer by etching the SiO_2 layer using a reactive ion etch (RIE) process. The same process, except the Al patterning steps, was used to pattern the front side SiO_2 layer. The back side Al layer, opaque to infrared light, assisted the alignment process without any deep etch. After this stage, the wafer was diced into individual dies for further processing. Batches of 10 to 20 dies were then mounted on a carrier wafer and deep etching of Si down to the buried oxide layer was performed from the back side. An optimized deep RIE (DRIE) recipe was used in an STS inductively coupled plasma (ICP) machine to achieve good vertical feature profiles. Subsequently, the buried oxide layer was removed using RIE from the back side. The dies were then un-mounted from the carrier wafer and thoroughly cleaned. I mounted them again on a carrier wafer and performed DRIE from the front side to transfer the pattern onto the Si device layer from the oxide mask. The actuators were released upon completion of this stage. The residual oxide mask layer was then removed using RIE and thin chromium and gold layers were deposited using a sputtering process for better electrical contact. An SEM image of a fabricated device is shown in Figure 6.13.

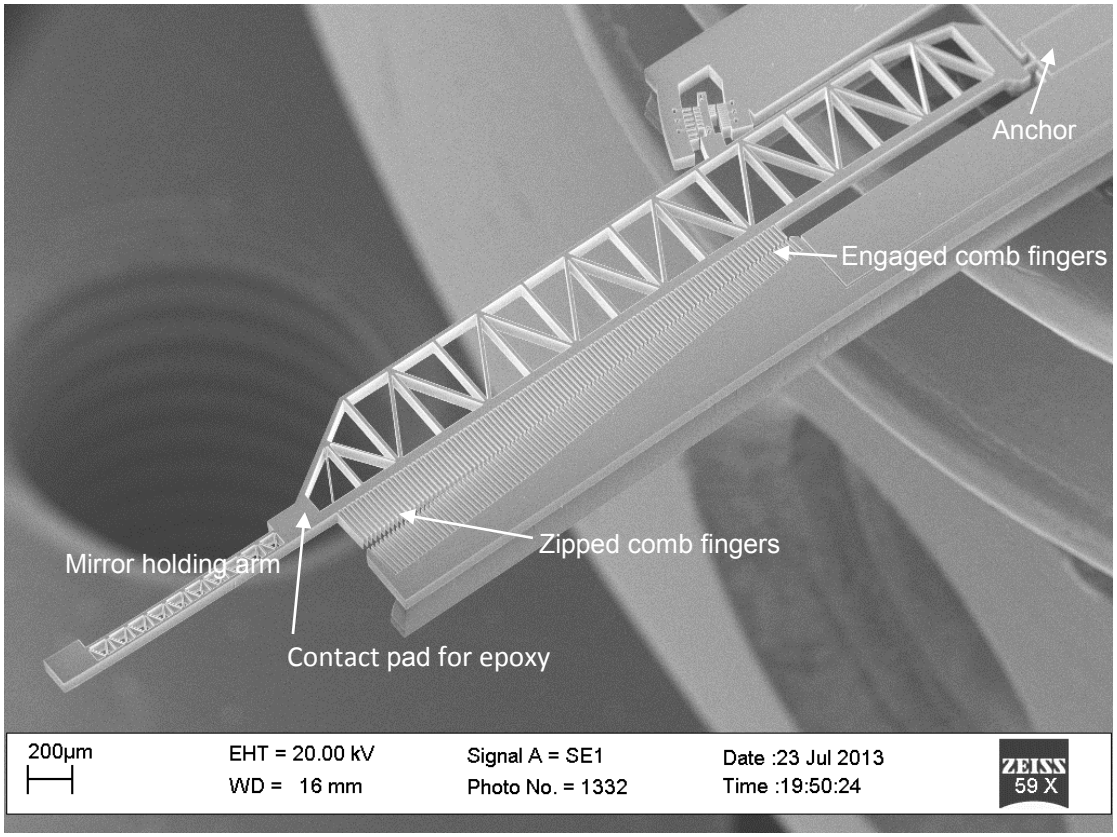

Figure 6.13 SEM image of a fabricated long arm actuator

6.4 Mounting of External mirror

Mounting an externally fabricated mirror onto the released MEMS devices is a challenging task as the devices can be easily destroyed if not done precisely. Two contact pads were inscribed at the top and bottom of the right truss in my design to facilitate mounting of an external mirror, as shown in Figure 6.13. The external mirror should be as thin as possible to avoid unnecessary mass which would reduce the resonance frequency of the device. A

standard Si wafer can be used to fabricate thin mirrors using a DRIE process to etch it down to the desired thickness. However, variation of etching rate throughout the wafer in the DRIE process made the thickness of the wafer non-uniform which made it extremely difficult to handle. There are also difficulties associated with un-mounting the thinned wafer from the carrier wafer. The Si mirrors were therefore fabricated from a commercially available 100 μm thin Si wafer, polished on both sides. The wafer was first diced into different suitable mirror sizes (length 1 mm to 2 mm and height 500 μm to 1 mm) using a Disco DAD 321 dicing saw. Thin layers of chromium (Cr~15 nm) and gold (Au ~50 nm) were then deposited onto the individual mirror pieces through sputtering. Gold was used on the mirror surface to increase its reflectivity in the infrared range.

I developed an efficient method to mount the external mirror onto the MEMS device to minimize problems associated with manual handling of the thin Si mirrors. A die bonding system consisting of a microscope, a moving stage, a heater, and a vacuum tip, was used to develop the mirror mounting method. Epotek H20E silver filled epoxy [95] was used as the bonding material between the MEMS device and the mirror. The epoxy can be cured by keeping at 120 °C for 15 minutes. The mirror mounting setup is shown in Figure 6.14. As shown in the figure, the white box under the microscope is the moving stage that is controlled by the black arm underneath it. The black box on the right side is the heating controller which was used to cure the epoxy. The die bonding system (Figure 6.14(a)) has different types of vacuum tips just above the movable stage. An enlarged view of the tip assembly is shown by the arrow. I used the second tip from the left. The needle was used to pick up a drop of epoxy and the vacuum tip (next to it), which has a slot to keep the mirror straight, was used to pick up the mirror piece and to release it.

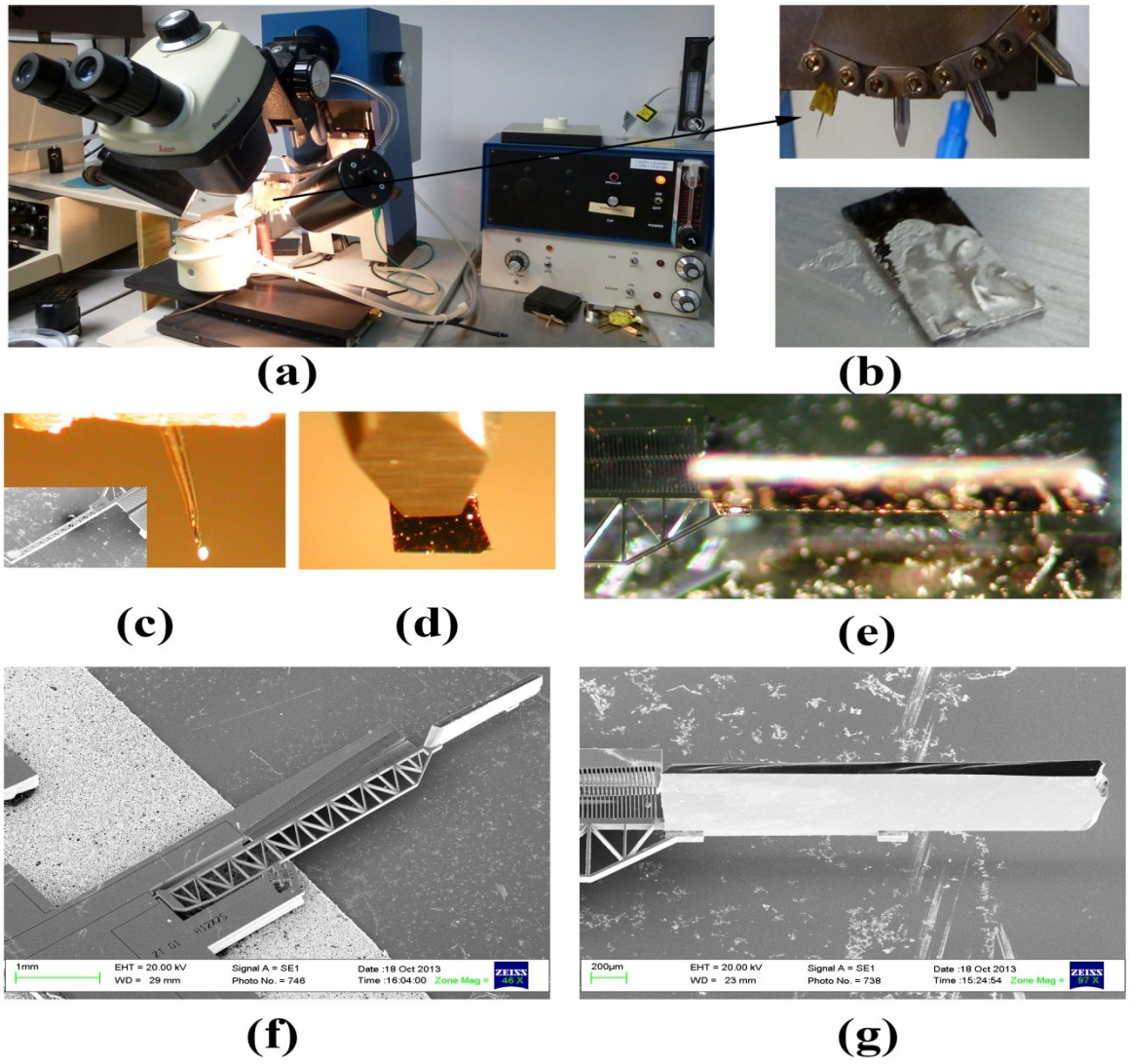

Figure 6.14 Mirror mounting setup and mounting process; (a) die bonding machine used for mounting the mirror (the enlarged part of the picture shows all available needles); (b) silver epoxy mixture; (c) drop of epoxy at the tip of the needle (the inset picture shows the epoxy on the mirror holder pad); (d) mirror picked up by a vacuum tip; (e) optical microscopic image of a mounted mirror; (f) SEM image of an actuator with mounted mirror; and (g) SEM image of a mounted mirror .

Figure 6.14(b)-(c) shows the epoxy mixture and a tiny dot of epoxy on the needle. The inset picture in Figure 6.14(c) shows drops of epoxy that had been put onto the mirror pad. A mirror picked up vertically by the vacuum tip is shown in Figure 6.14(d). The mirror piece was

aligned with the mirror holder on the MEMS actuator and released onto it with the help of the microscope and moving arm. Figure 6.14(e) shows an optical image of the actuator with mounted mirror. The reflection of the surface underneath can be seen in the mirror. SEM images of an actuator with mounted mirror and an enlarged view of the mounted mirror are shown in Figure 6.14(f)-(g), respectively.

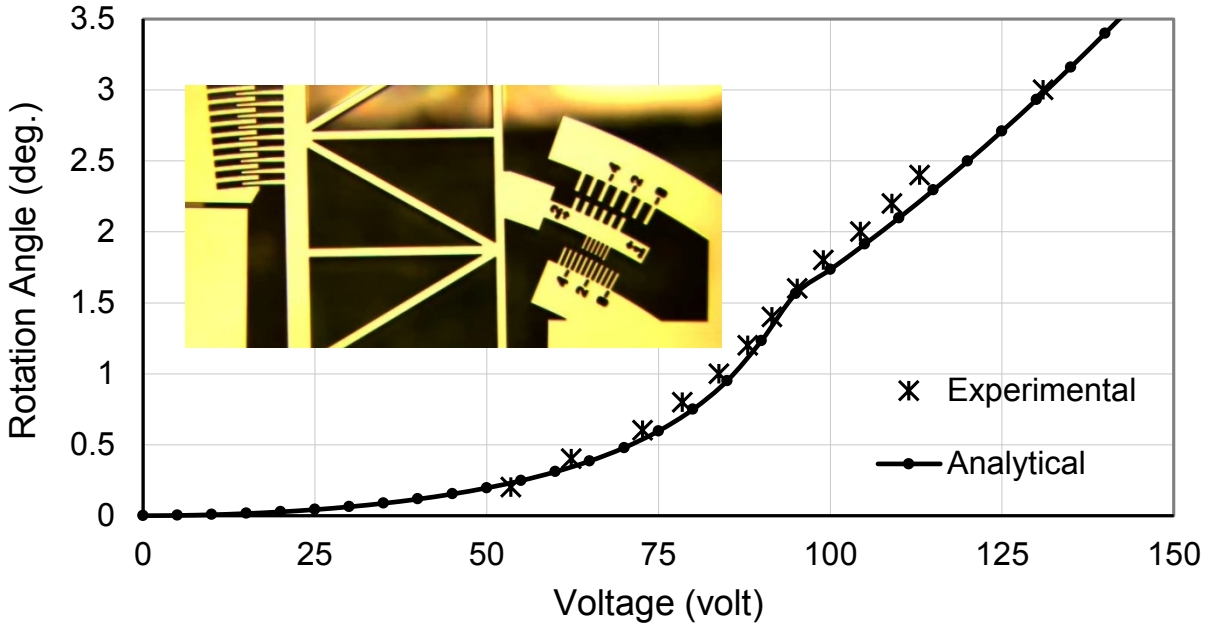

Figure 6.15 Measured rotation of the actuator as a function of voltage.

6.5 Results and Discussion

Actuator devices of two different designs were fabricated in different batches. The two designs have same dimensional parameters, given in Table 6-1, except the beam width. Mirrors of different sizes were mounted onto those devices using the mirror mounting method described in the previous section. The actuators were then characterized to determine their

electrical and mechanical properties. I used a Wentworth probing station for electrical characterization and an optical technique for mechanical characterization of the devices.

6.5.1 Device Actuation

The devices were actuated by supplying a voltage to the designed contact pads through probe electrodes. A rotational Vernier scale was inscribed within the device for easier experimental reading, as shown in the inset picture of Figure 6.15. The Vernier scale was designed to take readings as low as 0.1° in change of rotation angle. As I used an optical microscope (8X optical zoom and 3X digital zoom) in the wafer probing station to take the measurements, the experimental error is estimated to be minimal, around ±0.025°. The measured rotation angle of the actuator is plotted against voltage in the same figure and compared with the analytical results. In general, the experimental actuation results compare well with the analytical prediction. The singularity in the 80 to 90 V region, as predicted analytically, is also observed experimentally. However, the experimental results of actuators from different fabrication batches show small discrepancies which are a result of small variations of the device dimensions from processing. Significant deviations of the actuation results before and after mounting the mirror were not observed, which is in accord with Equation 6.6.

6.5.2 Mechanical Characterization

An optical bench setup in combination with the probing station was used for this characterization. The complete experimental setup is shown in Figure 6.16.

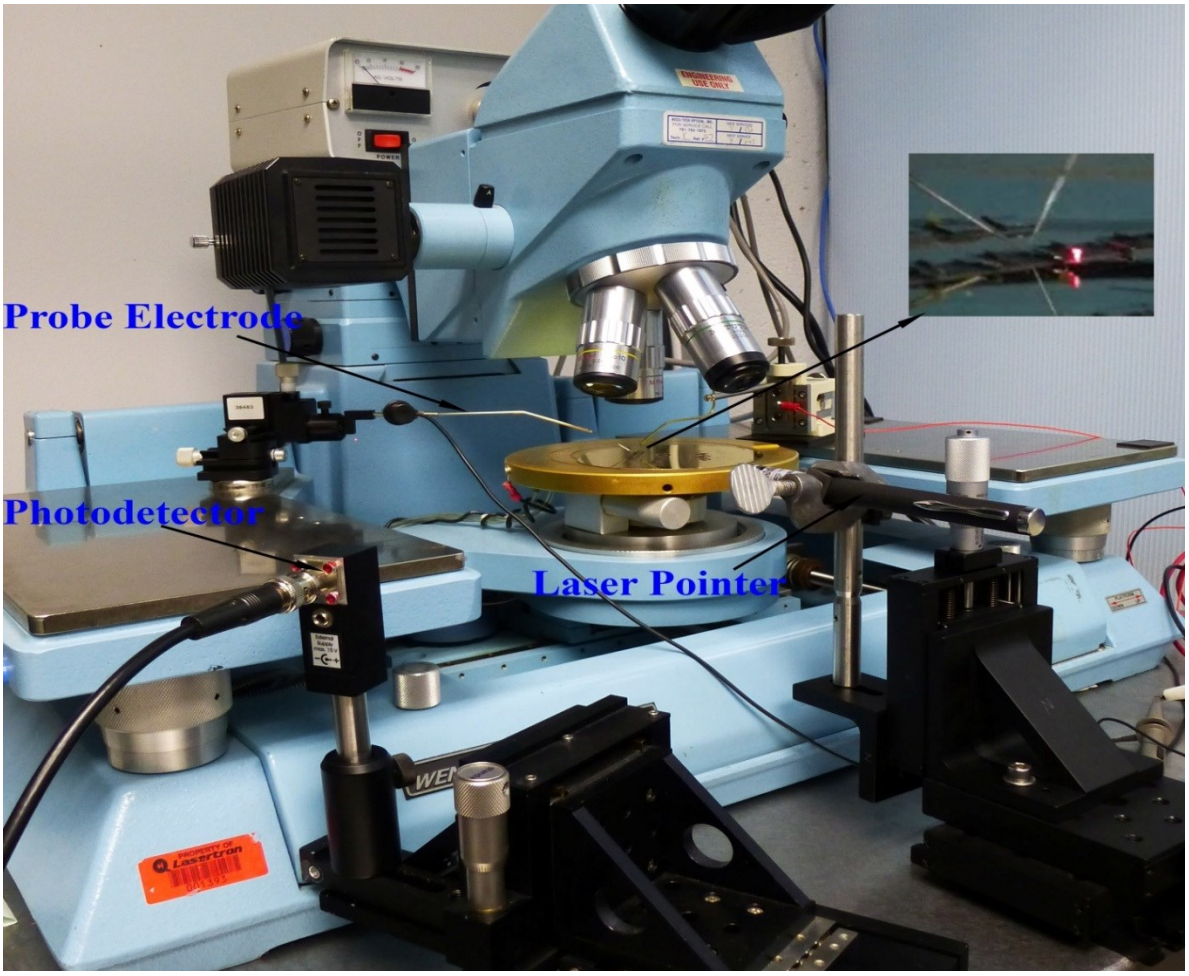

Figure 6.16 Experimental setup for characterization using optical techniques (the inset picture shows the laser beam spot on the mounted mirror).

As seen from the figure, a laser pointer with emission wavelength of 630-680 nm (power <5 mw) was aimed at the mirror attached to the actuator. The reflected light from the mirror was detected by a photodetector with a detection range of 320-1100 nm. The beam size of the laser pointer is 2 mm x 1.8 mm at a distance of 10 cm from the laser pointer to the mirror

surface. The sensitive area of the detector is approximately 0.5 mm^2. As the detector can only detect a portion of the light, I fixed the detector at the position of maximum output for a certain actuation voltage. Figure 6.17 shows the captured oscilloscope trace of the photodetector response after an actuation voltage of 90 V was applied. As seen in the figure, the actuator underwent a damped vibration about the actuated position. Vibration of mechanical structures is a natural phenomenon, but it is expected to be minimal for an actuator. Damped vibrations of MEMS actuators are discussed in literature [96, 97]. Viscous energy dissipation in the air determines the nature of vibration in laterally driven micro-actuators.

Table 6-2 Comparison of resonance frequency.

Mirror Size	**Analytical**	**Simulation**	**Experimental**
2 mm x 100 μm x 1 mm	277 Hz	243 Hz	246 Hz

I measured the resonance frequency of the damped vibration of the actuator from the captured oscilloscope image. Table 6-2 shows a comparison of the experimentally extracted resonance frequency with those obtained from two models for a mounted mirror size of 2 mm x 100 μm x 1 mm. The experimental resonance frequency matches the simulated value closely and the calculated value from the analytical model is within 10% of the experimental and simulated results. The small deviation in the analytical model is probably a result of the assumption of a constant truss width in the analytical model.

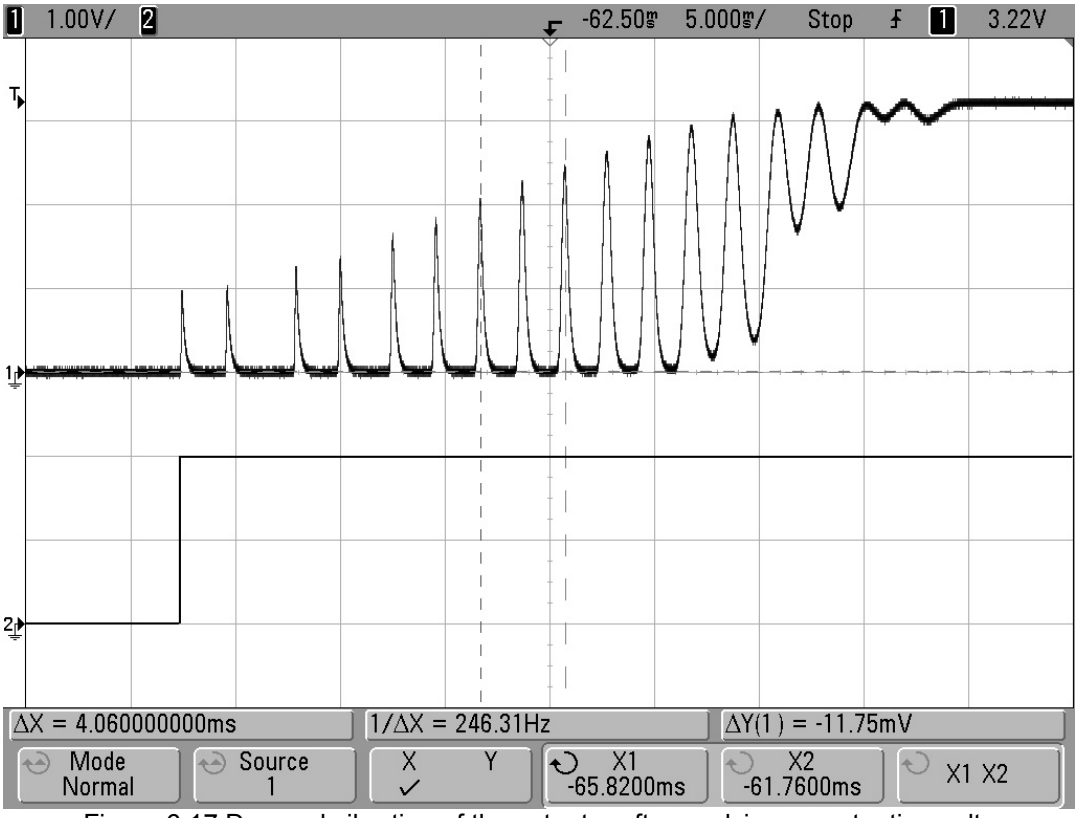

Figure 6.17 Damped vibration of the actuator after applying an actuation voltage.

I also characterized the dynamic response of the actuator within its operational voltage range. I moved the photodetector to a different position corresponding to an applied voltage, and recorded the time from applying the actuation voltage step until the laser beam crossed the detector position. As the displacement of the zipped comb actuator is quite low at lower voltages and the sensitive area of the photodetector is relatively large, measurements below actuation voltages of 30 V were not possible. In Figure 6.18, the results from an actuation voltage step from 0 to 100 V are presented. The vertical axis represents the detector position in terms of the actuation voltage that would result in a laser beam deflection to that position after the actuator vibration is fully damped.

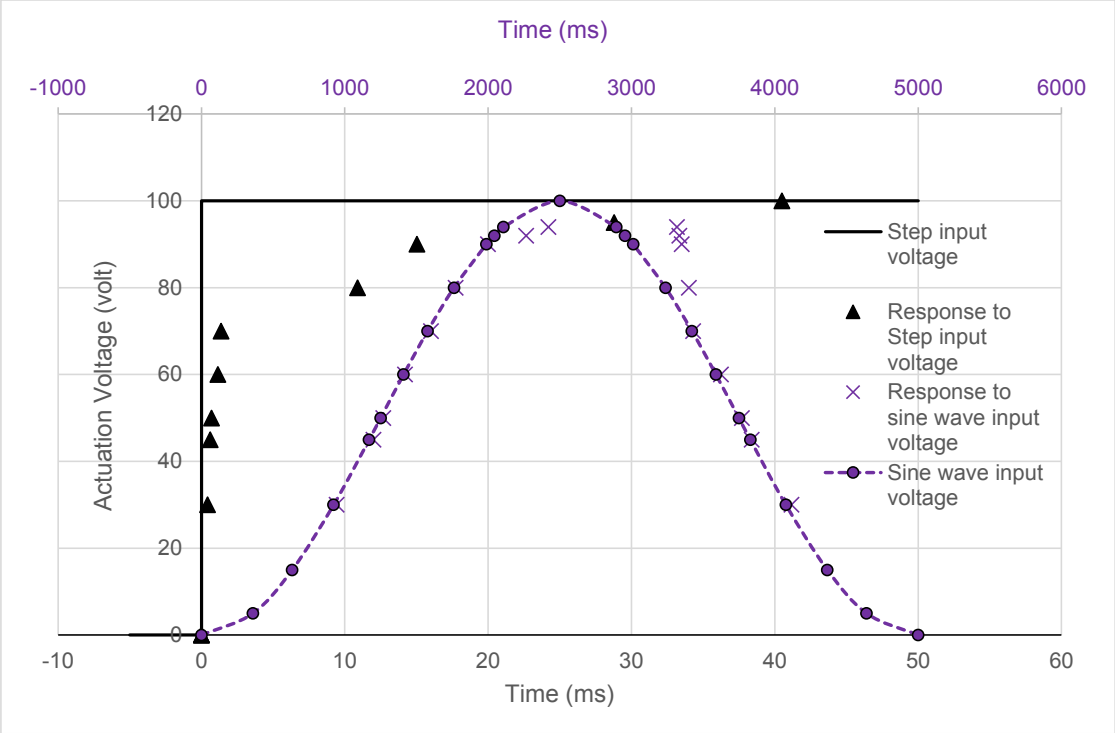

Figure 6.18 Dynamic response of the actuator to different actuation input voltages.

The horizontal axis gives the time at which the laser beam crosses a particular position after actuation. It can be seen that the actuator movement lags behind the actuation voltage. The rise time for the actuator for an actuation voltage step from 0 to 100 V is approximately 40 ms. Possible reasons for delay could be inertia and increased air drag at higher voltages, where the displacement per volt is higher. Also shown in Figure 6.18 is the response of the actuator to a slow (0.2 Hz) sine wave actuation voltage (100 V peak-to-peak). In this case, the actuator does not achieve its nominal rotation angle at the highest voltage. The reasons are unclear; the actuator movement should follow the applied sine wave actuation voltage quite closely, given the 40 ms response time in the case of a 100 V actuation voltage step.

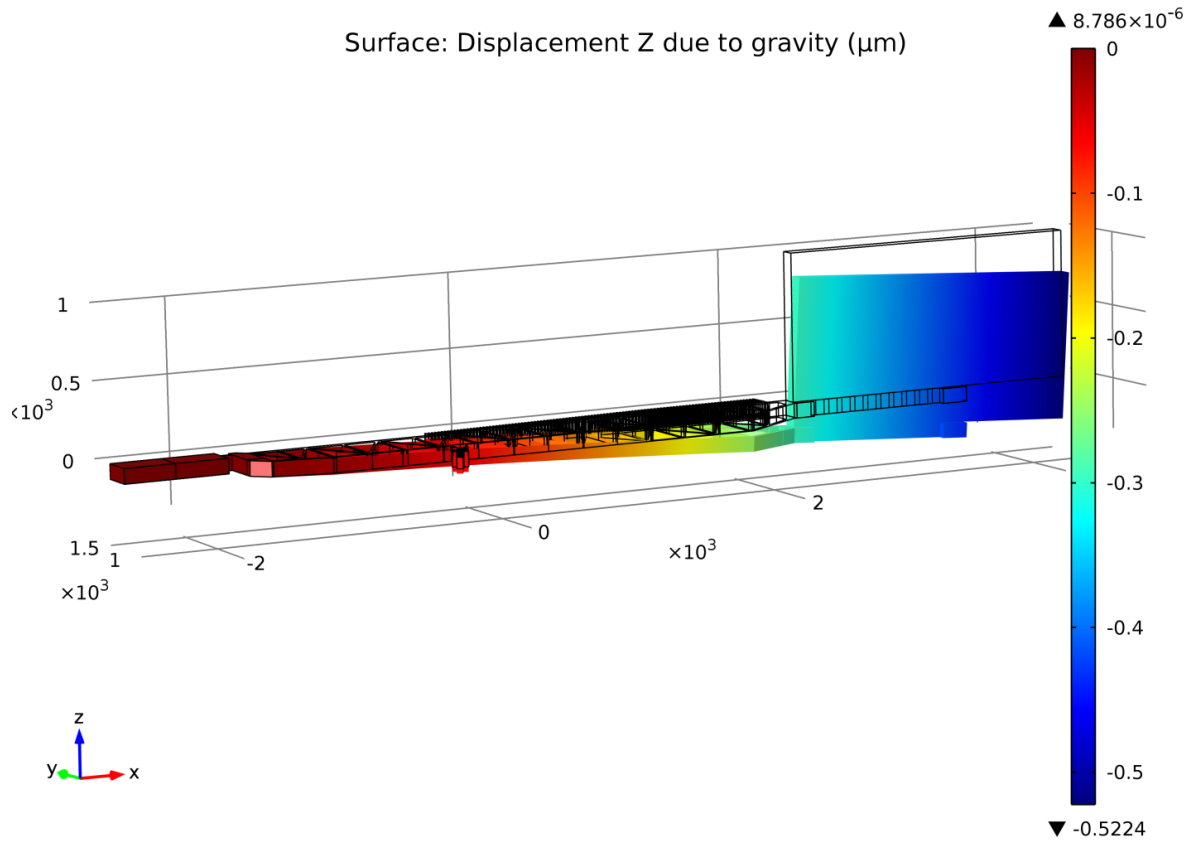

Figure 6.19 Simulated gravitational sag of the actuator with mounted mirror.

6.5.3 Vertical Sag

Due to large size of the mounted mirror, there is a possibility of vertical sag of the actuator in the z-direction. I simulated the long arm actuator with an externally mounted mirror using the multi-physics software COMSOL to characterize the z-directional sag. The simulation (see Figure 6.19) shows that the movable structure gradually bends downwards. It is found that there is a maximum of 200 nm downward sag between moving and fixed comb fingers. The maximum sag of the structure is about 0.5 µm and is located at the very far end of mirror holder, as expected.

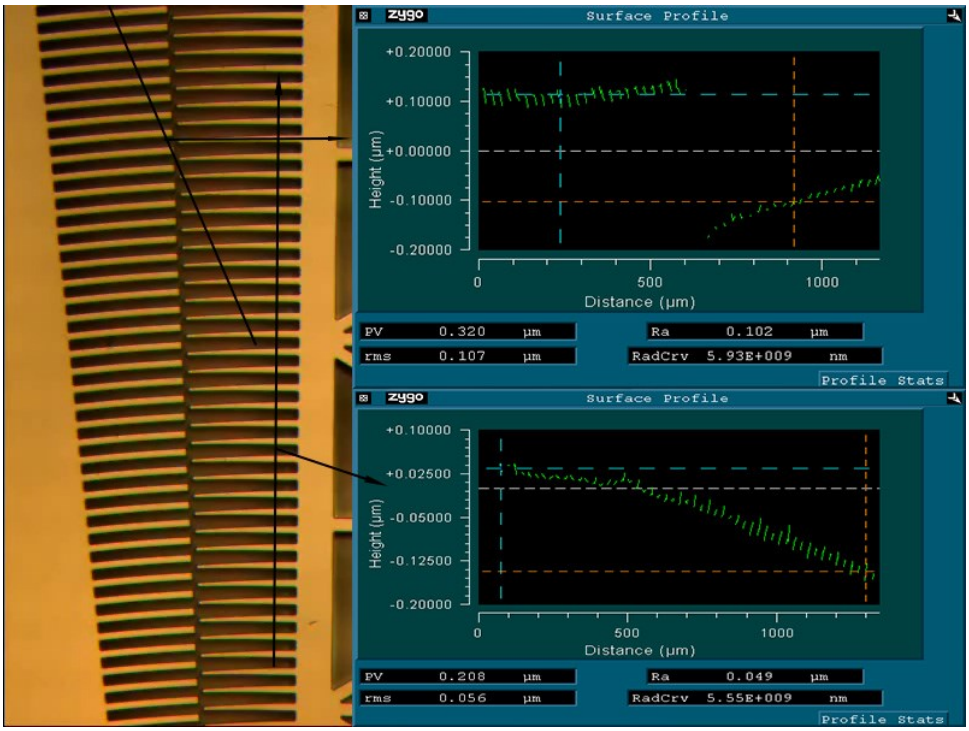

Figure 6.20 Experimentally measured downward sag of the moving structure.

The downward sag of the actuator was also characterized experimentally. I measured the surface level orientation of the actuator after mounting an external mirror using a Zygo optical profilometer, as shown in Figure 6.20. The first surface profile in the figure shows the height difference between the fixed and moving comb fingers. The moving comb fingers farthest from anchor point are found to be approximately 200 nm lower than the fixed structure for an actuator with mounted mirror size of 2 mm x 1 mm x 100 µm, similar to a sag of approximately 190 nm found using simulation. The second surface profile (bottom trace in the figure) shows the gradually increasing sag in the z-direction along the radially outward direction from the anchor point. I did not observe any significant deviation of actuation

behavior of the device due to this vertical sag.

6.6 Summary

In this chapter, a novel MEMS actuator with large externally mounted mirror has been presented in terms of design, modeling, fabrication and experimental validation and characterization. A different type of comb finger arrangement, named zipped comb fingers, was implemented, which provides a slower initial actuation. A novel truss design was implemented to support the 5.4 mm long arm and large movement of the actuator, which was necessary for creating working space for integrating optical components. Detailed analytical modeling of deflection, side instability, and resonance frequency was performed for the designed zipped comb drive actuator. I also presented an efficient method for mounting the mirror which was tested successfully by mounting differently sized mirrors. The mirror mounting method can be robotized for mass production in case of commercialization. Experimental characterization of the fabricated actuators was performed using electrical and optical methods to verify the results from analytical models and FEA simulations. The experimental results are found to be in good agreement with those from the analytical model and the simulations. This actuator can be used, for example, in ECLs and other optical applications which require large mirrors and high quality reflecting surfaces.

7 Conclusions and Future Work

I conclude this thesis with this final chapter by evaluating the designed MEMS actuators in light of the research goal, which is to establish a foundation to build a MEMS based external cavity diode laser with a large tuning range. The merits and demerits of the different comb drive actuators were analyzed based on suitability for implementation in Littman or Littrow configured ECLs and producing an integrated ECL chip. Finally, I point out the direction of the future research in this area.

7.1 Conclusions

In this thesis I described the development of three novel rotary comb actuators to support building MEMS based ECLs in either Littrow or Littman configuration. Chapter 1 gives the motivation for this broad research project, namely to build a mid-infrared ECL for spectroscopic applications. Chapter 2 provides background information about MEMS technology and MEMS actuators, and the literature describing different MEMS actuators for ECLs is reviewed. Chapters 3 to 7 illustrate my contributions through this PhD research toward achieving the broad research goal.

In the third chapter, the design, fabrication, and characterization of rotary comb actuators with resonance frequencies of 1 kHz and above are discussed. A maximum rotational angle of 3 degree was achieved with an applied voltage as low as 100 V which is a quite reasonable voltage for a MEMS device. The devices were fabricated from a SOI wafer with a device layer thickness of 100 μm using a wet release method. The sidewall of the movable arm with a reflecting surface of 2 × 0.1 mm can be used as part of the external cavity in an ECL in Littrow configuration by grooving a grating onto the sidewall. External optical components, such as mirrors, can also be mounted onto the arm of the actuator and can be used to adjust the resonator length in both Littrow and Littman configured ECLs.

Chapter 4 focuses on virtual pivot point actuators, which offer some specific advantages for designing Littman configured ECLs. The virtual pivot point actuator allows in-plane optical ray propagation for ECLs in Littman configuration; the optical ray would be blocked by the movable arm in simple rotary comb actuator. Section 4.2 describes the detailed design and analysis of the virtual pivot point actuator. Several designs were fabricated and a maximum rotation angle of ±1.5 degree at a voltage of 190 V was achieved. Movable arm-tip radii of 4 mm and clearances of up to 2.8 mm from the virtual pivot point to the device structure were achieved in these designs. The design can be modified to increase the maximum radius or clearance from the pivot point. A modification of this VPP design was performed to facilitate mounting of large external mirrors, and devices with mounted mirrors are presented [98]. The sidewalls of the movable arms of the actuator structures are accessible from outside for on-chip integration with different optical applications.

In Chapter 5, I describe two techniques to smooth micro-etched silicon sidewalls. In the first developed method, controlled over-passivation of the sidewall during etching with the Bosch process was used. The rms roughness of the etched sidewall using this recipe was 3.89 nm. The maximum achievable depth of a smooth sidewall using the over-passivated recipe is approximately 120 μm. The second technique to smooth the sidewall was developed from well-known oxidation techniques. Temperature and time of the oxidation process were carefully chosen and a two-cycle oxidation + BOE process was used to obtain optical quality smooth sidewalls. The rms roughness of the sidewall post-processed by the two-step oxidation + BOE technique was found to be 2.56 nm. One major advantage of the two-step oxidation + BOE technique is that the depth limit for the optically smooth sidewall is determined by the uniformly etched depth and profile verticality of the structure, not by any limitation of the smoothing process.

In Chapter 6, I present a MEMS actuator with long arm and large externally mounted mirror. The detailed design, analytical modeling and fabrication technique are described. It was found that a comb drive with zipped comb fingers provides a slower initial actuation. A rotation angle of 3 degree was achieved for an applied voltage of 130 V. A method was also demonstrated to mount an external mirror efficiently, which was tested successfully by mounting mirrors of different sizes. The experimental characterization of the fabricated actuators was performed using electrical and optical methods. The optical characterization showed a transient vibration of the actuator with mounted mirror after application of an actuation voltage step. This actuator can be used for optical applications which require large mirrors and high quality reflecting surfaces, for example, external cavity lasers.

In conclusion, the research presented in this PhD thesis provides a strong foundation to produce MEMS based mid infrared external cavity diode lasers with a large tuning range. All of the three designed actuators provide a rotation angle of about 3° which is sufficient to tune over wavelength range of about 100 nm. Since these designs support Littman, Littrow or both configurations and provide reflecting surfaces of various sizes, the actuators can be selected based on laser beam size and availability of other optical components. The optical quality of the sidewall surface could be improved with newly developed smoothing techniques so that they can be used as optical reflectors. Together with the developed smoothing technology, the actuators provide a stepping stone for building ECLs in a completely integrated way in which all of components are fabricated from silicon or in a hybrid approach.

7.2 Future Work

An extended objective beyond this project is to build a complete, on-chip integrated hybrid ECL. The current effort can be extended to fabricate silicon based optical components such as lenses and gratings, which are necessary to build ECLs. Semiconductor diode lasers usually need two cylindrical lenses to collimate the laser beam properly because of the different amounts of divergence of its fast and slow axis. One of the lenses can be fabricated simultaneously with the fabrication of the actuator. Another lens needs to be fabricated externally due to lack of suitable technology of fabricating an aspherical lens structure vertically. The lens can be integrated during integration of the laser diode into the actuator chip. The surface quality of these optical components can be improved to the level achievable with the sidewall smoothing techniques developed in this thesis.

In this thesis, I described two techniques for smoothing of silicon sidewalls, which resulted in sidewalls of 100 –120 μm depth. The research can be further extended to fabricate integrated optical quality mirrors up to wafer thickness. The design and fabrication method for the actuators can be modified to extend the mirror down to the handle layer. One of the major advantages of fabricating an integrated mirror in this way is that mirrors can be made very thin, thus increasing the resonance frequency of the actuator and therefore also the stability of the device. The two step oxidation + BOE sidewall smoothing technique can be used to obtain optical quality integrated mirrors. Additional processing issues, such as the profile angle of the mirror, uniformity across etch depth etc., may need to be resolved to fabricate larger integrated mirrors.

The actuators developed in this thesis provide an angular rotation of around 3°, equivalent to a lateral stroke in the range of 80–280 μm based on the length of moving arm. Although primarily developed for use in ECLs, these actuators can readily be used in other applications that require large rotation or large lateral stroke such as optical scanner, tunable optical filter, tunable phase shifter, optical attenuators, interferometer, optical tomography, etc. The large stroke and high resonance frequency of the actuators and the large size of the mirror can provide additional benefits for those systems.

References

[1] A. Kosterev, G. Wysocki, Y. Bakhirkin, S. So, R. Lewicki, M. Fraser, F. Tittel and R. Curl, "Application of quantum cascade lasers to trace gas analysis," *Appl. Phy. B* **90**, 165-176 (2008).

[2] F. K. Tittel, D. Richter and A. Fried, "Mid-infrared laser applications in spectroscopy," *Solid-State Mid-Infrared Laser Sources.* Springer Berlin Heidelberg, 458-529 (2003).

[3] B. Brunekreef and S. T. Holgate, "Air pollution and health," *The Lancet* **360**, 1233-1242 (2002).

[4] J. H. Schulte, "Effects of mild carbon monoxide intoxication," *Archives of Environmental Health: An International Journal* **7**(5), 524-530 (1963).

[5] U. Pöschl, "Atmospheric aerosols: Composition, transformation, climate and health effects," *Angew. Chem. Int. Ed.* **44**, 7520-7540 (2005).

[6] I. Tsujino, M. Nishimura, A. Kamachi, H. Makita, M. Munakata, K. Miyamoto and Y. Kawakami, "Exhaled nitric oxide–Is it really a good marker of airway inflammation in bronchial asthma?" *Respiration* **67**, 645-651 (2000).

[7] C. Shimamoto, I. Hirata and K. Katsu, "Breath and blood ammonia in liver cirrhosis," *Hepato-gastroenterology,* vol. **47(32)**, 443-445 (2000).

[8] M. R. McCurdy, Y. Bakhirkin, G. Wysocki, R. Lewicki and F. K. Tittel, "Recent advances of laser-spectroscopy-based techniques for applications in breath analysis," *J. of Breath Res.* **1**, 014001 (2007).

[9] C. R. Webster, G. J. Flesch, K. Mansour, R. Haberle and J. Bauman, "Mars laser hygrometer," *Appl. Opt.* **43**, 4436-4445 (2004).

[10] R. Hall, G. Fenner, J. Kingsley, T. Soltys and R. Carlson, "Coherent Light Emission from Ga-As Junctions," *Phys. Rev. Lett.* **9**, 366 (1962).

[11] M. I. Nathan, W. P. Dumke, G. Burns, F. H. Dill and G. Lasher, "Stimulated Emission of Radiation From GaAs p-n Junctions," *Appl. Phys. Lett.* **1**, 62-64 (1962).

[12] A. Q. Liu, X. M. Zhang and D. Y. Tang, "MEMS widely tunable lasers for WDM system applications," *Proc. of SPIE **4907**,* 186-194 (2002).

[13] X. M. Zhang, A. Q. Liu, V. M. Murukeshan and F. Chollet, "Integrated micromachined tunable lasers for all optical network (AON) applications," *Sens. and Actuators A* **97**(8), 54-60 (2002).

[14] M. G. Littman and H. J. Metcalf, "Spectrally narrow pulsed dye laser without beam expander," *Appl. Opt.* **17**, 2224-2227 (1978).

[15] M. C. Wu, A. Solgaard and J. E. Ford, "Optical MEMS for lightwave communication," *J. Lightwave Technol.* **24**, 4433-4454 (2006).

[16] H. Nathansan and R. Wickstrom, "Microelectronic frequency selective apparatus with vibratory member and means responsive thereto," US Patent No. **3413573** (1968).

[17] N. Yazdi, F. Ayazi and K. Najafi, "Micromachined inertial sensors," *Proc. IEEE* **86**(8), 1640-1659 (1998).

[18] F. E. Tay, *Microfluidics and BioMEMS Applications.* Kluwer Academic Publishers, (2002).

[19] H. J. d. l. Santos, *Introduction to Microelectromechanical Microwave Systems.* Artech House, (2004).

[20] K. Petersen, "Micromechanical light modulator array fabricated on silicon," *Appl. Phys. Lett.* **31**, 521-523 (1977).

[21] K. E. Petersen, "Silicon Torsional Scanning Mirror," *IBM J. of Res. Dev.* **24**, 631-637(1980).

[22] P. F. van Kessel, L. J. Hornbeck, R. E. Meier and M. R. Douglass, "A MEMS-based projection display," *Proc. of the IEEE* **86**, 1687-1704 (1998).

[23] M. A. Basha, N. Dechev, S. Safavi-Naeini and S. K. Chaudhuri, "A Scalable Optical MEMS Switch Architecture Utilizing a Microassembled Rotating Micromirror," *IEEE J. Sel. Top. Quantum Electron.* **13**, 336-347 (2007).

[24] S. P. Beeby, M. J. Tudor and N. White, "Energy harvesting vibration sources for microsystems applications," *Meas. Sci. Tech.* **17**, R175 (2006).

[25] B. Yang, C. Lee, R. K. Kotlanka, J. Xie and S. P. Lim, "A MEMS rotary comb mechanism for harvesting the kinetic energy of planar vibrations," *J Micromech. Microeng.* **20**, 065017 (2010).

[26] H. Fujita, "Microactuators and micromachines," *Proc. IEEE* **86**, 1721-1732 (1998).

[27] E. Thielicke and E. Obermeier, "Microactuators and their technologies," *Mechatronics,* **10**(4), 431-455 (2000).

[28] N. Maluf and K. Williams, *An Introduction to Microelectromechanical Systems Engineering. 2nd Ed.* Artech House, (2004).

[29] C. A. Rich and K. D. Wise, "A high-flow thermopneumatic microvalve with improved efficiency and integrated state sensing," J. *Microelectromech. Syst.* **12**, 201-208 (2003).

[30] H. Miyajima, N. Asaoka, T. Isokawa, M. Ogata, Y. Aoki, M. Imai, O. Fujimori, M. Katashiro and K. Matsumoto, "A MEMS electromagnetic optical scanner for a commercial confocal laser scanning microscope," J. *Microelectromech. Syst.* **12**, 243-251 (2003).

[31] D. Maillefer, H. van Lintel, G. Rey-Mermet and R. Hirschi, "A high-performance silicon micropump for an implantable drug delivery system," 12th IEEE Int. Conf. on *Micro Electro Mech. Syst.,* 541-546 (1999).

[32] W. L. Benard, H. Kahn, A. H. Heuer and M. A. Huff, "Thin-film shape-memory alloy actuated micropumps," J. *Microelectromech. Syst.* **7**, 245-251 (1998).

[33] S. F. Bart, T. A. Lober, R. T. Howe, J. H. Lang and M. F. Schlecht, "Design considerations for micromachined electric actuators," *Sensors and Actuators* **14**(3), 269-292 (1988).

[34] W. C. Tang, Electrostatic comb drive for resonant sensor and actuator applications, Diss. *University of California, Berkeley,* (1990).

[35] Y. Li, D. Psychogiou, S. Kuhne, J. Hesselbarth, C. Hafner and C. Hierold, "Large Stroke Staggered Vertical Comb-Drive Actuator for the Application of a Millimeter-Wave Tunable Phase Shifter," J. *Microelectromech. Syst.* **22**, 962-975 (2013).

[36] D. Hah, P. R. Patterson, H. D. Nguyen, H. Toshiyoshi and M. C. Wu, "Theory and experiments of angular vertical comb-drive actuators for scanning micromirrors," *IEEE J. Sel. Top. Quantum Electron.* **10**, 505-513 (2004).

[37] W. Trutna Jr and L. F. Stokes, "Continuously tuned external cavity semiconductor laser," J. *Lightwave Technol.* **11**, 1279-1286 (1993).

[38] Petermann K, *Laser Diode Modulation and Noise.* London: Kluwer, (1988).

[39] W. M. Wang, K. T. V. Grattan, A. W. Palmer and W. J. O. Boyle, "Self-mixing interference inside a single-mode diode laser for optical sensing applications," J. *Lightwave Technol.* **12**, 1577-1587 (1994).

[40] A. Q. Liu and X. M. Zhang, "A review of MEMS external-cavity tunable lasers," *J Micromech. Microeng.* **17**(1), R1-R13 (2007).

[41] A. Liu, X. Zhang, V. Murukeshan, C. Lu and T. Cheng, "Micromachined wavelength tunable laser with an extended feedback model," *IEEE J. Sel. Top. Quantum Electron.* **8**, 73-79 (2002).

[42] Q. Chen, G. D. Cole, E. Bjorlin, T. Kimura, S. Wu, C. S. Wang, N. C. MacDonald and J. E. Bowers, "First demonstration of a MEMS tunable vertical-cavity SOA," IEEE *Photonics Technol. Lett.* **16**, 1438-1440 (2004).

[43] Y. Li, W. Yuen, G. Li and C. Chang-Hasnain, "Top-emitting micromechanical VCSEL with a 31.6-nm tuning range," IEEE *Photonics Technol. Lett.* **10**, 18-20 (1998).

[44] C. J. Chang-Hasnain, "Tunable VCSEL," *IEEE J. Sel. Top. Quantum Electron.* **6**, 978-987 (2000).

[45] B. Pezeshki, E. Vail, J. Kubicky, G. Yoffe, S. Zou, J. Heanue, P. Epp, S. Rishton, D. Ton and B. Faraji, "20-mW widely tunable laser module using DFB array and MEMS selection," IEEE *Photonics Technol. Lett.* **14**, 1457-1459 (2002).

[46] Y. Uenishi, K. Honma and S. Nagaoka, "Tunable laser diode using a nickel micromachined external mirror," *Electron. Lett.* **32**, 1207-1208 (1996).

[47] A. Liu, H. Cai, X. Zhang and J. Tamil, "A review of different types of photonics MEMS tunable lasers," *Proc. SPIE **6836**,* 683602 (2007).

[48] A. Q. Liu, X. M. Zhang, D. Y. Tang and C. Lu, "Tunable laser using micromachined grating with continuous wavelength tuning," *Appl. Phys. Lett.* **85**, 3684-3686 (2004).

[49] W. Huang, R. Syms, J. Stagg and A. Lohmann, "Precision MEMS flexure mount for a Littman tunable external cavity laser," *IEE Proc. Science, Measurement and Technology,* **151**, 67-75 (2004).

[50] J. D. Berger, Y. Zhang, J. D. Grade, H. Lee, S. Hrinya, H. Jerman, A. Fennema, A. Tselikov and D. Anthon, "Widely tunable external cavity diode laser using a MEMS electrostatic rotary actuator," *Proc. 27th Eur. Conf. on Opt. Comm (ECOC)*, 198-199 (2001)

[51] Y. Lee, M. Toda, M. Esashi and T. Ono, "Miniature wishbone interferometer using rotary comb drive actuator for environment gas monitoring," 24th IEEE Int. Con. on *Micro Electro Mechanical Systems (MEMS),* 716-719 (2011).

[52] M. T. Hou, J. Huang, S. Jiang and J. A. Yeh, "In-plane rotary comb-drive actuator for a variable optical attenuator," *J. Micro/Nanolith. MEMS MOEMS* **7**, 043015 (2008).

[53] J. A. Yeh , C. Chen and Y. Lui, "Large rotation actuated by in-plane rotary comb-drives with serpentine spring suspension," *J Micromech. Microeng.* **15**, 201-206 (2005).

[54] A. Kassimali, Structural Analysis. Cengage Learning, (2010).

[55] K. Chen, A. A. Ayón, X. Zhang and S. M. Spearing, "Effect of process parameters on the surface morphology and mechanical performance of silicon structures after deep reactive ion etching (DRIE)," J. *Microelectromech. Syst.* **11**, 264-275 (2002).

[56] B. Wu, A. Kumar and S. Pamarthy, "High aspect ratio silicon etch: A review," *J. Appl. Phys.,* **108,** 051101 (2010).

[57] W. Juan and S. Pang, "Controlling sidewall smoothness for micromachined Si mirrors and lenses," *J. of Vacuum Science & Technology B: Microelectronics and Nanometer Structures* **14**, 4080-4084 (1996).

[58] T. M. F. Amin, M. Q. Huda, J. Tulip and W. Jager, "Sidewall roughness control in deep reactive ion etch process for micromachined Si devices," 7th Int. Conf. on *Electrical and Computer Engineering (ICECE),* 82-85 (2012).

[59] Intellisense, Intellisuite **8.2**, http://www.intellisense.com/.

[60] M. Q. Huda, "Personal Communication".

[61] M. Q. Huda, T. M. F. Amin, Y. Ning, G. McKinnon, J. Tulip and W. Jäger, "Rotary microelectromechanical system comb-drive actuator with smooth sidewall for photonic applications," *J. of Micro/Nanolithography, MEMS, and MOEMS* **11**(2), 023012-1 (2012).

[62] X. Zhang, A. Liu, C. Lu and D. Tang, "Continuous wavelength tuning in micromachined Littrow external-cavity lasers," IEEE J. *Quantum Electron.* **41**, 187-197 (2005).

[63] J. D. Berger, Y. Zhang, J. D. Grade, H. Lee, S. Hrinya and H. Jerman, "Widely tunable external cavity diode laser based on a MEMS electrostatic rotary actuator," *Optical Fiber Communication (OFC) Conference and Exhibit **2**,* TuJ2 1-3 (2001).

[64] J. H. Jerman and J. D. Grade, "Balanced Microdevice," U.S. Patent No. 6903486, (2005).

[65] X. M. Zhang, A. Q. Liu, C. Lu and D. Y. Tang, "A Real Pivot Structure for MEMS Tunable Lasers," J. *Microelectromech. Syst.* **16**, 269-278 (2007).

[66] K. E. Petersen, "Silicon as a mechanical material," *IEEE Proc.* **70**, 420-457 (1982).

[67] K. Sooriakumar, W. Chan, T. S. Savage and C. Fugate, "A comparative study of wet vs. dry isotropic etch to strengthen silicon micro-machined pressure sensor," *Electrocheml. Soc. Proc.* **27**, 259-265 (1995).

[68] F. Lärmer and A. Schilp, "Method of Anisotropically Etching Silicon," U.S. Patent No. 5501893 A, (1996).

[69] S. Sinzinger and J. Jahns, *Microoptics.* Wiley Online Library, (2005).

[70] S. Yun, S. You and J. Lee, "Fabrication of vertical optical plane using DRIE and KOH crystalline etching of (110) silicon wafer," *Sens. Actuators, A.* **128**, 387-394 (2006).

[71] D. Nilsson, S. Jensen and A. Menon, "Fabrication of silicon molds for polymer optics," *J Micromech. Microeng.* **13(4)**, S57 (2003).

[72] H. Liu, Y. Lin and W. Hsu, "Sidewall roughness control in advanced silicon etch process," *Microsyst. Technol.* **10**, 29-34 (2003).

[73] M. Chabloz, Y. Sakai, T. Matsuura and K. Tsutsumi, "Improvement of sidewall roughness in deep silicon etching," *Microsyst. Technol.* **6**, 86-89 (2000).

[74] I. Song, Y. Peter and M. Meunier, "Smoothing dry-etched microstructure sidewalls using focused ion beam milling for optical applications," *J Micromech Microeng.* **17(8)**, 1593 (2007).

[75] M. Lee and M. C. Wu, "Thermal annealing in hydrogen for 3-D profile transformation on silicon-on-insulator and sidewall roughness reduction," J. *Microelectromech. Syst.* **15**, 338-343 (2006).

[76] K. K. Lee, D. R. Lim, L. C. Kimerling, J. Shin and F. Cerrina, "Fabrication of ultralow-loss Si/SiO_2 waveguides by roughness reduction," *Opt. Lett.* **26**, 1888-1890 (2001).

[77] W. Pike, W. Karl, S. Kumar, S. Vijendran and T. Semple, "Analysis of sidewall quality in through-wafer deep reactive-ion etching," *Microelectron. Eng.* **73**, 340-345 (2004).

[78] B. E. Deal and A. Grove, "General relationship for the thermal oxidation of silicon," *J. Appl. Phys.* **36**, 3770-3778 (2004).

[79] R. Marcus and T. Sheng, "The oxidation of shaped silicon surfaces," *J. Electrochem. Soc.* **129**, 1278-1282 (1982).

[80] D. Kao, J. P. McVittie, W. D. Nix and K. C. Saraswat, "Two-dimensional thermal oxidation of silicon. II. Modeling stress effects in wet oxides," *IEEE Trans. Electron Devices* **35**, 25-37 (1988).

[81] D. Kao, J. P. McVittie, W. D. Nix and K. C. Saraswat, "Two-dimensional thermal oxidation of silicon—I. Experiments," *IEEE Trans. Electron Devices* **34**, 1008-1017 (1987).

[82] Y. Uenishi, K. Honma and S. Nagaoka, "Tunable laser diode using a nickel micromachined external mirror," *Electron. Lett.* **32**, 1207-1208 (1996).

[83] T. Amin, M. Huda, Y. Ning, G. McKinnon, J. Tulip and W. Jäger, "A virtual pivot point MEMS rotary comb actuator for tunable laser applications," Proc. SPIE **8490**, 84900D (2012).

[84] L. Ferreira and S. Moehlecke, "A silicon micromechanical galvanometric scanner," *Sens. Actuators, A* **73**, 252-260 (1999).

[85] P. Lin, H. Hsieh and G. J. Su, "Design and fabrication of a large-stroke MEMS deformable mirror for wavefront control," *J. Opt.* **13**, 055404 (2011).

[86] Y. Liu, J. Xu, S. Zhong and Y. Wu, "Large size MEMS scanning mirror with vertical comb drive for tunable optical filter," *Opt. Lasers Eng. 51(1), 54-60 (*2013).

[87] B. Qi, A. Phillip Himmer, L. Maggie Gordon, X. Victor Yang, L. David Dickensheets and I. Alex Vitkin, "Dynamic focus control in high-speed optical coherence tomography based on a microelectromechanical mirror," Opt. Commun., vol. 232, pp. 123-128, 2004.

[88] Y. Pan, H. Xie and G. K. Fedder, "Endoscopic optical coherence tomography based on a microelectromechanical mirror," Opt. Lett., vol. 26, pp. 1966-1968, 2001.

[89] M. Q. Huda, T. M. F. Amin, Y. Ning, G. McKinnon, J. Tulip and W. Jäger, "Fabrication of thin vertical mirrors through plasma etch and KOH: IPA polishing for integration into MEMS electrostatic actuators," Proc. SPIE 8612, 86120D (2013).

[90] T. Amin, M. Huda, J. Tulip and W. Jager, "Sidewall roughness control in deep reactive ion etch process for micromachined Si devices," 7th Int. Conf. on *Electrical and Computer Engineering (ICECE),* 82-85 (2012).

[91] F. C. Martinez, N. Chen, M. Waslik and A. P. Pisano, "Optimized ultra-DRIE for the MEMS rotary engine power system," *European Micro and Nano Systems Conference,* 13-17 (2004).

[92] J. Li, "Electrostatic zipping actuators and their applications to MEMS," PhD Diss. *Massachusetts Institute of Technology,* (2004).

[93] W. C. Wong, I. A. Azid and B. Yeop Majlis, "Theoretical Analysis of Stiffness Constant and Effective Mass for a Round-Folded Beam in MEMS Accelerometer," *Strojniški Vestnik-Journal of Mechanical Engineering* **57**, 517-525 (2011).

[94] M. Huda, T. Amin, Y. Ning, G. McKinnon, J. Tulip and W. Jäger, "Rotary MEMS comb-drive actuator with large deflection for photonic applications," Proc. *SPIE MOEMS-MEMS **8248**,* 824804 (2012).

[95] Epotek Epoxy Technology*,* http://www.epotek.com/.

[96] X. Zhang and W. C. Tang, "Viscous air damping in laterally driven microresonators," Proc. IEEE *Workshop on Micro Electro Mechanical Systems,* 199-204 (1994).

[97] Y. Cho, A. P. Pisano and R. T. Howe, "Viscous damping model for laterally oscillating microstructures," J. *Microelectromech. Syst.* **3**, 81-87 (1994).

[98] T. M. F. Amin, M. Q. Huda, J. Tulip and W. Jäger, "A virtual pivot point MEMS rotary comb actuator with externally mounted mirror for optical applications," Technical proc. of *NSTI-Nanotech* 2014, **2**, 17-20 (2014).

Appendices

Appendix A: Displacement of a Simple Rotary Comb Actuator

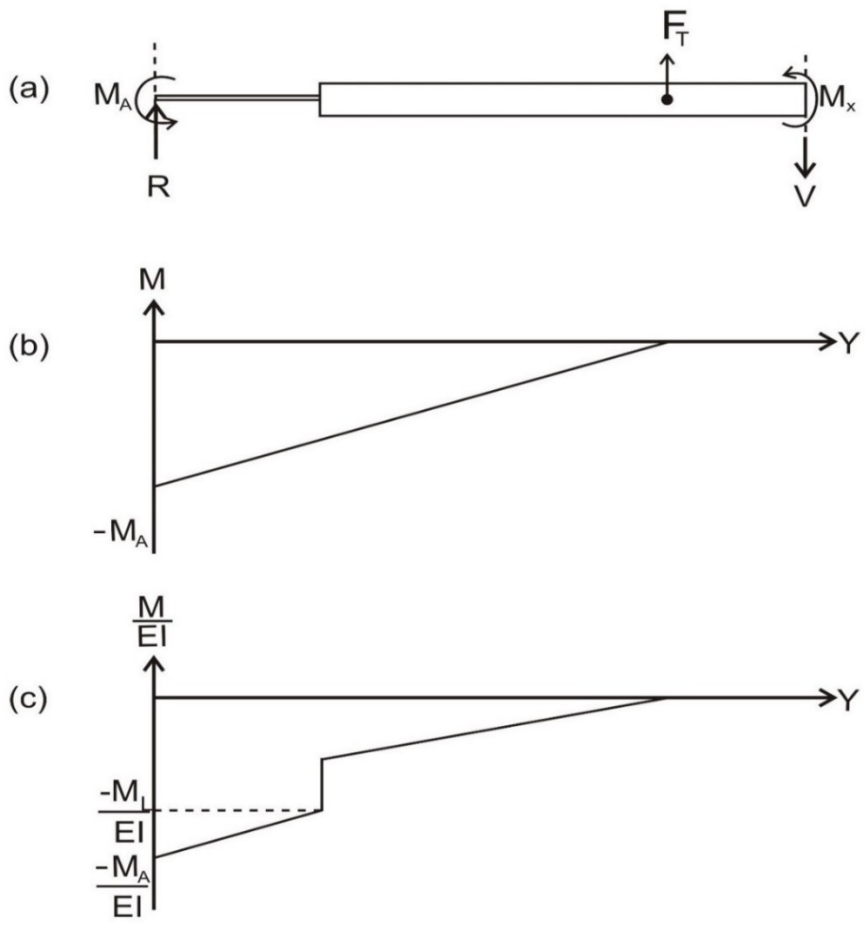

Figure A1: (a) Free body diagram of the point force model of the rotary comb actuator; (b) bending moment diagram of the point force equivalent model; (c) moment diagram normalized with respect to the area moment of inertia of the beam.

From the free body diagram, the summation over all vertical forces is zero at equilibrium condition:

$$\sum F_y = 0 \quad => \; R - F_T = 0 \;\; => R = F_T$$

Here, *R* is the reaction force at the anchor and F_T is the total force from all the comb fingers.

Taking the moment with respect to the anchor point, one obtains:

$$\sum M = 0 \quad => \; M_A - F_T(L + L_F) = 0 \;\; => M_A = F_T(L + L_F)$$

Here, M_A is the acting moment at the anchor point due to the applied force F_T, L is the length of the beam and L_F is the distance between the beam tip and the position where the force is applied to the truss.

Again, taking the moment just before the right end (at a distance x from anchor point) of the structure, one obtains:

$$\sum M = 0 \quad => \; M_A - R.x + F_T(x - L - L_F) + M_x = 0$$

$$=> M_x = -M_A + R.x - F_T(x - L - L_F)$$

$$where\ F_T(x - L - L_F) = 0\ for\ x \leq (L + L_F)$$

Here, M_x is the moment at distance x from the anchor point.

According to the moment area method, the displacement at any point of the structure can be determined by taking the moment of the area (only of the area to the left of that point) under the M/EI diagram with respect to the point. Thus the maximum displacement is at the farthest position from anchor point and can be determined accordingly:

$$x = \frac{1}{EI}\left[\frac{1}{2}L.(M_A - M_L).\left(\frac{2}{3}L + L_F + L_x\right) + L.M_L.\left(\frac{L}{2} + L_F + L_x\right) + \frac{1}{2Y}L_F.M_L.\left(\frac{2}{3}L_F + L_x\right)\right]$$

$$= \frac{F_T}{3EI}\left[\frac{3L^2}{2}.\left(\frac{2}{3}L + L_F + L_x\right) + 3L.L_F.\left(\frac{L}{2} + L_F + L_x\right) + \frac{3}{2Y}L_F.L_F.\left(\frac{2}{3}L_F + L_x\right)\right]$$

$$= \frac{N\varepsilon hV^2L^3}{3E.\frac{1}{12}w^3h}\left[\left(1 + \frac{L_F}{\frac{2}{3}L} + \frac{L_x}{\frac{2}{3}L}\right) + \left(\frac{L_F}{\frac{2}{3}L} + \frac{L_F^2}{\frac{L^2}{3}}\right) + \frac{1}{Y}\left(\frac{L_F^3}{L^3} + \frac{L_F^2L_x}{\frac{2L^3}{3}}\right)\right]$$

$$= \frac{4N\varepsilon V^2L^3}{Ew^3}\left[1 + \frac{L_F}{\frac{L}{3}} + \frac{L_x}{\frac{2}{3}L} + \frac{L_F^2}{\frac{L^2}{3}} + \frac{L_FL_x}{\frac{L^2}{3}} + \frac{L_F^2L_x}{\frac{2}{3}YL^3} + \frac{L_F^3}{YL^3}\right]$$

Here, M_L=M_A-$F.L_F$ is the bending moment at a distance L from the anchor point, L_x is the distance between the force position and the end of the actuator, Y is the ratio of area moment of inertia between the truss and the beam.

Appendix B: Spring Constant of the Long Arm Actuator

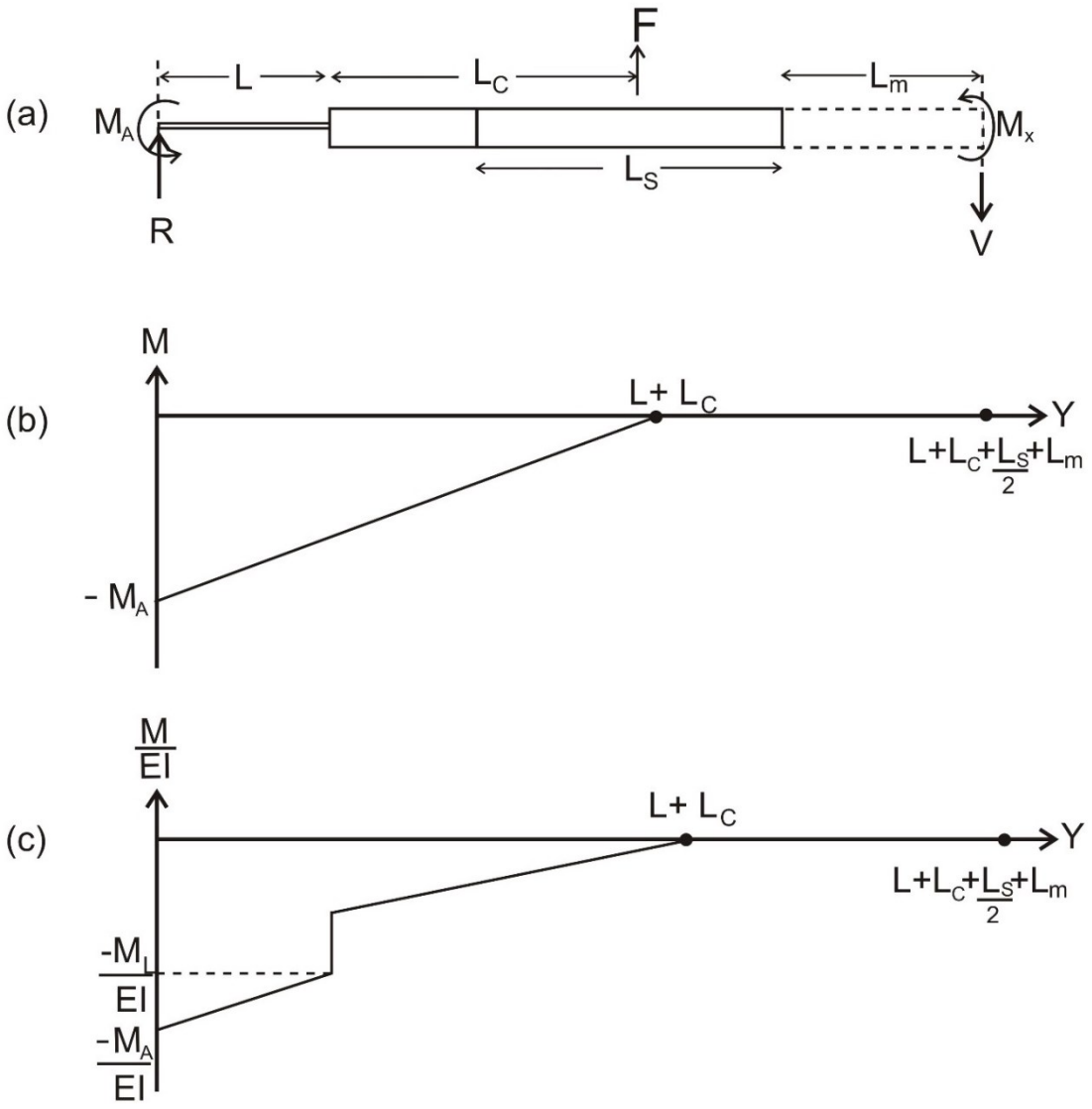

Figure A2: (a) Free body diagram of the point force model of long arm comb drive actuator; (b) bending moment diagram of the point force equivalent model; (c) moment diagram normalized with respect to the area moment of inertia of the beam.

From the free body diagram, the summation over all vertical forces is zero at equilibrium condition:

$$\sum F_y = 0 \quad => R - F = 0 \quad => R = F$$

Here, *R* is the reaction force at the anchor and F is the total force from all the comb fingers.

Taking moment with respect to the anchor point, one obtains:

$$\sum M = 0 \quad => M_A - F(L + L_C) = 0 \quad => M_A = F(L + L_C)$$

Here, M_A is the acting moment at the anchor point due to the applied force F, L is the length of the beam and L_C is the distance between the beam tip and the position where the force is applied to the truss.

Again taking the moment just before the right end (at a distance x from the anchor point) of the mirror holder, one obtains:

$$\sum M = 0 \quad => M_A - R.x + F(x - L - L_C) + M_x = 0$$

$$=> M_x = -M_A + R.x - F(x - L - L_C)$$

$$where\ F(x - L - L_C) = 0\ for\ x \leq (L + L_C)$$

Here, M_x is the moment at a distance x from the anchor point.

According to the moment area method, the displacement at any point of the structure can be determined by taking the moment of the area (only of the area to the left of that point) under the M/EI diagram with respect to the point. Thus the maximum displacement is at the farthest position from anchor point and can be determined accordingly:

$$x = \frac{1}{EI}\left[\frac{1}{2}L.(M_A - M_L).\left(\frac{2}{3}L + L_C + \frac{L_s}{2} + L_m\right) + L.M_L.\left(\frac{L}{2} + L_C + \frac{L_s}{2} + L_m\right)\right.$$
$$\left. + \frac{1}{2Y}L_F.M_L.\left(\frac{2}{3}L_c + \frac{L_s}{2} + L_x\right)\right]$$
$$= \frac{1}{3EI}\left[\frac{3L.FL}{2}.\left(\frac{2}{3}L + L_C + \frac{L_s}{2} + L_x\right) + 3L.FL_C.\left(\frac{L}{2} + L_F + \frac{L_s}{2} + L_m\right)\right.$$
$$\left. + \frac{3}{2Y}L_F.FL_C.\left(\frac{2}{3}L_F + \frac{L_s}{2} + L_m\right)\right]$$
$$= \frac{FL^3}{3EI}\left[1 + \frac{3L_c}{L} + \frac{3L_s}{4L} + \frac{3L_m}{2L} + \frac{3{L_c}^2}{L^2} + \frac{3L_cL_s}{2L^2} + \frac{3L_cL_m}{L^2} + \frac{{L_c}^3}{YL^3} + \frac{3{L_c}^2L_s}{4YL^3} + \frac{3{L_c}^2L_m}{2YL^3}\right]$$

Here M_L=M_A-$F.L_C$ is the bending moment at a distance L from the anchor point, L_S is the comb span length, L_m is the mirror holder length, and Y is the ratio of the area moment inertia of the truss and the beam.

They spring constant of a structure is given by Hooke's Law:

$$F = k.x$$

Therefore, the overall spring constant of the long arm actuator in the x-direction is found as:

$$K_x = \frac{3EI}{L^3}\left(1 + \frac{3L_c}{L} + \frac{3L_s}{4L} + \frac{3L_m}{2L} + \frac{3{L_c}^2}{L^2} + \frac{3L_cL_s}{2L^2} + \frac{3L_cL_m}{L^2} + \frac{{L_c}^3}{YL^3} + \frac{3{L_c}^2L_s}{4YL^3} + \frac{3{L_c}^2L_m}{2YL^3}\right)$$

Appendix C: Effective Mass of Different Sections of the Long Arm Actuator

The effective mass of the actuator was determined by Rayleigh's principle. If a beam has a cross sectional area A, length L and the displacement at any point is given by δ(x), the effective mass according to Rayleigh's principle can be given by:

$$m_e = \rho \int_0^L \left(\frac{\delta(x)}{\delta_{max}}\right)^2 A(x)dx$$

Here, ρ is the density of material. The effective mass of the designed actuator can be derived separately for different sections from the point force model shown in Figure 6.6. The displacement of the structure at different sections can be calculated by a similar process used in Appendix A with the moment area method.

A. Beam:

The displacement at a point x along the beam is given by:

$$b(x) = \frac{F}{6EI}[(3L + 3L_c)x^2 - x^3]$$

The maximum displacement of the beam is at the tip and is provided by Equation 6.6. The effective mass of beam is given by:

$$m_b = \rho wh \int_0^L \left(\frac{b(x)}{b_{max}}\right)^2 dx$$

B. Truss:

Displacement at a point x along the truss length is given by:

$$t(x) = \begin{cases} \frac{FL^3}{3EI}\left[1 + \frac{3L_c}{2L} + \left(\frac{3}{2L} + \frac{3L_c}{2L^2}\right)x + \frac{3L_c}{2RL^2}x^2 + \right. \\ \left. \frac{1}{RL^3}\left(1 - \frac{3L_c}{2}\right)x^3 \right], x < Lc \\ \frac{FL^3}{3EI}\left[1 + \frac{3L_c}{2L} + \frac{3L_c^2}{L^2} + \frac{3L_c^3}{RL^3} + \right. \\ \left. \left(\frac{3}{2L} + \frac{3L_c}{L^2} + \frac{3L_c}{2RL^3}\right)x \right]; L_c < x < L_c + \frac{L_s}{2} \end{cases}$$

The maximum displacement of the truss, t_{max}, can be determined by replacing x with $L_s/2$ in the second part of the equation of t(x).

$$m_t = \rho twh\left[\int_0^{L_c+\frac{L_s}{2}} \left(\frac{t(x)}{t_{max}}\right)^2 dx\right]$$

C. Finger:

The fingers are evenly distributed radially outward from the truss. For a specific finger, there is no variation of displacement along its arc length because it maintains the same radial distance from the center of rotation. Thus the effective mass of the fingers is given by:

$$m_f = \rho w_f h \sum_{n=1}^{N} \chi_n$$

Here, χ_n is the arc length of n^{th} finger.

D. Mirror:

The angular velocity is same throughout the mirror since there is no lateral force acting on it. So, the effective mass for the mirror section is given by:

$$m_m = \rho w_{mh} h L_m + \rho w_m h_m l_m$$

Here, w_{mh} is the mirror holder equivalent width and $w_m, h_m,$ and l_m are the mirror width, height and length, respectively.